Quantum Computational Simulations for Condensed Matter Systems

A Dissertation Presented for the

Doctor of Philosophy

Degree

The University of Tennessee, Knoxville

Trevor Alan Keen

August 2022

This work is dedicated to my family who have supported and encouraged me from a young age.

Acknowledgments

During my time here I have had the pleasure of working with many remarkable people both at the University of Tennessee and Oak Ridge National Laboratory. I would first like to thank my advisor Steve Johnston for his guidance and support during my time in his research group. He has kept me focused and guided me when I was unsure of what to do next. I would also like to thank my doctoral committee members Cristian Batista, Nicholas Peters, and Thomas Papenbrock for their advice and feedback throughout this experience. Similarly, I would like to thank my mentors Pavel Lougovski and Eugene Dumitrescu at Oak Ridge National Lab for sharing their expertise in quantum computing and their advice on research directions to pursue. I would also like to thank all of the collaborators and co-authors I have had over the years, including but not limited to Thomas Maier and Yan Wang at Oak Ridge National Laboratory, Bo Peng and Karol Kowalski at Pacific Northwest National Lab, and Thomas Steckmann and Lex Kemper at North Carolina State University.

Apart from professional connections, while in graduate school I have made a number of personal connections that have made Knoxville feel like home, and have made the experience so much more than getting a PhD. First, I would like to thank my girlfriend Rebecca Toomey for her love and support. She has always believed in me without fail, even when I didn't believe in myself. The peace she brought to my life and the inspiration she has given me through her own journey made the stresses of graduate school bearable. I would also like to thank my friends Quincy Clare-King and Brennan Hackett for pushing me and being on this graduate school journey with me. We have been through so much together and although we are all going our separate ways for now, I know that our friendships are life long ones.

To my family who, from an early age, has encouraged me to pursue higher education and supported me in ways that allowed me to do so.

To Mr. Steve Eischens and Mr. Eric Bizzell for igniting my interest in advanced physics and mathematics and entertaining my curiosity way beyond the requirements of their positions.

There are so many other people that I would like to thank, but this dissertation would be twice the length if I did so.

Abstract

In condensed matter physics, and especially in the study of strongly correlated electron systems, numerical simulation techniques are crucial to determine the properties of the system including interesting phases of matter that arise from electron-electron interactions. Many of these interesting phases of matter, including but not limited to Mott-insulating materials and possibly high-temperature superconducting systems, can be modeled by the Hubbard model. Although it is one of the simplest models to include electron-electron interactions, it cannot be solved analytically in more than one dimension and thus numerical techniques must be employed. Although there have been great strides in classical numerical simulation techniques for quantum many- body systems, all currently known simulation methods suffer from exponential resource scaling in certain parameter regimes.

Quantum computing techniques promise to alleviate these exponential scaling issues to allow simulations of larger and more complex systems. In this dissertation, I will present methods and results for simulations that leverage quantum computing for simulations of the Hubbard model. These simulations include both direct simulation of the Hubbard model along with results that solve the Hubbard model using dynamical mean-field theory (DMFT). Dynamical mean-field theory is a self-consistent mapping from the Hubbard to the Anderson impurity model, which reproduces the physics of the Hubbard model directly in the thermodynamic limit.

In terms of utilization of quantum computing techniques, here I present both results of a simulation run on real quantum hardware along with algorithms developed for future quantum hardware. Specifically, I run a small DMFT simulation which utilizes both classical

computing techniques and quantum computation. I also develop multiple algorithmic techniques for preparing quantum many-body states on a quantum computer and a quantum algorithm to calculate a generic response function of the system. Finally, I will give an outlook on challenges and future opportunities for using quantum computation to simulate quantum many-body systems.

Table of Contents

List of Tables

List of Figures

Chapter 1

Introduction and Motivation

1.1 Motivation

The pinnacle algorithm that showed the true potential of quantum algorithms is Shor's algorithm for the factorization of large numbers [1] discovered by Peter Shor in 1994. This algorithm spurred great interest in quantum computing research since it would allow one to break most currently used public-key cryptography schemes including RSA. However, Shor's algorithm will require thousands of essentially noiseless quantum bits (qubits) to break commonly used cryptography schemes. These types of stringent quantum hardware requirements will not be met for some time, and yet Shor's algorithm remains the end goal for many scientists studying quantum computation. However, in 1982, over ten years before the discovery of Shor's algorithm, Richard Feynmann proposed using quantum systems to simulate quantum models [2]. Even at this early stage in the theory quantum simulation, Feynman speculated that the resource requirements for simulating a physical quantum system using another quantum system would be strongly reduced compared to regular computing devices. It turns out that he was right about this exponential reduction in scaling, and even with all of the advances in classical computing made since 1982, quantum computers only need about 50 qubits to surpass classical simulations for certain systems [3].

Currently, we are in what has been called the "noisy intermediate-scale quantum" (NISQ) era [4], defined by the limited number of available qubits, their connectivity, and noise. These properties of current quantum computers severely limit the classes of problems that can be addressed. Fortunately, simulating quantum systems requires only tens of qubits to give quantum computers access to solutions of classically challenging problems, i.e. problems that have exponential scaling in classical computing methods [5]. It is expected that classically intractable problems can be addressed with as few as ~ 50 qubits [3]. For example, in a system of electrons, each electron requires one qubit to encode its occupation information. Extending this to many-fermion states, a system of 25 fermion-states can be encoded in just 50 qubits; in contrast, on a classical computer, the same state would require 2^{50} elements to be stored. Classical exact diagonalization schemes that solve the problem by diagonalizing the Hamiltonian of the system can handle $\sim 10-20$ electron orbitals for near half filling [6]. Therefore, only $\sim 20-40$ qubits are required for a quantum computational scheme to be competitive with classical exact diagonalization in the matter of storing the many-body state. This shows that the the memory resource requirements for simulating a general, strongly correlated system is much lower when using a quantum computer than for a classical computer.

Although the memory requirements to store a many-body state are significantly reduced for a quantum computer, actually finding those states is difficult [7]. The problem of reconstructing the entire quantum state with quantum state tomography is that it requires just as many resources as a classical simulation would [8]. In many cases, especially in condensed matter physics, we care about finding the expectation value of some operator instead of finding the final state of the system. Examples of desired quantities for strongly correlated electron systems include Green's functions and other correlation functions. Luckily, finding these expectation values is something that can be done relatively easily on a quantum computer. This provides the most relevant physical information about the system without needing to reconstruct the entire quantum state.

This is not to say that current quantum computers are perfect. Currently available qubits are noisy, i.e. there is some probability that performing an operation on one or more qubits

will give an incorrect result. Also, on currently available quantum hardware, not all qubits are interconnected. There are specific entangling channels that are allowed, i.e. you often cannot entangle any arbitrary two qubits on the device without an intermediary qubit. However, solutions to these problems are rapidly being addressed [9]. Every generation of quantum computers has more qubits with less noise than previous generations, and error correcting codes are rapidly being developed [10] for quantum computing devices that have more qubits with more interconnectivity. For near-term error reduction, there are many error mitigation techniques that address readout error (the quantum computer returns the incorrect state of the qubit) [11], and strategies to reduce the noise of specific unitary operations being performed [12, 13].

Fully fault-tolerant, large-scale quantum computation such as those needed to implement Shor's algorithm for problems of interest will not exist for some time, but algorithmic development is still needed to discover new techniques. NISQ devices with more than 50 qubits, on the other hand, already exist and may soon reach the level of sophistication needed to solve condensed matter problems that are not solvable classically [9, 14]. There are many proposed algorithms for using quantum computation to solve problems in condensed matter [15–18], but these algorithms need to be implemented and benchmarked in order to find the true bottlenecks of proposed algorithms and keep algorithmic development in line with the state of the art hardware.

In this thesis, I aim to find the true bottlenecks of proposed methods and propose workarounds that will allow for a quantum speedup over classical methods with a special emphasis on models and methods useful for condensed matter simulations. This thesis includes work on both quantum algorithmic development for fault-tolerant devices as well as benchmark simulations run on NISQ devices in order to both understand the state of the art and keep algorithmic design in line with possible applications on real devices.

1.2 Scalability Issues of Classical Algorithms

One of the main motivations for using quantum computers for many-body simulations is that all known classical simulations suffer from some exponential scaling issue in some parameter regime, whether it be in memory required or computation time. In this section, I will discuss the exponential scaling issues that arise in some of the most commonly used classical algorithms.

1.2.1 Fermionic Sign Problem

In a general quantum Monte Carlo (QMC) simulation, the simulation complexity is polynomial in inverse temperature and system size for parameter regimes without the sign problem, however the scaling becomes exponential in parameter regimes that exhibit the sign problem. When we expand the partition function for a QMC simulation, we would like to interpret the expansion coefficients as probability densities on the configuration space [19]. Fermionic anti-commutation relations can lead to negative weights (expansion coefficients), which prevents us from interpreting them as probabilities. To circumvent this, QMC practitioners consider a set of configurations $\mathbf{x}_i$ with weight distribution $|p(\mathbf{x})|$, which is different than the original expansion weight $p(\mathbf{x}) = \text{sgn}(p(\mathbf{x}))\ |p(\mathbf{x})|$. This change of weight distributions redefines expectation values as

$$\langle A \rangle = \frac{\langle A(p/|p|) \rangle_{|p|}}{\langle p/|p| \rangle_{|p|}} \implies \langle A \rangle = \langle A \,\text{sgn}(p(\mathbf{x})) \rangle_{|p|} \,/\, \langle \text{sgn}(p(\mathbf{x})) \rangle_{|p|} \,. \tag{1.1}$$

To compute this form of $\langle A \rangle$, we would sample the numerator and denominator separately [19]. Consider $\langle \text{sgn}(p(\mathbf{x})) \rangle = \mathcal{Z}/\mathcal{Z}_{|p|}$, where $\mathcal{Z}_{|p|}$ is the partition function of a system with positive weights $|p(\mathbf{x})|$. Rewriting this in terms of the difference of the free energies of the systems gives $\langle \text{sgn}(p(\mathbf{x})) \rangle = \mathcal{Z}/\mathcal{Z}_{|p|} = e^{-\beta \Delta F}$. Notice this will decrease exponentially as temperature decreases ($\beta \to \infty$) or volume increases (ΔF). The "sign problem" then is that as the system size or inverse temperature get large, the absolute value of the expected value of the sign approaches zero, i.e. $|\langle \text{sgn} \rangle| \to 0$ as $N, \beta \to \infty$. This gives a variance of

$\mathrm{Var}(\mathrm{sgn}(p(\mathbf{x}))) \approx 1$, and relative error after M measurements of $\Delta\,\mathrm{sgn} \approx \exp[\beta\Delta F]/\sqrt{M}$, which grows exponentially with decreasing temperature and/or increasing system size [19]. Since the relative error grows exponentially with decreasing temperature or increasing system size, the number of Monte Carlo measurements needed to counteract the sign problem will also grow exponentially, thus restoring the exponential complexity of solving the many-body problem.

It has been shown [20] that the sign problem is NP-hard, meaning that there is believed to be no polynomial time solution. It is important to note that the severity of the errors introduced by the sign problem, i.e. $|\exp[\beta\Delta F]|$, can depend on the model in question and the representation used in some cases [19].

This "sign problem" then results in a restriction of systems that can be efficiently simulated by quantum Monte Carlo techniques to relatively high temperatures systems for many models, especially if multiple orbitals are active or we include Hund's coupling [21]. For example, consider the Hubbard-Holstein model for fermions on a lattice, with on-site Coulomb repulsion U, an electron-phonon interaction term with strength λ, and the regular hopping and chemical potential terms. The fermion sign problem is not an issue in certain parameter regimes of filling and electron-phonon coupling strengths, allowing one to obtain meaningful results via Monte Carlo simulations [22]. For other parameter regimes however, the sign problem is so bad that the obtained results are basically meaningless (see Fig. 1.1) below a certain temperature [22].

In other systems such as the Hubbard model (Sec. 2.3), the issue of the sign-problem has a dependence on the geometry of the lattice [23]. For example, Ref. 23 explores the dependence of the sign problem in the Hubbard model for chain, ladder, square, rectangular, cubic, triangular, honeycomb, Lieb, and Kagome lattices for various values of on-site Coulomb repulsion and temperature. The results also show the dependence of the sign problem filling of the system, i.e. average number of electrons per lattice site and confirm previous results showing the fast appearance of the sign problem near half-filling (average of one electron per lattice site) for many systems of interest.

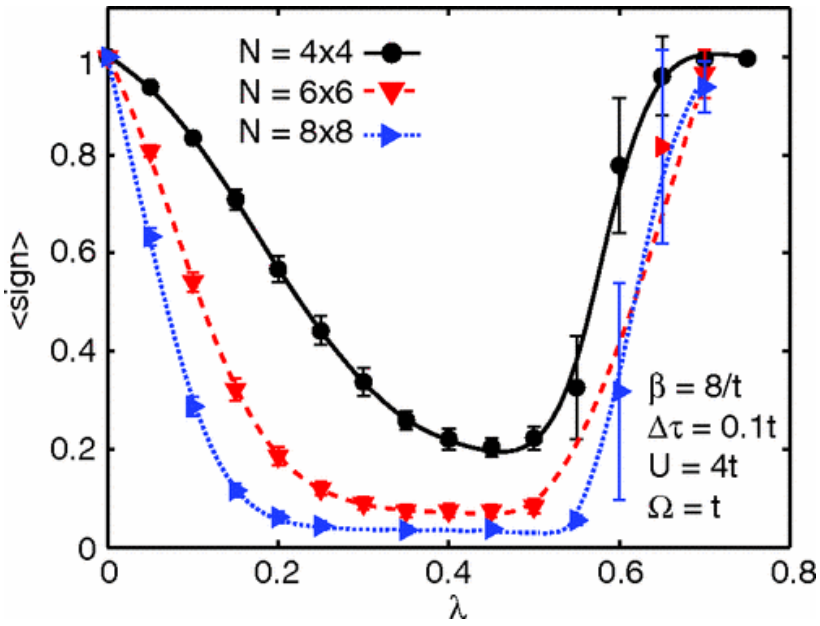

Figure 1.1: Expectation value of fermion sign as a function of electron-phonon coupling λ in the Hubbard-Holstein model for various lattice sizes at half-filling. The areas where $\langle \text{sign} \rangle$ becomes small represent parameter regimes where the fermion sign problem dominates. Figure from [22].

1.2.2 Memory Requirements

Other methods besides QMC, such as exact diagonalization (ED), coupled cluster, and density-matrix renormalization group, do not suffer from the issue of the sign problem. Exact diagonalization avoids the sign problem at the cost of an exponentially increasing amount of memory required to store the many-body wave function. For example, a classical computer will need to store a vector of dimension 2^{2N} for N spin-orbitals [5, 24]. This memory requirement restricts one to problems with $\sim 10 - 20$ sites in a lattice model depending on the filling [6].

Coupled cluster methods (see Sec. 2.5) reduce the storage complexity to polynomial in system size [25], but lack predictive power for strongly correlated molecules. Attempted techniques to deal with strong correlations in the coupled cluster method either lack the desired polynomial computational cost as a function of size, or are insufficiently accurate to make predictions [26]. This inaccuracy stems from using a mean-field (often Hartree-Fock) state as the initial trial state and truncating the cluster operator to a finite number of excitation operators. As the interactions between electrons get stronger and contribute more to the physics of the problem, higher orders of excitation operators are required. These assumptions make coupled-cluster methods extremely costly to use for strongly correlated systems.

The density-matrix renormalization group (DMRG) method [27] reduces the effective degrees of freedom using variational methods to find the lowest energy matrix product state (MPS). This construction alleviates the memory issue experienced as compared to ED, but DMRG is only accurate for systems with low entanglement (are close to a matrix product state) for certain geometries [26, 28]. As the entanglement entropy grows, more states must be kept, which increases the memory requirements. Therefore, DMRG is typically restricted to one-dimensional systems since the entanglement entropy is proportional to the surface area. This increase in entropy with system size makes matrix product states bad approximants to the true ground state [29].

1.3 Advantages of Quantum Computation

As mentioned, for a suitably chosen basis, the quantum many-body state can be encoded in a number of qubits that scales polynomially with system size instead of with an exponential amount of classical memory. In fact, for many problems of interest, the number of qubits required to store the many-body quantum state of interest is actually linear in system size. For example, this is the case for Hamiltonians with nearest or next-nearest-neighbor interactions [3]. This scaling of required resources means that a wavefunction that could not be stored classically can be stored with ~ 50 qubits. Now that multiple devices with over 50 qubits exist, e.g. Google [9] and IBM [14], we can begin to simulate problems on quantum computers that cannot be simulated classically.

1.4 Basics of Quantum Computing

In order for a physical system to be eligible for use as a quantum computing device, the system must be able to [10, 30]:

1. Represent the state of a qubit (Sec. 1.4.1);
2. Perform a universal family of unitary transformations/gates (Sec. 1.4.2);
3. Prepare the register of qubits in a suitable initial state; and
4. Measure the result of a computation, i.e. report the state of a qubit.

The first two of these requirements will be explored below. The third means that one has sufficient control over the qubits such that they can be put into a fiduciary quantum state. The fourth requirement ensures that we have some way of reading the state of a qubit. Note that these are *physical* requirements of a quantum computer, independent of the algorithms, measurement schemes, etc. used. These requirements are also included in the so called DiVincenzo criteria [30], but we will use the form enumerated above.

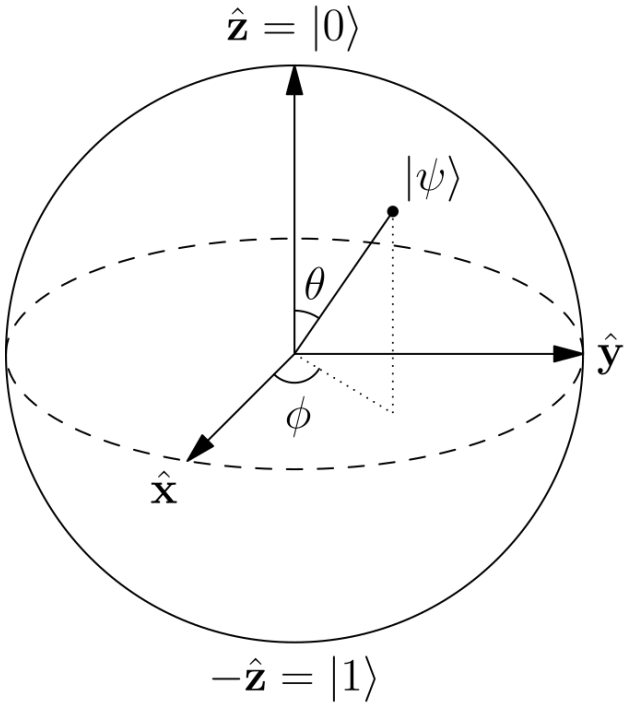

Figure 1.2: The Bloch sphere can be used to represent the state of the qubit. A classical bit could only have the state on the poles, but a qubit can be in a superposition, i.e. be in a state anywhere on the surface of the sphere. Here, the state $|\psi\rangle$ is given by $|\psi\rangle = \cos\left(\frac{\theta}{2}\right)|0\rangle + e^{i\phi}\sin\left(\frac{\theta}{2}\right)|1\rangle$. Figure from Ref. 31.

1.4.1 Qubits

A quantum bit, or qubit, is the quantum version of the classical bit, and is the basic unit of quantum information. As opposed to a classical bit which would require an exponential amount of memory to store a quantum state, a qubit can express a quantum state with a polynomial number of qubits. Figure 1.2 shows the *Bloch sphere*, which can be used to pictorially represent the state of a qubit and the operations that can be used to change the state of the qubit. In Fig. 1.2, $|0\rangle$ and $|1\rangle$ would correspond to the state of a classical bit, whereas a qubit can take on any state on the surface of the Bloch sphere parameterized by angles θ and ϕ.

Physical Qubits

The best physical realization of a qubit for use in quantum computation is still an open question. There are many different kinds of qubits, but here I will report only on the most commonly used at the time of writing, along with some extremely promising future technologies.

In my work for this thesis, I utilized so-called superconducting qubits. Superconducting qubits come in three main sub-varieties: charge qubits, flux qubits, and phase qubits, all of which have their advantages and disadvantages. For the work in this thesis, transmon-based charge qubits were used. A transmon is an anharmonic oscillator created by replacing the inductor in an LC circuit with a Josephson junction [32]. The state of the qubit, then, is the eigenstate of the anharmonic oscillator. The states of the qubits can be manipulated using AC currents oscillating at microwave frequencies, and capacitors between qubits allow for entanglement. The measurement of a superconducting charge qubit is performed by measuring the population of the transmon oscillators [32].

Another physical realization of a qubit is in an ion trap quantum computer [10, 33]. An ion trap quantum computer is composed of ions held in place using electromagnetic forces, and the state is given by the nuclear spin of the trapped atoms. To prepare them, the ions are cooled until they are in their vibrational and hyperfine ground states. The states of the

qubits are controlled using light, which causes transitions and in turn changes the atomic state. The qubit-qubit interaction is mediated with a phonon state. Measuring the qubits can be done by measuring the population of the hyperfine states of the ions.

In quantum dot qubits, electrons are trapped in a semiconducting material. These quantum dots come in pairs, and the state of the qubit is decided by which of the quantum dots in the pair contains an electron. Operations are performed on the qubits by a voltage applied between the two dots. Like the superconducting charge qubit, the measurement is a measurement of the charge in a quantum dot [10].

One possible future technology is the topological qubit. However, this type of qubit relies on the existence of non-Abelian anyons, which have not yet been found experimentally. In a topological quantum computer, the state is described by the braiding of the world lines of two anyons, and swapping the positions of adjacent anyons to create new braids constitutes qubit operations. To measure the state of the qubits, the states of the anyons would be measured [34–36]. This particular technology is exciting because small disturbances to the anyons from the environment do not change the topology, making topological qubits resilient to most common sources of error. Although a topological qubit has not been discovered to date, these qubits would be extremely robust to noise from the environment and they are being actively pursued with promising results [34].

1.4.2 Quantum Gates

Recall that for a system to be considered viable for use as a quantum computer, it must be able to perform a universal family of unitary transformations, i.e. it must be able to put a register of qubits into an arbitrary state. In other words, suppose we are given a set of quantum gates that operate on individual qubits or sets of qubits. That set is said to be universal for quantum computation if any unitary operation can be approximated to arbitrary accuracy using a quantum circuit composed only of those gates [10]. In this section, I will give the precise conditions for a set of gates that are universal, along with a commonly used gate set. The gate set used in this section, however, is not unique and is often

determined by what operations are easiest to perform on the qubits themselves. There are three main universality constructions that, when combined, prove that any unitary operation can be approximated to arbitrary precision using combinations of just four basis gates (three single-qubit and one entangling gate), e.g. [10]:

1. The Hadamard gate (single-qubit) : $\frac{1}{\sqrt{2}}\begin{pmatrix} 1 & 1 \\ 1 & -1 \end{pmatrix}$
2. The Phase gate (single-qubit) : $\begin{pmatrix} 1 & 0 \\ 0 & i \end{pmatrix}$
3. The $\pi/8$ or T gate (single-qubit) : $\begin{pmatrix} 1 & 0 \\ 0 & e^{i\pi/4} \end{pmatrix}$
4. The Controlled NOT (CNOT) gate (two-qubit) : $\begin{pmatrix} 1 & 0 & 0 & 0 \\ 0 & 1 & 0 & 0 \\ 0 & 0 & 0 & 1 \\ 0 & 0 & 1 & 0 \end{pmatrix}$.

The phase gate is not strictly necessary since it is simply two T gates, but it is convenient in fault tolerant analysis. The constructions needed to show that these gates constitute a universal gate set are [10]:

1. An arbitrary unitary operator can be expressed exactly as a product of unitaries that each acts on a subspace of the states of at most 2 qubits.

2. An arbitrary unitary operator can be expressed to arbitrary precision with the above gates combined as in construction 1.

3. A single qubit operation can be approximated to arbitrary accuracy with the above gates 1-3, combined with construction 2.

The first construction hinges on the fact that a d-dimensional unitary matrix can be decomposed using d unitary matrices that act non-trivially on at most two vector

components. The second construction can be shown using Gray codes [10], which are sequences of binary numbers such that adjacent members differ in exactly one bit. Gray codes are used to show that an arbitrary unitary operation on n qubits can be implemented with single-qubit and CNOT operations. In the worst case, an exponential number of operations will be required. This can be seen by observing that the space of state vectors of n qubits can be represented by the unit $2^{n+1}-1$ dimensional sphere. The number of patches on the surface of the sphere with radius of the allowable error ϵ is the ratio of the surface area of the $2^{n+1}-1$ unit sphere to the volume of the $2^{n+1}-2$ sphere of radius ϵ. This shows that the number of operations required grows exponentially in the number of qubits. Fortunately, for many unitaries of interest, this worst case scenario is not the average case [10].

1.4.3 Quantum Circuit Conventions

In the construction of a quantum circuit, wires are used to represent qubits, time goes from left to right (leftmost operations are applied to the qubits first, often in parallel), and a wire with a \ through it denotes a bundle of qubits. The gates that will be used in this thesis and their corresponding symbols are:

- Hadamard: —[H]— $= \frac{1}{\sqrt{2}} \begin{pmatrix} 1 & 1 \\ 1 & -1 \end{pmatrix}$
- Pauli matrix X Rotation by angle θ: —[$e^{-i\frac{\theta}{2}X}$]— $=$ —[$R_X(\theta)$]— $= \begin{pmatrix} \cos\left(\frac{\theta}{2}\right) & -i\sin\left(\frac{\theta}{2}\right) \\ -i\sin\left(\frac{\theta}{2}\right) & \cos\left(\frac{\theta}{2}\right) \end{pmatrix}$
- Pauli matrix Y Rotation by angle θ: —[$e^{-i\frac{\theta}{2}Y}$]— $=$ —[$R_Y(\theta)$]— $= \begin{pmatrix} \cos\left(\frac{\theta}{2}\right) & -\sin\left(\frac{\theta}{2}\right) \\ \sin\left(\frac{\theta}{2}\right) & \cos\left(\frac{\theta}{2}\right) \end{pmatrix}$

- Pauli matrix Z Rotation by angle θ: 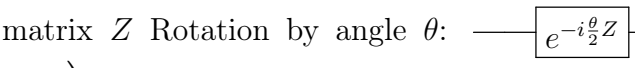 $= \begin{pmatrix} e^{-i\frac{\theta}{2}} & 0 \\ 0 & e^{i\frac{\theta}{2}} \end{pmatrix}$
- T-gate: 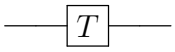 $= \begin{pmatrix} 1 & 0 \\ 0 & e^{i\pi/4} \end{pmatrix}$
- Phase gate: 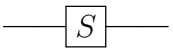 $= \begin{pmatrix} 1 & 0 \\ 0 & i \end{pmatrix}$
- CNOT (Controlled X) gate: 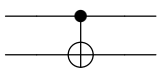 $= \begin{pmatrix} 1 & 0 & 0 & 0 \\ 0 & 1 & 0 & 0 \\ 0 & 0 & 0 & 1 \\ 0 & 0 & 1 & 0 \end{pmatrix}$
- Controlled $U = \begin{pmatrix} u_{00} & u_{01} \\ u_{10} & u_{11} \end{pmatrix}$ gate: 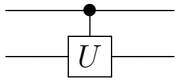 $= \begin{pmatrix} 1 & 0 & 0 & 0 \\ 0 & 1 & 0 & 0 \\ 0 & 0 & u_{00} & u_{01} \\ 0 & 0 & u_{10} & u_{11} \end{pmatrix}$

In the two-qubit gates (CNOT and controlled U), the filled dot on the first (top) qubit denotes that if the first qubit is in the state $|1\rangle$, then the operation being controlled (X or U) is applied to the second qubit. There are analogous gates for controlling the operation on the state $|0\rangle$, and in this case the filled dots are replaced with unfilled circles ($\circ$). It is possible to extend the CNOT and controlled U gates to have multiple control qubits, i.e. the application of the X or U gate depends on the state of multiple control qubits, see Fig. 3.2 for an example. These gates, and many of the gates listed above, are defined simply for convenience and can always be decomposed into any universal gate set.

Chapter 2

Concepts in Quantum Many-Body Theory

In the field of condensed matter physics, many researchers are striving to develop advanced numerical methods to perform simulations. However, all currently known classical simulations at their core either make an assumption about the system that is not completely general or suffer some exponential scaling for some parameter regimes. In this chapter, I will introduce the condensed matter concepts and models that are used throughout this thesis and some of the relevant classical techniques that are often used to solve them.

2.1 Finite-Temperature Green's Function Formalism

In my projects that compose this thesis, I have mainly been focused on calculating zero-temperature, single-particle Green's functions. This is due to the fact that the single-particle Green's function is easier and less cumbersome to work with than the full many-body states, but still contains the interesting physics of the problem. For example, the expected value of any single-particle operator of interest can be extracted from the single-particle Green's function, and the Green's function is a central quality in many simulation schemes, such as dynamical mean-field theory (DMFT). While I have focused mainly on the zero-temperature

Green's function, here I will present the Green's function formalism at finite temperature in order to give the broadest understanding possible. It is relatively easy to extrapolate to the zero-temperature limit from the finite temperature formalism. In the case of degenerate ground-states, this is actually advantageous since the zero-temperature limit will give the thermally weighted average of the degenerate ground-states [37].

In the most generic sense, a Green's function describes the response of a system to an excitation. The finite temperature Green's function essentially takes into account the fact that the excitation is interacting with a bath of particles that have some average energy. Luckily, we do not need to know the exact state of the particles in the bath, which fluctuate through different configurations, we only need the temperature and Hamiltonian [37].

When constructing the finite temperature Green's function, we must take the thermodynamic average of the system. A Green's function for the electron then is

$$G(t,t') = \frac{\mathrm{Tr}\left[e^{-\beta H}\ c_\lambda(t)\ c_\lambda^\dagger(t')\right]}{\mathrm{Tr}\left[e^{-\beta H}\right]}, \tag{2.1}$$

where β is inverse temperature, $c_\lambda(t)$ is the time-dependent annihilation operator in the Heisenberg picture $c_\lambda(t) = e^{iHt}c_\lambda e^{-iHt}$ and the trace Tr is a summation over a complete set of states. Because of the factor $e^{-\beta H}$ in the finite-temperature Green's function, one in principle has to do an expansion for both $e^{-\beta H}$ and $e^{\pm iHt}$. However, if we consider the time variable as a "complex temperature", we can treat t and β as the real and imaginary parts of a complex variable. In that case, time becomes complex with $\tau = it$ (also known as a Wick rotation) and the Green's function will be a function of τ with domain $-\beta \leq \tau \leq \beta$. This is known as the Matsubara method [37, 38].

If the Hamiltonian is time-independent, then the Green's function is a function of $\tau - \tau'$ instead of τ and τ' and we can define the electron Green's function as

$$G\left(\tau - \tau'\right) = -\left\langle T_\tau c_\lambda\left(\tau\right) c_\lambda^\dagger\left(\tau'\right)\right\rangle. \tag{2.2}$$

Here, the bracket $\langle O \rangle$ denotes the thermodynamic average of the operator and T_τ is an imaginary time ordering operator that arranges operators with the earliest τ to the right. The Fourier transform of this Green's function gives the Matsubara frequency Green's function

$$G\left(i\omega_n\right) = \int_0^\beta d\tau \; G\left(\tau\right) \; e^{i\tau\omega_n}, \tag{2.3}$$

which is a function of Matsubara frequency $i\omega_n$, where (for fermions) $\omega_n = \frac{(2n+1)\pi}{\beta}$, $n \in \mathbb{Z}$ are the fermionic Matsubara frequencies, i.e. the poles of the thermal occupation number function. In this step, we make the substitution $H \to H - \mu N$, with μ the chemical potential of the system and N the total number of particles, in order to introduce the grand canonical ensemble where the number of particles in the system can vary.

It is convenient at this point then to define the grand partition function $\mathcal{Z} = \mathrm{Tr}\left[e^{-\beta(H-\mu N)}\right]$. From this, we can construct a single-electron Green's function by expanding Eq. (2.3) using sums of complete sets of eigenstates $\sum_n |n\rangle\langle n|$ and $\sum_m |m\rangle\langle m|$ of the Hamiltonian such that:

$$G(i\omega_n) = \frac{1}{\mathcal{Z}} \sum_{n,m} \left|\langle n| \, c_\lambda \, |m\rangle\right|^2 \frac{e^{-\beta E_n} + e^{-\beta E_m}}{i\omega_n + E_n - E_m}. \tag{2.4}$$

To extract the real-frequency behavior of the single-particle Green's function, it suffices to take Eq. (2.4) and let $i\omega_n \to \omega + i\delta$, where $\delta = 0^+$ is a convergence factor, to obtain the so-called retarded Green's function. Then, one can extract useful quantities such as the spectral function

$$A = -\frac{2}{\pi} \, \mathrm{Im}\{G\}, \tag{2.5}$$

which gives the probability that an electron has energy ω and other quantum number λ [37].

After the analytic continuation to the real-frequency domain, the retarded, single-particle Green's function is given by

$$G^R(\lambda,\omega) = \frac{1}{\mathcal{Z}}\sum_{n,m} |\langle n|\, c_\lambda\, |m\rangle|^2 \frac{e^{-\beta E_n} + e^{-\beta E_m}}{\omega + i\delta + E_n - E_m}. \tag{2.6}$$

The spectral function for the single-electron is just $-2\,\mathrm{Im}\{G^R(\omega)\}$ (note that in some formulations there is a normalization factor $(-1/\pi)$ instead of -2), and in this case is

$$A(\omega) = \frac{2\pi}{\mathcal{Z}}\sum_{n,m} |\langle n|\, c_\lambda\, |m\rangle|^2 (e^{-\beta E_n} + e^{-\beta E_m})\delta(\omega + E_n - E_m). \tag{2.7}$$

This function has a couple of important features. For one, it is absolutely positive for any λ and ω. Secondly, it satisfies the sum rule [37]

$$\int_{-\infty}^{\infty} \frac{d\omega}{2\pi} A(\omega) = 1. \tag{2.8}$$

2.2 Zero-Temperature Limit

When one takes the zero-temperature limit ($\beta \to \infty$) of the Green's function as presented in Eq. (2.1), the thermodynamic operator $e^{-\beta H}$ will project out the ground state of the Hamiltonian, resulting in a zero-temperature Green's function of the form

$$G(\lambda, t-t') = -i\,\langle GS|T_t\left[e^{iHt}c_\lambda e^{-iH(t-t')}c_\lambda^\dagger e^{-iHt'}\right]|GS\rangle\,, \tag{2.9}$$

where T_t now is the real-time time ordering operator. The quantity I will focus mostly on is specifically the zero-temperature retarded Green's function given by

$$G^R_{j\sigma,j'\sigma'}(t,t') = -i\theta(t-t')\,\langle\psi_0^N|\left\{\hat{c}_{j\sigma}(t), \hat{c}^\dagger_{j'\sigma'}(t')\right\}|\psi_0^N\rangle\,, \tag{2.10}$$

where $\left|\psi_0^N\right\rangle$ is the ground state of the N-particle system, j and j' will denote lattice sites, and σ, σ' denote the spin. In this work, only time-translationally invariant (time-homogeneous) systems are considered, so the Green's function only depends on $t - t'$ and we can choose $t' = 0$. In addition, if the Green's function is diagonal in spin space $G_{j\sigma,j'\sigma'}(t) = G_{j\sigma,j'\sigma}(t)\delta_{\sigma\sigma'}$ and spin-rotationally invariant $G_{j\uparrow,j'\uparrow}(t) = G_{j\downarrow,j'\downarrow}(t)$, we suppress the spin index when there is no confusion. One way to physically interpret the Green's function in Eq. (2.10) is as follows. For simplicity, let us take the first term of the anticommutator, the second term will use the same reasoning. Here, j and j' take the role of the position and let $t' = 0$, which in turn causes $e^{-iHt'} \to \mathbb{1}$ and $e^{-iH(t-t')} \to e^{-iHt}$.We further assume the system is spin-rotationally invariant so $\sigma = \sigma'$ and also assume $j = j'$. Then, take the true ground state of the system and create an excitation at position $j = j'$ with spin $\sigma = \sigma'$ at time 0. Then, at time t destroy the excitation at site $j = j'$ with spin $\sigma = \sigma'$. In general, during the time between 0 and t, the excitation is scattered, or shifted in energy, or is affected by the system in some way. When one measures at a later time t we find how much amplitude is left in the state that was created by the initial excitation, which gives information about the response of the system to the introduction of the particle.

Taking the Fourier transform of the time-domain Green's function at zero temperature gives the energy Green's function similar to the Matsubara case (just take $i\omega_n \to \omega + i\delta$ and the zero-temperature limit). It is also important to note that, for a single-electron in a band, the non-interacting Green's function in the frequency domain is given by

$$G^{(0)}(\lambda, \omega) = \frac{1}{\omega + i\delta - E_\lambda}. \tag{2.11}$$

The full (interacting) Green's function then can be written as

$$G(\lambda, \omega) = \frac{1}{\omega + i\delta - E_\lambda - \Sigma(\lambda, \omega)}, \tag{2.12}$$

where Σ denotes the electron self-energy. This self-energy is named as such because the electron added has an effect on the system, which in turn modifies the effect the system

has on the electron, so in a roundabout way the electron is having an effect on itself. This formulation states that the exact Green's function of the system is obtained by calculating the self-energy via Dyson's equation [37]

$$G(\lambda,\omega) = \frac{G^{(0)}(\lambda,\omega)}{1 - G^{(0)}(\lambda,\omega)\Sigma(\lambda,\omega)}. \tag{2.13}$$

2.3 Hubbard Model

Although its conception dates back to the 1960's and its original use was to describe the ferromagnetism in transition metals [39], the Hubbard model remains one of the central models to condensed matter physics. Its importance lies in the fact that it is one of the easiest to express models containing electron-electron interactions, and yet it captures many interesting phenomena. Some examples of these phenomena are the Mott metal-insulator transition [40–42], antiferromagnetism [43], emergent spin and stripe orders [44, 45], fractionalized quasiparticles [46], strange metallic behavior [47], pseudogaps [48, 49], and high-temperature superconductivity [48, 50], depending on its dimensionality and parameter regime.

The Hamiltonian describing the Hubbard model contains both electron hopping terms and on-site electron-electron interaction terms and can be written as

$$H = -t \sum_{\langle i,j\rangle,\sigma} c^{\dagger}_{i,\sigma} c_{j,\sigma} + U \sum_{i} \hat{n}_{i,\uparrow}\hat{n}_{i,\downarrow} - \mu \sum_{i} \left(\hat{n}_{i,\uparrow} + \hat{n}_{i,\downarrow}\right), \tag{2.14}$$

where $\langle i,j\rangle$ denotes hopping between nearest neighbor sites, $c^{\dagger}_{i,\sigma}\left(c_{j,\sigma}\right)$ creates (destroys) an electron with spin σ on site i, $n_{i,\uparrow} = c^{\dagger}_{i,\uparrow}c_{i,\uparrow}$, $t_{i,j}$ is the hopping integral between sites i and j, U is the Coulomb repulsion strength between electrons on the same site, and μ is an optional chemical potential term used to set the particle density. This model is illustrated in Fig. 2.1 on a 2D square lattice. The simplicity of the model is deceiving since there is no known analytical solution, except in the special case of the one-dimensional system with nearest neighbor hopping [46].

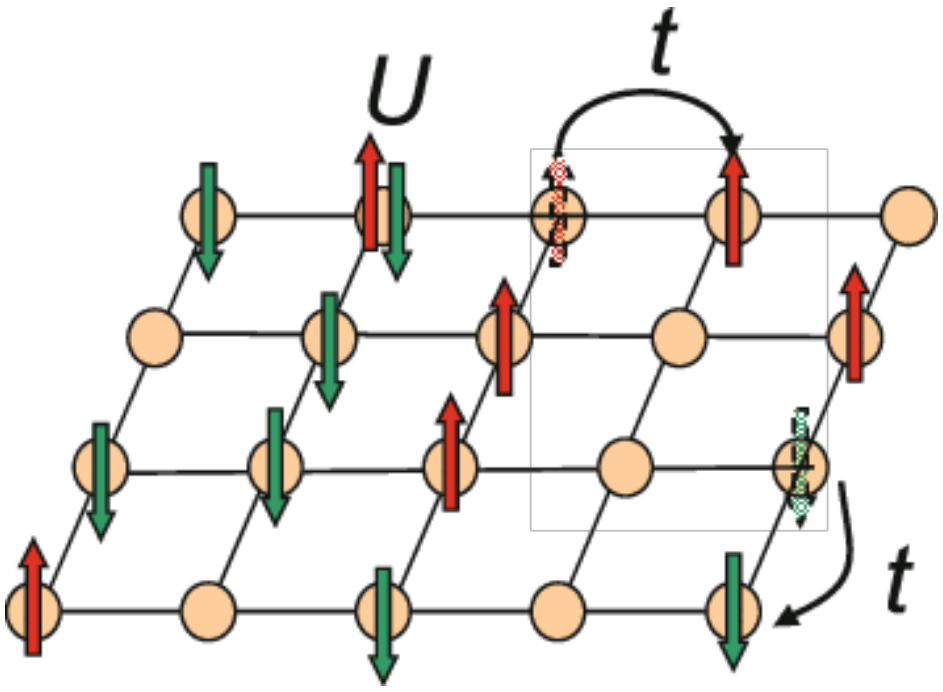

Figure 2.1: Diagram of the two-dimensional Hubbard model on a square lattice with hopping parameter t and on site electron-electron interaction U. Diagram from Ref. [54]

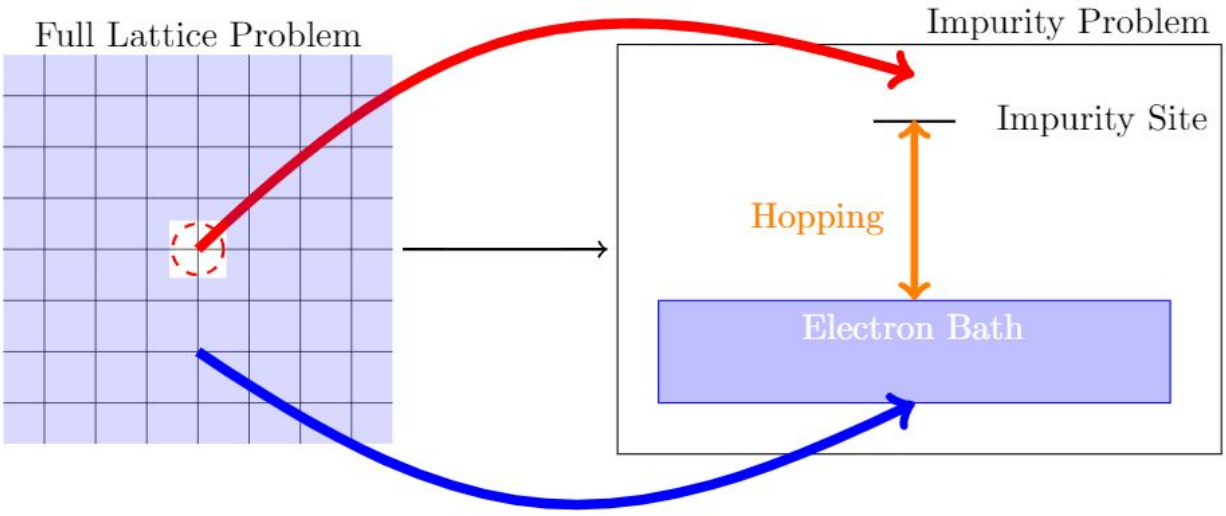

Figure 2.2: Diagram of the DMFT mapping. In DMFT the full lattice problem (left) is mapped onto an impurity problem (right). The single impurity site from the lattice retains the electron-electron interaction and allows hopping from the non-interacting bath to the impurity site.

2.4 DMFT and AIM

The Anderson impurity model (AIM) has played an essential role in developing our understanding of localized fermionic degrees of freedom coupled to a continuum [37]. The model describes localized magnetic moments embedded in a sea of conduction electrons and is closely related to the Kondo problem [51, 52]. It also plays a central role in dynamical mean-field theory (DMFT) [53], where a problem on an infinite lattice is mapped onto an AIM whose parameters are determined self-consistently to reproduce the physics of the original problem, see Fig. 2.2. In this context, the continuum levels are often referred to as "bath" levels, and we will use this language throughout the thesis. DMFT is one of the most widely used frameworks for studying the phenomena in the Hubbard model arising from electron-electron correlation [53].

In the limit of infinite dimensions, the mapping from the infinite lattice to the impurity model becomes exact, but the model Hamiltonian (specifically the kinetic energy term) must be rescaled so that the energy does not diverge [53]. In the specific case of DMFT on the Hubbard model, the impurity model is the Anderson impurity model (AIM). The Anderson impurity model Hamiltonian is given by

$$H_{\mathrm{AIM}} = \sum_{i=0,\sigma}^{N_{\mathrm{bath}}} \left(\epsilon_i - \mu\right) \hat{n}_{i,\sigma} + U \hat{n}_{0,\uparrow} \hat{n}_{0,\downarrow} + \sum_{i=1,\sigma}^{N_{\mathrm{bath}}} V_i \left(c_{0\sigma}^{\dagger} c_{i,\sigma} + c_{i,\sigma}^{\dagger} c_{0,\sigma}\right), \tag{2.15}$$

where subscript 0 denotes the impurity site, U is the impurity site Coulomb repulsion, V_i denotes the hopping between bath site i and the impurity, μ is the chemical potential used to set the filling, and the ϵ_i denotes the site energy of site i.

The central quantity of DMFT is the impurity site single-particle (hole and electron) retarded Green's function. In the real time domain, this quantity is given by

$$iG_{\mathrm{imp}}(t) = \theta(t) \langle GS | \{c_\sigma(t), c_\sigma^{\dagger}(0)\} | GS \rangle, \tag{2.16}$$

where $\theta(t)$ is the Heaviside step function, and $|GS\rangle$ denotes the ground state of the system, which is analogous to Eq. (2.9). In the paramagnetic phase, $G_{\text{imp}}(t)$ is spin symmetric, and so it is sufficient to only compute $G_{\text{imp}}(t)$ for one spin configuration.

Fourier transforming this quantity to the real frequency domain gives the impurity Green's function in the frequency domain analogous to Eq. (2.12)

$$G_{\text{imp}}(\omega) = \frac{1}{\omega + \mu - \Delta(\omega) - \Sigma_{\text{imp}}(\omega)}, \tag{2.17}$$

where $\Delta(\omega) = \sum_i \frac{|V_i|^2}{\omega - (\epsilon_i - \mu)}$ is the so-called hybridization function that describes the coupling of the impurity to the bath, and Σ_{imp} is the impurity self-energy, which is due to the interactions on the impurity site. In the non-interacting limit ($U = 0$), the Green's function reduces to an analog of Eq. (2.11) with the eigenenergies replaced by the hybridization function

$$G^{(0)}_{\text{imp}}(\omega) = \frac{1}{\omega + \mu - \Delta(\omega)}. \tag{2.18}$$

The self-energy can be calculated using Eq. (2.17) along with Eq. (2.18) using Dyson's equation, Eq. (2.13), for the impurity model

$$\Sigma_{\text{imp}}(\omega) = G^{(0)}_{\text{imp}}(\omega)^{-1} - G_{\text{imp}}(\omega)^{-1}. \tag{2.19}$$

DMFT is a self-consistent algorithm, meaning the problem must be solved and the DMFT parameters (V_i and ϵ_i) updated many times to solve the problem (see Fig. 2.3). This self-consistency condition ensures that the local problem matches the impurity problem, i.e. $\Sigma_{\text{imp}}(\omega) = \Sigma_{\text{loc}}(\omega)$. The self-consistency equation along with Dyson's equation form a complete set, allowing us to find updates to the DMFT parameters until a self-consistent solution is found [53]. Useful results that approach the thermodynamic limit can be obtained from DMFT with only a few impurity orbitals [15]. The steps of the DMFT loop are shown in Fig. 2.3 and can be enumerated as

1. Make the DMFT assumption $\Sigma_{ii}(\vec{k}, \omega) \approx \Sigma_{\text{imp}}(\omega)$.

2. Initialize the local self-energy $\Sigma_{ii}(\omega)$.

3. Calculate the local Green's function making the local self-energy approximation

$$G_{ii}(\omega) = \sum_{\vec{k}} \frac{1}{\omega + \mu - \epsilon(\vec{k}) - \Sigma_{ii}(\omega)}$$

   where $\epsilon(\vec{k})$ is the dispersion relation of the non-interacting system.

4. Fit the hybridization function using the local Green's function

$$\Gamma(\omega) = \sum_{i=1}^{N_b} \frac{V_i^2}{\omega + \mu - \epsilon_i} = \omega + \mu - G_{ii}^{-1} - \Sigma_{\text{imp}}(\omega)$$

   where the V_i and ϵ_i are the bath parameters to be extracted from the fit.

5. Calculate the impurity Green's function

$$G_{\text{imp}}(\omega) = \frac{1}{\omega + \mu - \Gamma(\omega) - \Sigma_{\text{imp}}(\omega)}$$

   and the bath Green's function $G_0(\omega) = \dfrac{1}{\omega - \Gamma(\omega)}$.

6. Calculate the impurity self-energy from the Dyson equation $\Sigma_{\text{imp}}(\omega) = G_0^{-1}(\omega) - G_{\text{imp}}^{-1}(\omega)$.

7. Check for convergence of the self-energy $\Sigma_{ii}(\omega) \stackrel{?}{=} \Sigma_{\text{imp}}(\omega)$.

8. If no convergence, return to step 3, replacing the local self-energy with the impurity self-energy and loop again.

Note that here I have used the placeholder ω instead of choosing to work in Matsubara frequency space or real-frequency space.

Although the DMFT mapping simplifies the lattice problem to be solved, we still need to solve the impurity problem. One widely used technique is exact diagonalization (ED). In ED, the bath is discretized to a finite set of levels as opposed to a continuum. The

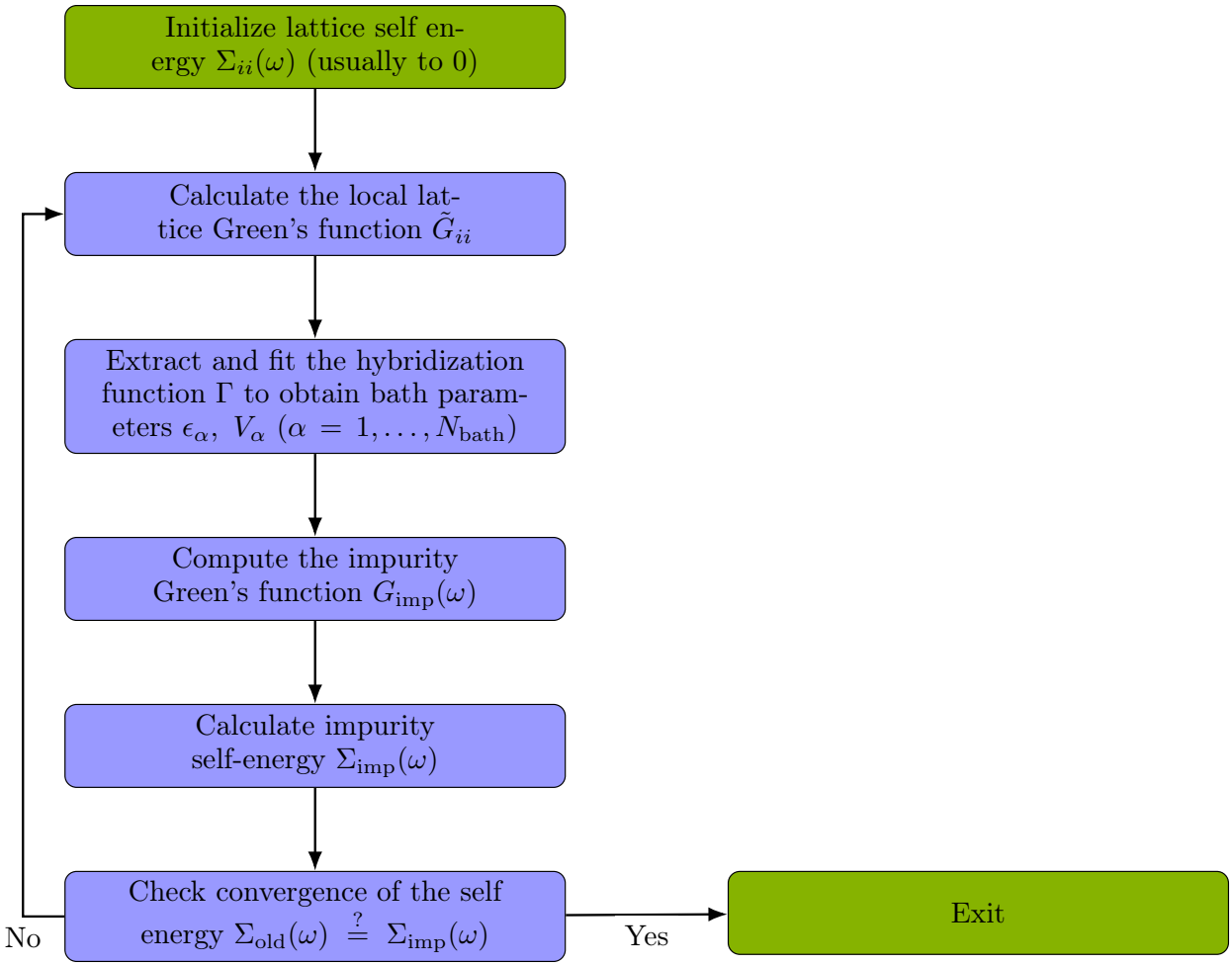

Figure 2.3: Diagram of the DMFT loop.

impurity problem is then solved by finding the eigenvalues and eigenvectors of the AIM Hamiltonian. However, since the bath levels are discretized, the amount of memory required to store the quantum many-body state grows exponentially with the number of bath levels used. For each iteration of the DMFT loop, the infinite lattice is projected to the impurity and vice versa. For these projections to be valid, the self-energy must be nearly local, i.e. the self-energy should be a function of frequency only instead of momentum and frequency. In the exact diagonalization solution to DMFT, the size of the Hilbert space determines the energy spacing between excited states. This spacing should be small enough that the low-energy behavior of the self-energy is resolved. The discretization of the lattice, however, depends strongly on the temperature used in the Matsubara imaginary time formulation of the problem. When the temperature is decreased, the low-energy characteristics of the lattice Green's function show increased sensitivity, which in turn requires a larger bath, see Ref. 6 for a complete analysis.

The standard method for approximately diagonalizing Hamiltonian matrices is the Lanczos method [55, 56]. In the Lanczos method, a Hermitian matrix H is tridiagonalized within a *Krylov space* which is generated by acting on some initial vector with powers of H. In the Krylov space, H will be tridiagonal, and tridiagonal matrices can be efficiently diagonalized using, for example, the QR decomposition [57]. The Lanczos method works well for zero-temperature systems, but when used for finite temperature calculations it suffers from numerical instability due to the loss of the orthogonality of the excited states. If one is simply looking for the Green's function of the system, however, it can be found with just the elements of the tridiagonal form of the Hamiltonian [56].

2.5 Coupled Cluster Methods

Classical coupled cluster (CC) methods have been used to compute the impurity coupled cluster Green's function (CCGF) [58–60] both for the AIM and other Green's function schemes for solving impurity models [61, 62]. The CC approach solves the corresponding

many-body problem by considering a subset of excitations from a reference state $|\Phi\rangle$ [63–67]. This method becomes exact in the limit that all possible excitations are considered; however, the computational complexity grows polynomially in the system size N and factorially in the number of excited particles considered. Typical implementations use the Hartree-Fock solution as a reference and truncate the possible excitations to single-, double-, and sometimes triple-particle excitations (see. Fig. 2.4). These implementations achieve $\mathcal{O}(N^6)$ for CCGF based on single and double excitations and $\mathcal{O}(N^8)$ when triple excitations are added. This scaling is a significant improvement over the exponential scaling of methods like exact diagonalizaton and its non-exact variants like the Lanczos algorithm, or quantum Monte Carlo methods applied to models with a sign problem. However, for strongly correlated regimes, where many-body effect become significant, one often needs to go beyond triple excitations to obtain converged solutions [68]. In this regime, classical algorithms for computing reliable CCGFs in either the frequency or time domain become severely constrained by memory and storage requirements [69–72].

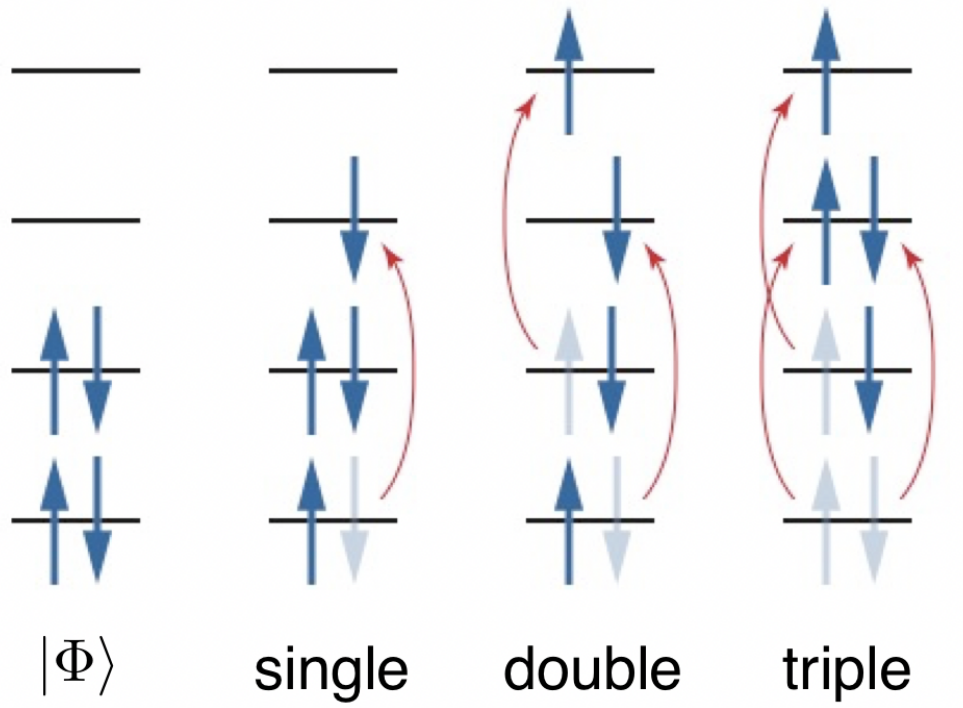

Figure 2.4: An example of a reference state $|\Phi\rangle$ and a single, double, and triple excitations from that state.

Chapter 3

Overview of Quantum Computational Simulation Methods

To perform a simulation of a quantum many-body system using a quantum computer, there are three main steps: (i) state preparation (Sec. 3.1) (ii) evolution (Sec. 3.2) and (iii) measurement (Sec. 3.3). In this chapter, I will review the most widely used methods to complete these three tasks, with special emphasis on those that I have implemented in my own work.

3.1 State Preparation

In contrast to the other subtasks in a quantum simulation, the quantum resource requirements are not as well understood for preparing a general quantum state, or even the ground state. Many Hamiltonians important to physics are k-local Hamiltonians, i.e. a Hamiltonian that can be decomposed into a sum of terms that act on at most k qubits. It has been shown that in general, for any integer $k \geq 2$, the complexity of the general k-local Hamiltonian problem (of finding the ground state energy) is QMA-complete [73–75], where QMA stands for Quantum Merlin Arthur complexity class, the quantum analog of the classical NP complexity class.

3.1.1 Variational Methods

As the name suggests, variational state preparation methods leverage the variational principle to find the desired state. In essence, variational state preparation finds the energy expectation value of some parameterized ansatz state, and then minimizes that expectation value using classical minimization methods to prepare the ground state [76–78]. These methods rely on an external classical feedback loop to drive optimization. This process is system dependent and can be very costly [79]. Nevertheless, the fact that variational state preparation can typically be performed with relatively low quantum resource overhead makes them an extremely attractive option for near term applications.

Unitary-Coupled Cluster (UCC) Ansatz

One widely used variational ansatz is inspired by the coupled cluster methods of Sec. 2.5, specifically a unitary formulation of coupled cluster aptly named the unitary coupled cluster (UCC) ansatz [77, 80]. The coupled-cluster method becomes the unitary coupled cluster method by the replacing the T of Eq. (5.4) by $T \to T - T^\dagger$, thus making T anti-hermitian, causing e^T to be unitary. In the anti-Hermitized cluster operator T, the $t^{i_1 \cdots i_k}_{a_1 \ldots a_k}$ are now the variational parameters of our ansatz and the ansatz state is given by

$$|\psi_T\rangle = e^T |\psi_i\rangle \,, \tag{3.1}$$

where $|\psi_T\rangle$ is the target state and $|\psi_i\rangle$ is the initial "guess" state. However, even if we truncate the series in Eq. (5.4) to terms with at most four fermionic operators, the number of variational parameters scales as the square of the number of occupied orbitals (n_{occ}) times the square of the number of unoccupied orbitals (n_{unocc}), $n^2_{occ} \cdot n^2_{unocc}$.

Hamiltonian Ansatz

Another commonly used ansatz is the variational Hamiltonian ansatz (VHA) [77], where the ansatz is composed of rotations by terms included in the Hamiltonian. For Hamiltonians

with relatively few and "simple" interaction terms, e.g. the Hubbard model (Sec. 2.3), this variational Hamiltonian ansatz method is particularly useful. To use UCC for the Hubbard model, on the other hand, would require a much larger circuit depth and each interaction term would be more complicated than those included in the Hubbard model directly [77]. It is worth noting that for noisy intermediate-scale quantum (NISQ) devices, the VHA has been also been studied in the presence of errors present in the quantum device [78] using a quantum simulator.

Thus far, I have reviewed the methods of preparing the ground state of a system, but there is an extension of the VQE that can be used to prepare excited states of the Hamiltonian [81].

3.1.2 Exact State Preparation Methods

In contrast to variational methods, "exact" state preparation methods are able to guarantee that the state they provide is within a given error tolerance of the true ground state. Thus, these methods can successfully produce the ground state to arbitrarily high probability. The drawback, however, is that these methods generally require more and higher quality quantum resources (more qubits, higher gate depth, etc.), making them prohibitive for use in the current NISQ era.

Quantum Phase Estimation

One exact method of state preparation is achieved by using a procedure known as quantum phase estimation (QPE) [82]. In quantum phase estimation, an ancilla register of qubits in a superposition state is required to control the application of powers of the unitary time evolution operator on the qubits encoding the state of interest. This method utilizes a quantum Fourier transform (QFT) to decode the state of the ancilla register, and thus the phase. For technical details and circuit constructions, see App. A.2.

It is often useful in practice to combine multiple state preparation procedures to improve their effectiveness. One such method combines the adiabatic method with quantum phase estimation [18]. This method also uses quantum phase estimation, but it uses adiabatic

evolution to get the state close to the desired state before using QPE to project onto the final state. This increases the chances of quantum phase estimation projecting the adiabatically evolved state onto the desired state. This method will have the same resource requirements in terms of extra qubits as quantum phase estimation, with the added issue that the adiabatic process requires the quantum device to store the state for longer without the state being destroyed.

Projection Operators

Another class of exact ground state preparation procedures use projection operators (also known as filtering or cooling functions) [83–88]. Projecting methods have recently been proposed, where some ground-state projecting operator (usually as a function of the Hamiltonian) is applied, sometimes iteratively, onto a trial state until the ground state is projected out. Filtering functions have also been used for combinatorial and search problems [89, 90]. After application of the chosen projection operator, the trial state can be guaranteed to be the ground state up to exponentially small error. Some examples of projection operators used for ground state preparation include $\cos^M(H)$ [83], H^{-k} [84], and $e^{-\frac{1}{2}t^2H^2}$ [91], where the state preparation is performed to within precision ϵ for a large enough M, k, or t (see Ch. 6 for full analysis with bounds on M and t and Ref. 84, 92 for full analysis with bounds on k). The asymptotic scalings of these algorithms depend on four things:

1. the spectral gap of the system Δ_s (corresponding to the difference in energy expectation value between the first excited and ground state) or a lower bound $\Delta \leq \Delta_s$,
2. the overlap of the initial trial state with the true ground state or a lower bound on this value γ,
3. the allowable error in final state fidelity with the true ground state η,
4. a value α that depends on the expansion of the projection operator used (see Table 6.1).

Another exact ground-state preparation method borrowed from classical simulations is quantum imaginary-time evolution (QITE) [93, 94]. This method is similar to other

projection methods in the sense that the imaginary time evolution operator $e^{-\tau H}$ is constructed and then acts on a state. Then, $e^{-\tau H}|\psi_{\text{trial}}\rangle$ becomes the ground state in the limit of infinite imaginary time. The length of imaginary time required to obtain the ground state to a given error is dependent on the spectrum of H and the initial overlap of the input state with the ground state [93, 94]. Apart from being used to prepare ground states, this method has also been utilized to prepare the thermal Gibbs state [95] given by its density matrix representation $\rho_G = \frac{1}{\mathcal{Z}} e^{-\beta H}$.

As an example of ground state preparation using projection operators, consider the method of Ref. 84 which uses the projector H^{-k} for some integer k. To improve the Harrow, Hassidim, and Lloyd (HHL) algorithm [96] for the quantum linear system problem (QLSP), Childs *et al.* [92] introduced the following Gaussian integral representation for the inverse of a nonsingular operator $\hat{H}$

$$\hat{H}^{-1} = \frac{i}{\sqrt{2\pi}} \int_0^\infty dy \int_{-\infty}^\infty dz\, z e^{-\frac{1}{2}z^2} e^{-iyz\hat{H}}. \tag{3.2}$$

Discretized in a double Riemann sum, Eq. (3.2) can be approximately implemented by the linear combinations of unitaries (LCU) method. Kyriienko [84] generalized this equation (replacing the z factor in the integrand with zy^{K-1}) to represent the operator $\hat{H}^{-K}$ for a positive integer K and used this operator to project out ground states of suitable Hamiltonians by acting with it on an initial state with a finite overlap with the true ground state. This method applies to Hamiltonians with a ground state energy having the smallest magnitude among all eigenenergies, such as Hamiltonians with a positive spectrum. For Hamiltonians with a nonpositive spectrum, Bespalova and Kyriienko [86] proposed using instead the operator $\hat{H}^K$ to project out the ground state. $\hat{H}^K$ can be expressed by a differential representation involving the time-evolution operator and the finite difference approximation to the derivatives can be evaluated by LCU [97] or quantum-classical hybrid algorithm [86, 98].

3.2 Dynamics

Once the state of interest is prepared, the next step in performing a quantum simulation is to simulate the dynamics of the system. This can have a direct effect on the simulation, e.g. finding the expected value as a function of time for some operator, or can be part of a larger simulation algorithm, e.g. in methods that involve integral transforms. Whatever the case, it is almost always necessary to have the ability to implement the time evolution operator $U(t) = e^{-iHt}$ for the Hamiltonian H under consideration. Because of this necessity, there exists numerous methods to implement the time evolution operator. In this section, I will give a brief overview of some of the most commonly employed methods, both for near term application and for future fault-tolerant devices. In this section, it is important to rewrite the Hamiltonian H as a linear combination of L terms. Throughout this section, I will use

$$H = \sum_{j=1}^{L} H_j. \tag{3.3}$$

3.2.1 Trotter-Suzuki Methods

A product formula approach approximates the exponential of a sum of operators by a product of exponentials of those same operators [99, 100], e.g. to first order

$$\exp\left[-it\sum_{j=1}^{L}\alpha_j H_j\right] \approx \left[\prod_{j=1}^{L}\exp\left(-\frac{it}{n}\,\alpha_j H_j\right)\right]^n + \mathcal{O}\left(\frac{t^2}{n^2}\right), \tag{3.4}$$

which becomes exact in the limit where $n \to \infty$. This approximation can be improved with a higher order Suzuki formula [101–103], which is defined recursively by

$$\begin{aligned} S_2(x) &\equiv \prod_{j=1}^{L}\exp(\alpha_j H_j x/2)\prod_{j=L}^{1}\exp(\alpha_j H_j x/2) \\ S_{2k}(x) &\equiv [S_{2k-2}(p_k x)]^2 S_{2k-2}((1-4p_k)x)[S_{2k-2}(p_k x)]^2. \end{aligned} \tag{3.5}$$

Here $p_k \equiv 1/(4 - 4^{1/(2k-1)})$ for $k > 1$. These approximations improve on the expected error as

$$\exp\left[-it\sum_{j=1}^{L}\alpha_j H_j\right] \approx \left[S_{2k}\left(\frac{-it}{n}\right)\right]^n + \mathcal{O}\left(\frac{t^{2k+1}}{n^{2k}}\right). \tag{3.6}$$

The error in the approximation can be found by utilizing the Baker–Campbell–Hausdorff [104] formula. When implementing these approximations, the bottleneck lies in implementing these operators with an n value large enough to get within a fixed error while maintaining a circuit depth that the device can handle. This limitation leads us to consider methods that may require more quantum resources, but have superior scaling in terms of simulation complexity.

One variation on the second order symmetric Trotter-Suzuki expansion of the time evolution operator is used for Hamiltonians that can be easily split into a kinetic and potential term, such as the Hubbard and Anderson impurity models. In this application,as described in Ref. 105, one uses a series of Givens rotations to diagonalize the kinetic part of the Hamiltonian so that the time evolution operator for the kinetic part of the Trotter expansion can be implemented with single-qubit rotations. Specifically, for systems considered in this thesis, one can separate the potential (U_c and ϵ) terms from the hopping (V) terms and implement them separately as $\mathcal{U}(t) \approx e^{-\mathrm{i}\frac{t}{2}H_{\mathrm{pot}}}e^{-\mathrm{i}tH_{\mathrm{hop}}}e^{-\mathrm{i}\frac{t}{2}H_{\mathrm{pot}}}$. By implementing a series of Givens rotations between the potential and hopping terms, the hopping terms become single qubit rotations, which must be synthesized using T gates. Note that this Trotter decomposition will require two implementations of the set of Givens rotations; a set of rotations into the diagonal basis of the hopping Hamiltonian and a set of rotations back into the computational basis.

3.2.2 The Linear Combination of Unitaries Method

The linear combination of unitary operators (LCU) method is extremely powerful and can be utilized for many different purposes, see Chaps. 5, 6. The LCU method decomposes any non-unitary operator into a linear combination of unitary operators. This technique is the underlying idea of several other simulation methods, e.g. truncated Taylor series [106]

and qubitization [107]. The basic circuit to non-deterministically implement an operator proportional to $\kappa U_a + U_b$ for any $\kappa > 0$ is shown in Fig. 3.1, where

$$V_\kappa \equiv \begin{pmatrix} \sqrt{\frac{\kappa}{\kappa+1}} & \frac{-1}{\sqrt{\kappa+1}} \\ \frac{1}{\sqrt{\kappa+1}} & \sqrt{\frac{\kappa}{\kappa+1}} \end{pmatrix}.$$

For just two operators, if we let $\Delta_U = \|U_a - U_b\|$, then this circuit fails to implement the desired linear combination of unitary operators with a failure probability of at most [108]

$$\Delta_U^2 \kappa/(\kappa+1)^2 \leq 4\kappa/(\kappa+1)^2. \tag{3.7}$$

The failure probability is due to the fact that the LCU algorithm is non-deterministic, i.e. there is a probability that the circuit will implement some operation other than the desired LCU. General linear combinations of unitary operators can be found by successively applying this procedure with a larger register of ancilla qubits that grows as $\log_2$ of the number of terms in the LCU (see Fig. 3.2). Fig. 3.1 implements the desired linear combination of the operators, which can be shown by the following direct calculation. First, assume for convenience that the unitaries in the linear combination have equal weight so that $V_\kappa \to H$ and we want to apply $U_a + U_b$. The controlled unitaries can be written as

$$|0\rangle\langle 0| \otimes U_a + |1\rangle\langle 1| \otimes U_b.$$

Then, when the controlled operators act on the state of the ancilla and system $|+\rangle \otimes |\psi\rangle$, the resulting state is

$$\frac{1}{\sqrt{2}}(|0\rangle \otimes U_a |\psi\rangle + |1\rangle \otimes U_b |\psi\rangle).$$

Applying another Hadamard gate to the ancilla qubit gives the state

$$\frac{1}{2}(|0\rangle \otimes (U_a + U_b) |\psi\rangle + |1\rangle \otimes (U_a - U_b) |\psi\rangle).$$

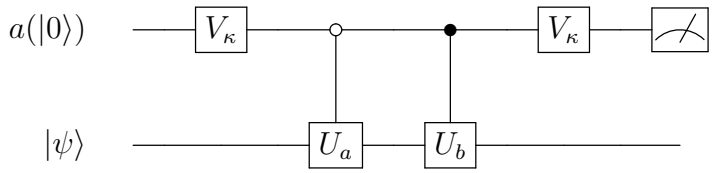

Figure 3.1: Quantum circuit to non-deterministically perform an operation proportional to $\kappa U_a + U_b$. Reproduced from Ref. [108].

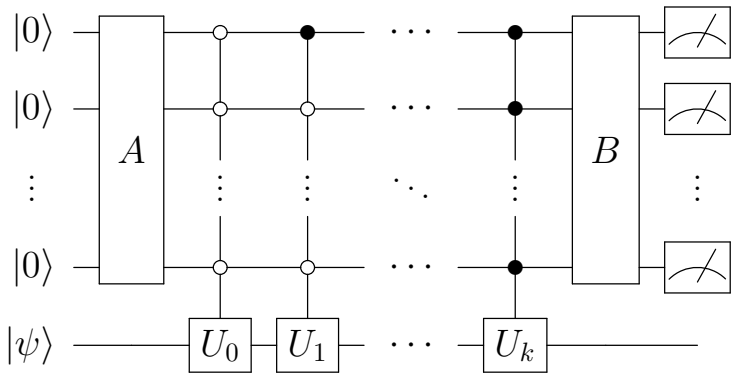

Figure 3.2: A general circuit for implementing a linear combination of $k+1$ unitary operators using ancilla preparation operator A to prepare the required $\log(k+1)$ ancilla qubits and measurement basis transformation operator B. We assume for simplicity that $k+1$ is an integer power of 2. Reproduced from Ref. [108].

Thus, if we measure the ancilla and obtain the state $|0\rangle$ from the measurement, the LCU was successfully implemented. If the measurement of the ancilla returns $|1\rangle$, the LCU failed to implement the desired operator and the procedure must be repeated. This algorithm allows time evolution to be expressed using multi-product formulas, i.e. sequences of non-unitary operators that are linear combinations of product (Trotter-Suzuki like) formulas [108].

3.2.3 The Truncated Taylor Series Method

Another method of simulating dynamics is known as the truncated Taylor series (TS) method [102, 109]. The idea is to use a truncated Taylor series up to order K to simulate the time-evolution operator $U(t) = e^{-iHt}$ corresponding to some Hamiltonian H, i.e.

$$\tilde{U}(t) \equiv \sum_{k=0}^{K} \frac{(-itH/r)^k}{k!}, \tag{3.8}$$

where r is the number of time segments in the total evolution time. If we then rewrite H as

$$H = \sum_{l=1}^{L} \alpha_l H_l$$

with each H_l a unitary operator that can be implemented and $\alpha_l > 0$. Then $\tilde{U}(t)$ can be rewritten as a linear combination of unitary operators of the form

$$\begin{aligned} \tilde{U}(t) &= \sum_{k=0}^{K} \sum_{l_1,\ldots,l_k=0}^{L} \frac{t^k}{r^k k!} \alpha_{l_1} \ldots \alpha_{l_2} (-i)^k H_{l_1} \ldots H_{l_k} \\ &= \sum_{j=0}^{\Gamma-1} \beta_j \tilde{V}_j \end{aligned} \tag{3.9}$$

where $\Gamma = \sum_{k=0}^{K} L^k$ and $\tilde{V}_j$ are unitary operators corresponding to products of the H_l's, and the β_j are the corresponding coefficients such that $\beta_j > 0$. The TS algorithm then essentially implements the linear combination in Eq. (3.9). Although this sum is not quite unitary, the error can be bounded rigorously [109].

Assuming that there is a way of implementing the unitary V_j using extra qubits (the ancillary state), then define an operation Select(V) such that, for any $j \in \{0, 1, \ldots, \Gamma - 1\}$ and any state $|\psi\rangle$,

$$\text{Select}(V) |j\rangle \otimes |\psi\rangle = |j\rangle \otimes V_j |\psi\rangle . \tag{3.10}$$

To simulate $\tilde{U}$, we need to first apply to the ancillary state a unitary operator B such that

$$B |0\rangle = \frac{1}{\sqrt{s}} \sum_{j=0}^{\Gamma-1} \sqrt{\beta_j} |j\rangle ,$$

where $s \equiv \sum_{j=0}^{\Gamma-1} \beta_j$. Then if we define

$$W \equiv (B^\dagger \otimes \mathbb{1})(\text{select}(V))(B \otimes \mathbb{1})$$

with $P \equiv |0\rangle \langle 0| \otimes \mathbb{1}$ we get that

$$PW |0\rangle |\psi\rangle = \frac{1}{s} |0\rangle \tilde{U} |\psi\rangle .$$

Note that for $T = (\alpha_1 + \cdots + \alpha_L)t$, and to be within accuracy ϵ of the true time evolution operator, this method requires an ancilla register containing $\mathcal{O}\left(\frac{\log L \log T/\epsilon}{\log \log T/\epsilon}\right)$ qubits to implement [109]. This requirement makes the truncated Taylor series method less practical than product formula methods for near-term applications. It does, however, offer superior error scaling compared to product formula implementations and requires no special structure for the Hamiltonian being simulated. It is worth mentioning that, for many systems of interest to condensed matter and quantum chemistry, the Select(V) operator can be implemented with a number of gates that grows linearly with the system size [110].

3.2.4 Quantum Signal Processing and Qubitization

Another method for constructing the time evolution operator is given by block-encoding and qubitization [107]. This method has the best known asymptotic scaling in terms of oracular

query complexity, i.e. the number of queries to an oracle that implements an operation on the quantum computer. In this context, an oracle is a black box that returns some information needed for the rest of the computation. For example, one commonly used oracle is queried and returns the desired matrix element of a given Hamiltonian. Although it is superior asymptotically, for a given use case time evolution by qubitization may not necessarily be the most optimal, especially for near-term applications. The definition of the block encoded form of a not necessarily unitary matrix A is given below [85].

Definition 3.1 (Block-Encoding)**.** *We say that a unitary matrix U is an (α, m, ϵ) encoding of $A \in \mathbb{C}^{2^n} \otimes \mathbb{C}^{2^n}$ if*

$$\|A - \alpha(\langle 0^m| \otimes \mathbb{1})U(|0^m\rangle \otimes \mathbb{1})\|_2 \leq \epsilon. \tag{3.11}$$

This definition essentially states that the matrix A has been encoded into the upper left block of an $(m+n)$ qubit matrix U, i.e. $U = \begin{pmatrix} A & \cdot \\ \cdot & \cdot \end{pmatrix}$. Qubitization assumes access to oracles that prepare the ancilla register into an arbitrary state $|G\rangle$ and implement U, along with the inverses and controlled versions of those oracles.

The block encoding method, then, allows one to obtain the block encoding of a function $f(H) = B(H) + iC(H)$, where B and C are real polynomials of degree $Q/2$ and opposite parity. To approximate the time evolution operator, one simply needs to choose polynomials B and C with proper degree $Q/2$ such that $e^{-itH} \approx B(H) + iC(H)$. It is worth noting, however, that the method as presented here only succeeds with probability $\approx \frac{1}{4}$. This success probability was remedied in a later paper by compressing the spectrum of the Hamiltonian and approximating the exponential only over the compressed spectrum [111].

3.3 Measurement of Qubits and Observables

The final part of a quantum computing simulation is to measure a value of interest, typically the expectation value of some operator. Due to the entanglement and superposition inherent to quantum computers, these expectation values are relatively easy to find when compared

to the work and resources needed to find them classically. However, in a quantum computer, reconstructing the entire quantum state from an arbitrary operation takes many repetitions of the simulation with subsequent measurements to find the final superposition, i.e. to find the density matrix. For an n qubit system, this density matrix will contain 2^{2n} elements, requiring us to recreate and measure the state $\mathcal{O}(2^{2n})$ times, thus requiring essentially the same amount of work as simulating the system classically [8]. Luckily, it is almost never necessary to fully reconstruct the quantum state when performing simulations of physical systems since the observables of interest can be can be found without reconstructing the entire quantum state.

3.3.1 Ancilla Assisted Measurement

In this section I will outline some methods that use one (or more) ancilla qubits to measure expectation values of an operator. These methods generally put the ancilla qubit(s) into a superposition, and perform an action that is controlled on the ancilla qubit(s), and targeted on the system qubits. The state of the ancilla qubit determines if the circuit is applied or not, effectively entangling the ancilla qubit with the system qubits.

The conceptually and mathematically simplest ancilla assisted measurement scheme is the so-called Hadamard test. In the Hadamard test, to measure the expected value of an operator U, a single extra qubit is required and is put into superposition with a Hadamard gate (see Sec. 1.4.2), with a controlled-U gate, then the Hadamard gate is applied again and the ancilla qubit is measured. It is straightforward to show that the Hadamard test returns the desired expectation value by direct computation:

$$\begin{aligned}
&|0\rangle_a \otimes |\psi\rangle \\
&\to H|0\rangle_a \otimes |\psi\rangle = \frac{1}{\sqrt{2}}(|0\rangle_a + |1\rangle_a) \otimes |\psi\rangle = |+\rangle \otimes |\psi\rangle \\
&\to CU_a(|+\rangle \otimes |\psi\rangle) = \frac{1}{\sqrt{2}}(|0\rangle_a \otimes |\psi\rangle + |1\rangle_a \otimes U|\psi\rangle) \\
&\to H\frac{1}{\sqrt{2}}(|0\rangle_a \otimes |\psi\rangle + |1\rangle_a \otimes U|\psi\rangle) = \frac{1}{2}(|0\rangle_a \otimes (\mathbb{1}+U)|\psi\rangle + |1\rangle_a \otimes (\mathbb{1}-U)|\psi\rangle)
\end{aligned} \tag{3.12}$$

Measuring the first qubit then gives $|0\rangle_a$ with probability $\frac{1}{4}\langle\psi|(\mathbb{1}+U^\dagger)(\mathbb{1}+U)|\psi\rangle$, and is assigned the value of 1. The measurement could also give $|1\rangle_a$ with probability $\frac{1}{4}\langle\psi|(\mathbb{1}-U^\dagger)(\mathbb{1}-U)|\psi\rangle$ and is assigned the value of -1. The expected value of the output then is the difference between the probabilities, $\frac{1}{2}\langle\psi|(U^\dagger+U)|\psi\rangle = \mathrm{Re}(\langle\psi|U|\psi\rangle)$. To obtain the imaginary part of the expected value, one just needs to apply a phase gate with the Hadamard gates such that the initial state of the ancilla qubit is $\frac{1}{\sqrt{2}}(|0\rangle_a - i|1\rangle_a)\otimes|\psi\rangle$. The measurement of more general operators as discussed next can be verified via a similar computation.

To measure a general operator of the form $\langle\psi|U^\dagger V|\psi\rangle$, we can employ an ancilla qubit [112], as shown in Fig. 3.3.

A simplification occurs (Fig. 3.4) if we want to measure an operator of the form $C_{AB} = \langle U^\dagger AUB\rangle$, e.g. a correlation function, where A and B are both expressible as a sum of unitary operators, with $A = \sum_i \alpha_i A_i,\ B = \sum_j \beta_j B_j$.

Alternatively, as described in Ref. 18, if one wishes to measure

$$\left\langle e^{itH}A^\dagger e^{-itH}B\right\rangle,$$

first prepare the ancilla in state $|+\rangle$. Then, implement controlled operations such that if the ancilla is in state $|0\rangle$, implement $e^{itH/2}B$. If it is in state $|1\rangle$, implement $e^{-itH/2}A$. Finally, measure the ancilla in the X basis to obtain $\left\langle e^{itH}A^\dagger e^{-itH}B\right\rangle$.

Analogously to the case of measuring the expectation value of a single unitary operator, there is a method that can be used to find the expectation value of a sum of unitary operators. This method utilizes multiple ancilla qubits with controlled operations that are simultaneously controlled on all of the ancillas. We can measure

$$O = \sum_{i=1}^{M} a_i\ U_i^\dagger V_i$$

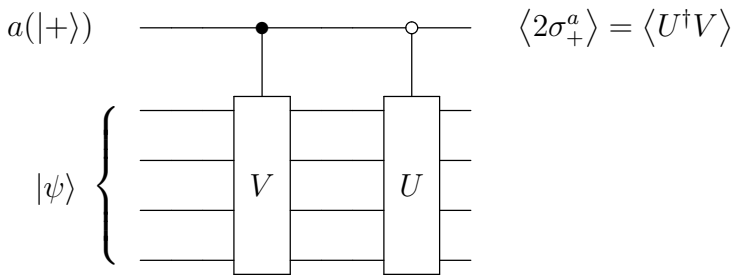

Figure 3.3: Ancilla assisted circuit to measure $\langle\psi| U^\dagger V |\psi\rangle$, reproduced from [112].

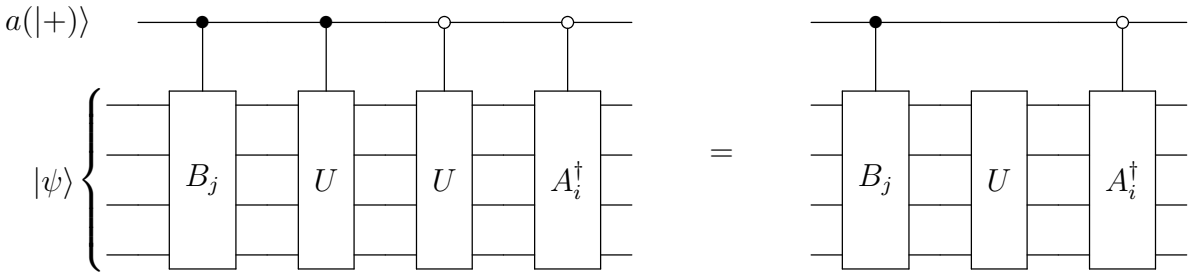

Figure 3.4: Simplification of the circuit for $\langle U^\dagger A_i U B_j \rangle$, reproduced from [112].

with only M circuits, where $a_i \geq 0$ and M is an integer power of 2. Alternatively, one can first rewrite

$$O = \mathcal{N} \sum_{i=1}^{M} \alpha_i^2 \; U_i^\dagger V_i$$

where $\mathcal{N} = \sum_{i=1}^{M} a_i$, $\alpha_i^2 = a_i/\mathcal{N}$ such that $\sum_{i=1}^{M} \alpha_i^2 = 1$. Then, measure $\langle O \rangle$ by the following procedure [112]:

1. Prepare the state $|\psi_0\rangle$ for the desired expectation value.

2. Join L ancillas to the state such that $L = J + 1$ and $2^J = M$. Put the first ancilla in state $|+\rangle$, and leave the others in state $|0\rangle$.

3. Apply a unitary $E(\alpha_1,\ \alpha_2, \ldots,\ \alpha_M)$ to the ancillas $\{a_2,\ a_3, \ldots,\ a_L\}$ to get the state $|\psi\rangle = \alpha_1 |00\ldots0\rangle + \alpha_2 |00\ldots01\rangle + \cdots + \alpha_M |11\ldots11\rangle = \sum_{i=1}^{M} \alpha_i |i\rangle$

4. Apply controlled unitary operators $\tilde{U}_i$ to evolve the system by U_i if the state of the ancillas is $|0\rangle_{a_1} |i\rangle$. Then apply controlled $\tilde{V}_i$ to evolve by V_i if the ancillas are in state $|1\rangle_{a_1} |i\rangle$. This gives a final state of $|\Psi\rangle = \frac{1}{\sqrt{2}} \left[|0\rangle_{a_1} \sum_{i=1}^{M} \alpha_i |i\rangle U_i + |1\rangle_{a_1} \sum_{i=1}^{M} \alpha_i |i\rangle V_i \right] \otimes |\Psi_0\rangle$.

5. Measure $\langle 2\sigma_+^{a_1} \rangle = 2 |0\rangle_{a_1} \langle 1| = \left\langle \sum_{i=1}^{M} \alpha_i^2 \; U_i^\dagger V_i \right\rangle$

6. Then $\langle O \rangle = \mathcal{N} \langle 2\sigma_+^{a_1} \rangle$

3.3.2 Classical Shadows

Consider again the problem of finding the expectation values $\{o_i\}$ of a set of observables $\{O_i\}$. For a density matrix of the system given by ρ, expectation values can be written as

$$o_i(\rho) = \mathrm{Tr}(O_i \rho) \tag{3.13}$$

for a finite number M observables. The classical shadow S_ρ then can be used to predict arbitrary values from Eq. (3.13) using a median of means estimation [113]. Classical shadows

are created by repeatedly applying a unitary transformation of the state such that $\rho \to U\rho U^\dagger$ and measuring in the computational basis [113]. In this case the size of shadow N, i.e. the number of times a unitary operator is applied to the state and then the state is measured in the computational basis, must be $\geq \mathcal{O}\big(\log(M) \max_i \|O_i\|^2_{\text{shadow}}/\epsilon^2\big)$ to predict M expectation values to additive error ϵ [113]. Here, the definition of the norm depends on the unitary transformations used to create the classical shadows. For example, for random Clifford measurements $\|O\|^2_{\text{shadow}} \sim \text{Tr}(O^2)$. For random Pauli measurements that are k-local, i.e. the observable O_i acts non-trivially on at most k qubits, $\|O_i\|^2_{\text{shadow}} \leq 4^k \|O_i\|^2_\infty$ [113] where the infinity norm $\|A\|_\infty = \max_{1\leq i\leq m} \sum_{j=1}^n |a_{ij}|$ for an $m \times n$ matrix A is the maximum absolute row sum of the matrix. When using the classical shadows measurement method, instead of choosing a random Pauli measurement uniformly one can locally bias the sampling from random measurement bases on each individual qubit [114], giving *locally-biased classical shadows*. In Ref. 114, the authors show how to optimize the bias of the estimator using knowledge of the observable being computed and a classical approximation of the quantum state called the reference state. The authors of Ref. 114 benchmark their method with a molecular Hamiltonian on systems up to 16 qubits and find significant improvements over the original classical shadows method. However, the locally-biased classical shadows method requires solving a convex optimization problem for the Hamiltonian in question to find appropriate probability distributions for measuring states close to the true ground state.

3.4 Green's Function Calculation Techniques

In the field of condensed matter physics, and especially when considering systems of strongly correlated electrons, one of the most desired quantities is the Green's function of the system (Sec. 2.1). In many cases, the type of information desired about the system can be extracted just from the Green's function of the system, which is much more feasible than reconstructing the entire quantum state of the system. In this section, I will outline some previously proposed methods for calculating Green's functions by leveraging quantum computers which

utilize some or all of the three main components of quantum simulation previously outlined in this section.

3.4.1 Hybrid Quantum-Classical Methods

In this section, I will outline some of the most popular and commonly used hybrid quantum-classical schemes for calculating Green's functions. These methods generally have the property that they will do the classically tractable part of the problem on the classical computer and then offload the classically intractable part to the quantum computer, which then returns the results for processing on a classical computer.

Many of these methods utilize variational methods to prepare the ground state of the system to then compute the expectation values required to construct the Green's function. For example, in Ref. 115 utilizes the unitary coupled-cluster ansatz to construct the required states and calculate the so-called "transition amplitudes" (see the numerator in Eq. 2.6) using statistical sampling. Similarly, Ref. 116 uses statistical sampling and the quantum phase estimation algorithm (Sec. 3.1.2) to calculate the generic linear response functions of an electronic system.

Another variational hybrid quantum-classical technique for calculating Green's functions uses variational quantum simulation, i.e. uses variational methods to approximate the time evolution operator acting on some reference state [117]. This method gives an efficient calculation of the Green's function in real time. The authors of Ref. 117 extend variational quantum simulation to calculate the transition amplitudes between two different quantum states after time evolution. The authors of Ref. 117 give another method for calculating the spectral function using a modified variational quantum eigensolver (VQE) to calculate excited states of the given system and again find the transition amplitudes needed to construct the spectral function representation as in Eq. (2.7).

Finally, the authors of Ref. 118 utilize a modification of VQE using "correction vector" techniques. The correction vector is prepared by an ansatz quantum circuit and classically

optimized using a sampled, variational cost function. The correction vector then gives the response of the ground state to a perturbation at a given freqeuncy.

There are methods, however, that do not utilize the variational quantum eigensolver. One hybrid quantum-classical method that I implemented on a real quantum device through IBMQ [119] and is explained in Ch. 4. This uses direct methods of applying the time evolution operator and extracting the Green's function of the two-site Anderson impurity model in the real-time domain. A better solution to this problem using newer quantum hardware, advanced Fourier transform techniques, and algebraic fast-forwarding of the time evolution operator allowed my co-authors and I [120] to map the full phase diagram of the two-site Anderson impurity model on IBMQ devices [119]. Another proposed method that avoids the use of VQE using classical coupled-cluster techniques is given in Ch. 5.

3.4.2 Fully Quantum Methods

In the near term variational based, hybrid quantum-classical methods show the most promise due to constraints on near-term quantum hardware. However, these methods will not have optimal scaling compared to purely quantum methods in the future fault-tolerant regime. In this section, I will outline some of the best known fully quantum methods for future fault-tolerant devices.

Most methods for calculating the Green's function on a fault-tolerant device attempt to do so directly in the frequency domain, i.e. by calculating Eq. (2.6) or its zero-temperature variant directly. In that case, the main computational hurdle is to construct the resolvent operator of the Hamiltonian, i.e. $R(\omega) = (\omega - \hat{H})^{-1}$. This may seem like a simple matrix inversion problem, but the interesting part of the Green's function is the poles, and matrix inversion around these poles would become intractably difficult even on a quantum computer. Thus constructing the resolvent operator is not as simple as applying the HHL algorithm [96] or its extension for matrix inversion [92] due to the dependence of the scaling on the ratio of the largest to smallest eigenvalue of the operator being inverted. There are other ways, however, of constructing an operator of this nature. Many known methods for constructing

the resolvent depend on integral transforms [91, 121, 122]. For example, in Ref. 121, the author utilizes a block-encoded (Sec. 3.2.4) form of a Gaussian integral transform to compute the spectral density of the system. In Ref. 122, the author uses a quantum Fourier transform (App. A.1) to randomly sample frequency values and obtain the diagonal component of the resolvent operator.

Although constructing the resolvent operator is a main part of constructing the Green's function, as can be seen in Eq. (2.7) it is not the only thing to be computed. To this end, in Ch. 6 I outline a method based on integral transformations and linear combinations of unitary operators to measure the full Green's function directly in the frequency domain using only quantum resources [91].

Chapter 4

Quantum-classical simulation of two-site dynamical mean-field theory on noisy quantum hardware

This chapter is reproduced from Trevor Keen *et al* 2020 *Quantum Sci. Technol.* 5 035001 [123]. The background and motivation have been edited to better fit within the larger body of work presented here. The results, data presented, and conclusions drawn remain unchanged.

4.1 Introduction

In the future, large-scale fault-tolerant quantum computers will enable direct Hamiltonian simulations of many-body systems with thousands of particles. In particular, using quantum computers for strongly correlated electron systems is a valuable and scalable solution as demonstrated by several recent theoretical analyses (see Refs. 15, 18, 124). In the current era of noisy intermediate-scale quantum (NISQ) [125] hardware, however, the number of available qubits, their connectivity, and noise prohibit direct implementations of such scalable quantum simulation algorithms. But even with all of their imperfections, NISQ devices can

still be leveraged for simulating quantum dynamics in a hybrid quantum-classical algorithmic approach. DMFT simulations (Sec. 2.4) fit naturally into such a hybrid quantum-classical scheme. In the DMFT setting, quantum hardware can be used to solve the impurity problem which is then post-processed by a classical computer to extract the value of hybridization parameters in a self-consistent manner, see Fig. 4.1. Moreover, DMFT simulations on a NISQ device are sensible because the impurity is a small part of the lattice. Thus, DMFT will require fewer qubit resources compared to a direct simulation of say, the Hubbard model. It has also been shown that DMFT's limitations, e.g. a small set of correlated orbitals and no momentum dependence of the self-energy can be overcome on quantum computers [15].

In this chapter, I present an implementation and benchmark of the two-site DMFT scheme described in Ref. 126. Specifically, we employ one of IBM's superconducting qubit chips to solve the impurity problem by measuring the impurity Green's function in the time domain, while the remainder of the DMFT self-consistency loop is executed on a classical computer. For each circuit run on the quantum computer, we execute the maximum number of shots allowed by IBM, 8192. We find that the Trotter error associated with the discretization of the time-evolution leads to inaccurate frequency estimates in the fit procedure, which in turn introduces an unphysical pole in the self-energy and incorrect quasiparticle weights. These erroneous frequencies, along with noise from the quantum chip, prevent the DMFT algorithm from converging to the correct self-consistent solution. To overcome this issue, we instead determined the quasiparticle weight by integrating the spectral function. We find that this method is much less sensitive to gate noise and Trotter error and allows the DMFT algorithm to converge to self-consistency for a half-filled Mott insulator.

A similar approach to the two-site quantum-classical DMFT simulation and its implementation on a noiseless quantum simulator was given in Ref. 127. However, only recently have implementations for existing quantum hardware begun to appear [128]. Though attempting to achieve the same goal – an implementation of two-site DMFT on a real quantum computer – the approach used in this chapter differs from that in Ref. 128 in multiple ways. For one, in this chapter a Trotterized unitary is applied to directly obtain impurity Green's function data in the time domain. In contrast, the authors in Ref. 128 use Variational Quantum

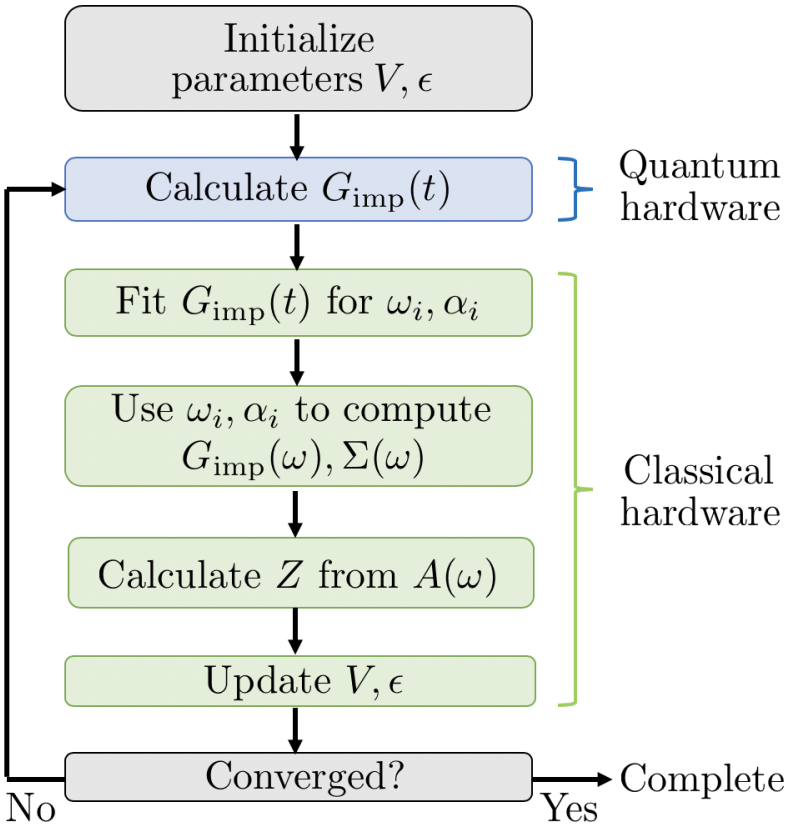

Figure 4.1: Flowchart for the two-site DMFT calculation implemented on a hybrid classical/quantum system. This loop is repeated until two successive values of V are within some threshold of each other.

Eigensolver (VQE) [129] to implement exact diagonalization. Their method depends on the scalability of the VQE to larger and more complex systems, which is not well known, and these VQE methods are meant to treat Hamiltonians with only a few noncommuting terms [15]. Also, to handle the unphysical poles in the self-energy arising from frequency shifts in the frequency domain representation of the impurity Green's function, the authors of Ref. 128 use a regularization technique to restore the frequency cancellation expected to arise in the Dyson equation. In this chapter, a different method of calculating quasiparticle weight is used instead, which is not explicitly dependent on the self-energy. Another difference is that here the DMFT loop is iterated to self-consistency, whereas Ref. 128 only states that it can be done and did not implement it.

4.2 Model & Formalism

This chapter shows an implementation of a two-site DMFT simulation of the single-band Hubbard Hamiltonian, discussed in Sec. 2.3. Recall that the DMFT method maps the single band Hubbard model of Eq. (2.14) onto an Anderson impurity model of the form in Eq. (2.15). In this case, we consider Eq. (2.14) in infinite dimensions on a Bethe lattice, i.e. a lattice in which every site is connected to all other sites. DMFT is exact in this limit when $N_{\text{bath}} \to \infty$. In what follows, however, we consider the so-called two-site problem with $N_{\text{bath}} = 1$. While it is a simplified problem, two-site DMFT allows one to recover qualitative results for the Mott transition and has been solved exactly [126].

The central quantity in DMFT is the retarded impurity Green's function of Eq. (2.16). We solve this problem for the case of a strong Coulomb repulsion at half-filling, where $\epsilon_0 - \mu = \frac{U}{2}$ and $\epsilon_1 - \mu = 0$ [126]. This simplification means that we only need to concern ourselves with the self-consistency condition for the hybridization parameter V.

Our two-site DMFT protocol is outlined in Fig. 4.1. Specifically, we carry out the following steps:

1. Fix U and $\epsilon_i - \mu$ to the values appropriate for half-filling, and initialize V to some nonzero initial value.

2. Measure the impurity Green's function of Eq. (2.16) in the time domain.

3. Fit the time domain data to obtain the $G_{\text{imp}}(\omega)$ of Eq. (2.17).

4. Obtain the spectral function from $G_{\text{imp}}(\omega)$ and the self-energy from $G^{(0)}_{\text{imp}}(\omega)$ and $G_{\text{imp}}(\omega)$.

5. Calculate the quasiparticle weight $\mathcal{Z}$ by integrating the quasiparticle peaks in the spectral function.

6. Calculate the update to the hybridization parameter V by taking the square root of $\mathcal{Z}$ (this simple square root update method is possible because of the properties of two-site DMFT and the Bethe lattice).

7. Repeat steps 2-6 with the new value of V until the new value of V matches the one from the step previous.

4.3 Methods

4.3.1 Hardware Needs & Error Mitigation

Quantum computing simulations of a fermionic system require two qubits for every orbital in the problem, each one to encode the occupancy of the up and down spins on each orbital. Our two-site DMFT protocol will therefore require four qubits. We further require an ancillary qubit and perform a single-qubit interferometry measurement scheme, as described in Refs. 127, 130, 131, bringing the total number of qubits required to five. We pick a particular subset of qubits on the device that matches the required connectivity to implement our time dynamics circuitry. There is also the circuitry required to prepare the ground state, for which we include the already chosen connectivity between qubits being used for the time dynamics circuitry, and variationally find optimal single qubit rotations between the CNOT gates allowed by connectivity (see Sec. 4.4.1 and Fig. 4.2).

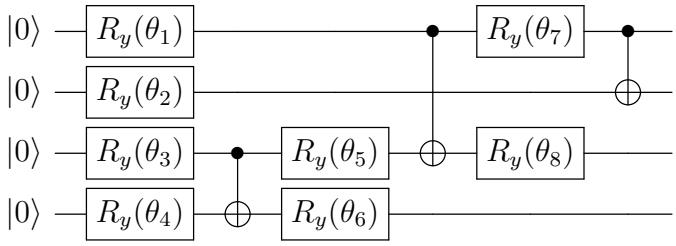

Figure 4.2: The circuit used to prepare the ground state using only three CNOT gates and eight single qubit rotations. The parameters $\{\theta_i\}$ are varied to maximize the fidelity between the output state of this circuit and the ground state of the system.

To extract the time dynamics of the impurity Green's function, we implemented the time evolution operator $U(t) = e^{-iH_{\text{AIM}}t}$ using elementary single and two-qubit gates. There are several approaches that can achieve such a decomposition. We opted to implement this using the first order Trotter-Suzuki expansion (Sec.3.2.1) as opposed to methods such as qubitization [107] reviewed in Sec. 3.2.4 or the Linear Combinations of Unitary Operations (LCU) [132–134] reviewed in Sec. 3.2.2. While both LCU and qubitization methods achieve a superior scaling in terms of the number of gates needed to implement $U(t)$ for a given t and synthesis error ϵ, we make this choice due to the hardware constraints of current quantum devices. Unlike qubitization and LCU, which require multiple ancillas and the ability to implement advanced controlled unitary operations, Trotterization can be implemented in a more resource-efficient way at the price of increased noise. We also employed several error mitigation techniques to improve our simulations. Specifically, we used the exponential error extrapolation described in Refs. [12, 13] and described in App. B.1 to reduce the noise generated by the relatively large number of CNOT gates required to implement a single Trotter step. We also applied the assignment error reduction method described in the supplementary information of Ref. 11 to characterize and correct for qubit readout (assignment) errors. This method is also reviewed in App. B.1.

4.3.2 Jordan-Wigner Transformation

To compute quantities of interest on a quantum computer, we first transformed the fermionic creation and annihilation operators to spin operators [135, 136] using the Jordan-Wigner transformation [135]. In our four qubit system (excluding the ancilla qubit used for measurement), the first two qubits encode the spin-down information for sites one and two, while the third and fourth qubits encode the corresponding information for the spin-up occupation. We then represented the creation operator as $\sigma^- = X - iY$, following Ref. 127.

After applying the Jordan-Wigner transformation, the transformed operators are

$$\begin{aligned} c_{1\downarrow}^{\dagger} &= \sigma_1^- = \frac{1}{2}\big(X_1 - iY_1\big), \\ c_{2\downarrow}^{\dagger} &= Z_1\sigma_2^- = \frac{1}{2}Z_1\big(X_2 - iY_2\big), \\ c_{1\uparrow}^{\dagger} &= Z_1Z_2\sigma_3^- = \frac{1}{2}Z_1Z_2\big(X_3 - iY_3\big), \\ c_{2\uparrow}^{\dagger} &= Z_1Z_2Z_3\sigma_4^- = \frac{1}{2}Z_1Z_2Z_3\big(X_4 - iY_4\big). \end{aligned} \tag{4.1}$$

Here, X_i, Y_i, or Z_i denote operations where a Pauli operator acts on the i^{th} qubit while identity operators act on the remaining qubits. In this representation, the two-site Anderson impurity model is given by

$$H_{\text{AIM}} = \frac{U}{4}(Z_1Z_3 - Z_1 - Z_3) + \frac{\epsilon_0 - \mu}{2}(Z_1 + Z_3) - \frac{\epsilon_1 - \mu}{2}(Z_2 + Z_4) + \frac{V}{2}(X_1X_2 + Y_1Y_2 + X_3X_4 + Y_3Y_4), \tag{4.2}$$

where we have neglected any identity terms.

4.3.3 Trotter Expansion of the time evolution operator

As mentioned in Sec. 4.3.1, we used a first order Trotter-Suzuki expansion (see Sec. 3.2.1) to implement the time evolution operator over higher order methods. The first order Trotter-Suzuki expansion [137, 138] gives

$$\begin{aligned} U(t) = e^{-iH_{\text{AIM}}t} \approx \Big(&e^{-i\frac{V}{2}(X_1X_2 + Y_1Y_2)\Delta t} e^{-i\frac{V}{2}(X_3X_4 + Y_3Y_4)\Delta t} e^{-i\frac{U}{4}Z_1Z_3\Delta t} \\ &\times e^{-i(\frac{\epsilon_0 - \mu}{2} - U/4)Z_1\Delta t} e^{-i(\frac{\epsilon_0 - \mu}{2} - U/4)Z_3\Delta t} e^{i\frac{\epsilon_1 - \mu}{2}Z_2\Delta t} e^{i\frac{\epsilon_1 - \mu}{2}Z_4\Delta t}\Big)^n + \mathcal{O}(\Delta t^2), \end{aligned} \tag{4.3}$$

where t is the total time, n is the number of time steps taken, and $\Delta t = \frac{t}{n}$. In constructing the circuits corresponding to one Trotter step, we utilized the Cartan subalgebra rotation method for each of the V terms [139–141], thus reducing CNOT gate costs for the two V terms from six CNOTs each to three CNOTs each.

4.3.4 Measurement Scheme and Procedure

To obtain the values of the impurity Green's function in the time domain, we used a single-qubit interferometry scheme, as proposed in Refs. [127, 130, 131]. We first re-write Eq. (2.16) in terms of the greater $G^{>}_{\text{imp}}(t) = -i\langle c_{0\sigma}(t)c^{\dagger}_{0\sigma}(0)\rangle$ and lesser $G^{<}_{\text{imp}}(t) = i\langle c^{\dagger}_{0\sigma}(0)c_{0\sigma}(t)\rangle$ Green's functions. We then use the Jordan-Wigner Transformation [Eq. (4.1)] to recast these as

$$\begin{aligned} G^{>}_{\text{imp}}(t) =& \frac{-i}{4}\big[\langle U^{\dagger}(t)X_1U(t)X_1\rangle - i\langle U^{\dagger}(t)X_1U(t)Y_1\rangle \\ &+ i\langle U^{\dagger}(t)Y_1U(t)X_1\rangle + \langle U^{\dagger}(t)Y_1U(t)Y_1\rangle\big] \end{aligned} \tag{4.4}$$

and

$$\begin{aligned} G^{<}_{\text{imp}}(t) =& \frac{i}{4}\big[\langle X_1U^{\dagger}(t)X_1U(t)\rangle + i\langle X_1U^{\dagger}(t)Y_1U(t)\rangle \\ &- i\langle Y_1U^{\dagger}(t)X_1U(t)\rangle + \langle Y_1U^{\dagger}(t)Y_1U(t)\rangle\big]. \end{aligned} \tag{4.5}$$

After measuring the retarded impurity Green's function $G_{\text{imp}}(t)$ at each Trotter step, we least-squares fit $iG_{\text{imp}}(t)$ on a classical computer using the the scipy package [142] and a function of the form

$$iG_{\text{imp}}(t) = 2\left[\alpha_1\cos(\omega_1 t) + \alpha_2\cos(\omega_2 t)\right], \tag{4.6}$$

which is a simplification due to the assumed particle-hole symmetry in our system [127]. The Fourier transform of Eq. (4.6) is straightforward with

$$\begin{aligned} G_{\text{imp}}(\omega + i\delta) =& \alpha_1\left(\frac{1}{\omega + i\delta + \omega_1} + \frac{1}{\omega + i\delta - \omega_1}\right) \\ &+ \alpha_2\left(\frac{1}{\omega + i\delta + \omega_2} + \frac{1}{\omega + i\delta - \omega_2}\right), \end{aligned} \tag{4.7}$$

where δ is an artificial broadening. Once self-consistency is reached and the fit parameters are obtained, we use the Dyson equation [Eq. (2.19)] to compute the self-energy and, subsequently, the spectral function $A(\omega) = -\frac{1}{\pi}\text{Im}[G_{\text{imp}}(\omega + i\delta)]$.

4.4 Results

4.4.1 Ground State Preparation

The main obstacle for performing fermionic calculations on a quantum computer lies in preparing the necessary eigenstates. The quantum phase estimation algorithm [10] will not work for the hardware we have used due to the inability to feed forward the state acquired via phase estimation to the time dynamics part of the algorithm. Instead, we use a variational approach that is well-suited to the limited connectivity of IBM's quantum chips.

Our variational state ansatz can be prepared by a shallow circuit with three CNOTs and eight single-qubit rotations (see Fig. 4.2 for details). The single-qubit rotation parameters are chosen to minimize the expectation value of the Hamiltonian H_{AIM} for given values of V, U, ϵ_i, μ. We find that this ansatz can reproduce the exact ground state (to the precision of the minimization). More specifically, our variational state has a fidelity with the exact ground state of 1 with an error on the order of 10^{-14}. When V becomes smaller than 10^{-2}, we neglect the V term and can prepare the ground state exactly.

4.4.2 Impurity Green's Function

As stated previously, the impurity Green's function is the central quantity of interest in the DMFT routine. In Fig. 3, we show the impurity Green's function in the time domain for two different sets of parameters, namely $V = t^*$ (top) and $V = 0$ (bottom) with $U = 8t^*$ for both cases. The data in Fig. 4.3 are superimposed with the fits to the data [Eq. (4.6)] and the exact solution for those parameters. In the top panel of Fig. 3 we also plot the impurity Green's function calculated with only the error introduced by the Suzuki-Trotter approximation to the Green's function. This curve is absent in the bottom plot since the Trotter error is zero for $V = 0$ and so those data points would lie directly on top of the exact curve. In both cases, there are only seven data points for $G_{\mathrm{imp}}(t)$ because the Trotter step is so expensive in terms of CNOT gates that the noise generated for more time steps and a nonzero V would overwhelm the simulation. In Fig. 4.4, we show the impurity Green's

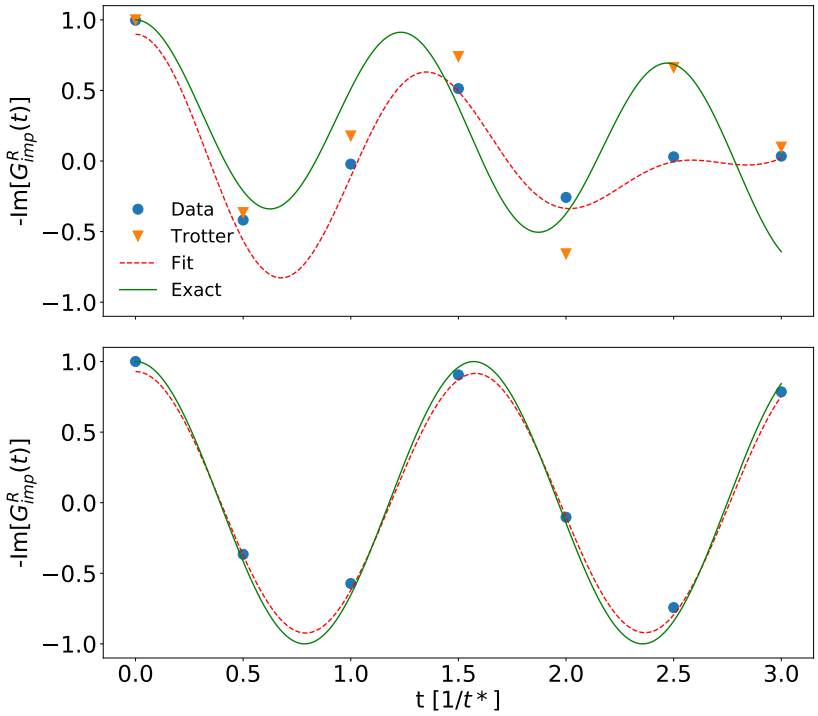

Figure 4.3: Top: Data and fit for the impurity Green's function at the first step in the self-consistency loop with $U = 8t^*$ and $V = t^*$ compared against the exact result and the result with Trotter error only. The parameters for the fit (Eq. (4.6)) shown are $\omega_1 = 4.033$, $\omega_2 = 5.197$, $\alpha_1 = 0.242$, and $\alpha_2 = 0.207$. Bottom: Data and fit for impurity Green's function at self-consistency $V = 0$ with $U = 8t^*$ plotted along with the exact result. The parameters for the fit shown are $\omega_1 = 3.980$, $\omega_2 = 2.116$, $\alpha_1 = 0.461$, and $\alpha_2 = 0.003$. Note that in the bottom plot, the calculation with Trotter error only is absent since there is no error from Trotterization when $V = 0$.

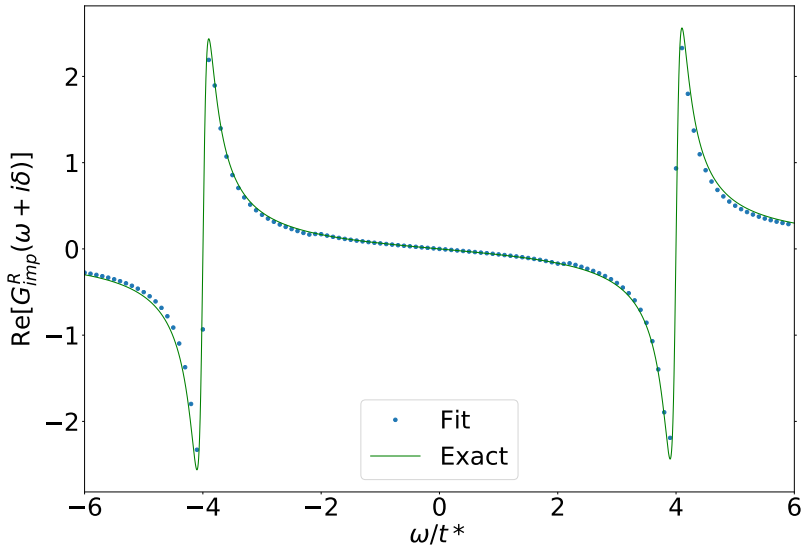

Figure 4.4: Impurity Green's function in the frequency domain for $U = 8t^*$, here calculated via Eq. (4.7) after the DMFT algorithm has converged to self-consistency. The data are compared to the exact result, and both curves assume a broadening of $\delta = 0.1$.

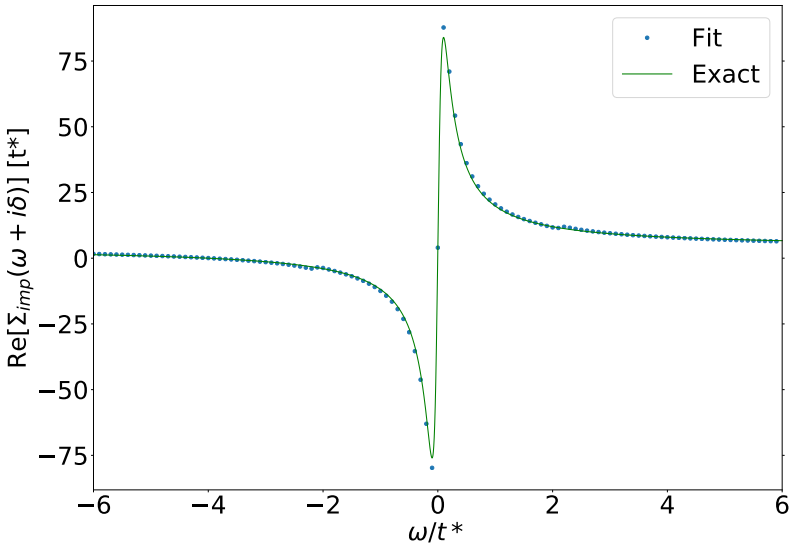

Figure 4.5: The real part of the self-energy calculated from Fig. 4.4 via Eq. (2.19). Data are shown for the fit parameters and the exact result, both with a broadening of $\delta = 0.1$.

function in the frequency domain extracted from the fit parameters [Eq. (4.7)], along with the exact solution, both obtained after self-consistency is achieved ($V = 0$). In Fig. 4.5, we display the self-energy of the system at self-consistency, calculated using Eq. (2.19) with the $G_{\text{imp}}(\omega)$ shown in Fig. 4.4. As expected for two-site DMFT at half-filling with $U > U_c = 6t^*$, at self-consistency one term in Eq. (4.6) dominates with a frequency at $\frac{U}{2}$. Due to noise, however, our self-consistent solution does not converge to exactly the right frequency (it is shifted by approximately $0.02/t^*$). Nevertheless, we still obtain good agreement with the exact solution.

4.4.3 Quasiparticle Weight Calculations

Because of the semicircular form for the density of states of the Bethe lattice in the limit of infinite coordination, the hopping parameter V in the case of a single bath level is given simply by the square root of the quasiparticle weight $V = \sqrt{\mathcal{Z}}$ [126]. The latter can be calculated from the self-energy using the relation

$$\mathcal{Z}^{-1} = 1 - \frac{d\text{Re}[\Sigma(\omega)]}{d\omega}\bigg|_{\omega=0}. \tag{4.8}$$

In practice, however, we found that the Trotter error and noise inherent to the quantum simulation result in slight shifts in the fit frequencies ω_1 and ω_2 [see Eq. (4.6)]. These errors produce extraneous peaks around $\omega = 0$ in the self-energy computed using the Dyson equation, which gives small nonzero quasiparticle weights, regardless of the other parameters. We observed that even small errors in the frequencies due to Trotterization causes unreliable derivatives and thus unreliable quasiparticle weights. This issue can be mitigated by taking more Trotter steps, but with the noise restrictions of the available quantum computers, we are restricted to approximately six Trotter steps.

To circumvent this issue, we instead integrate the quasiparticle peaks, i.e. the two peaks closest to $\omega = 0$, in the spectral function to obtain the quasiparticle weight. For example, in the top panel in Fig. 4.6, the two innermost peaks of the spectral function are visible for finite V, but for our Mott insulating case at self consistency they become very small.

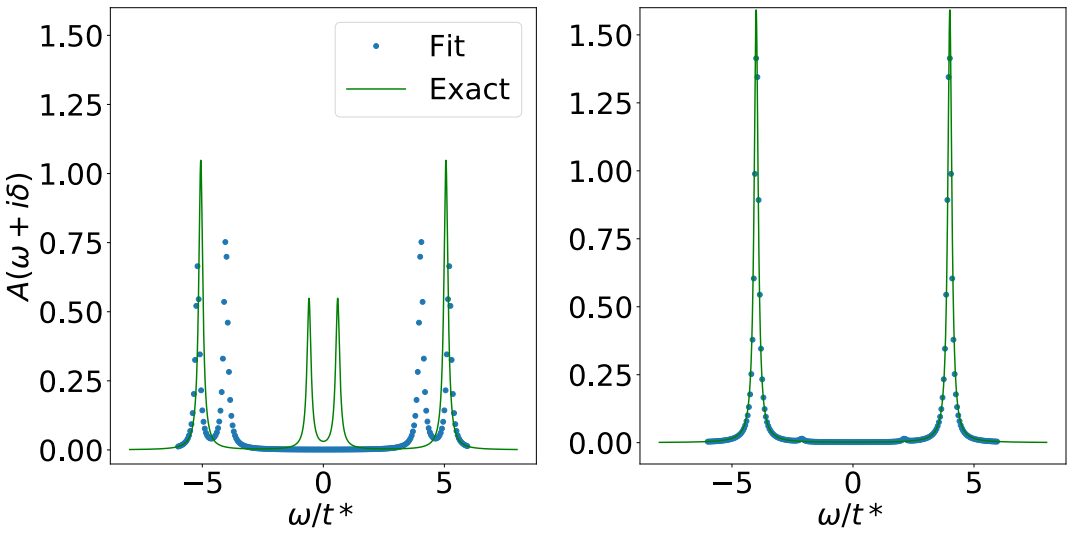

Figure 4.6: Left: The calculated spectral function after the first step of the self-consistency loop with $U = 8t^*$, $V = 1t^*$, and a broadening of $\delta = 0.1$, compared with the exact result. Right: The same spectral function after the DMFT loop has converged to $V = 0$.

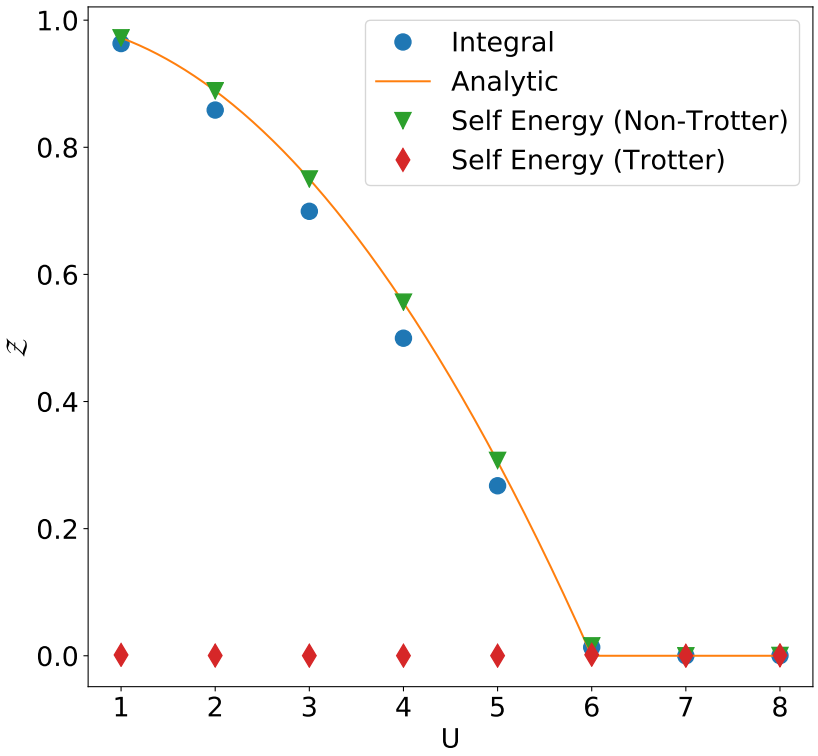

Figure 4.7: Quasiparticle weight at self-consistency as a function of U using Eq. (4.8) with fit parameters from both the Trotterized unitary (diamonds), the exact unitary fit parameters (triangles), and from integrating the low-energy peaks of the spectral function (circles) with fit parameters from the Trotterized unitary, along with the analytical result of Ref. 126 (solid line).

This method still produces inaccurate quasiparticle weights, but they are less sensitive to the shifts in frequency due to Trotter error, and accurate enough to allow us to obtain some meaningful results.

For finite values of V, the fitting procedure gives incorrect parameters when the data for $iG_{\text{imp}}(t)$ is fit to Eq. (4.6) due to the limited number of Trotter steps that we can implement. Similarly, the noise inherent to current quantum hardware has an effect on the quality of the fit. These erroneous fit parameters make the updates for the self-consistency parameters inaccurate. Because of this, we have found it difficult to converge to self-consistency when $U < U_c$ and a metallic solution ($V \neq 0$) is expected. In Fig. 4.7, we show the values of the quasiparticle weight at self-consistency for different values of U. We see that with Trotter error, the values of the quasiparticle weight calculated via Eq. (4.8) are completely unreliable. Fig. 4.7 also shows that we do not recover the exact quasiparticle weight at self-consistency for all values of U, but obtain fairly good results that are more resilient to Trotter error in comparison to any other method we attempted (see Sec. B.2), and that for our trial case of the strongly Mott insulating regime, we can recover the exact quasiparticle weight at self-consistency. It should be noted that all of the data in Fig. 4.7 was calculated on a classical computer.We are, however, able to obtain a converged solution for $U > U_c$, where a Mott insulating gap forms and at self-consistency $V = 0$, as discussed in the next section. Other methods that we attempted to employ to calculate the quasiparticle weight more reliably are given in Sec. B.2.

4.4.4 Mott Insulating Phase

For an on-site impurity Coulomb repulsion above a critical value of $U_c = 6t^*$ at half-filling ($\epsilon_0 - \mu = \frac{U}{2}$ and $\epsilon_1 - \mu = 0$), the self-consistent value of V is zero. This solution corresponds to the well known Mott insulating phase [126]. In our particular case, we set $U = 8t^*$ and took an initial guess for the hybridization parameter of $V = 1t^*$, see the top figure in Fig. 4.3 for the initial run. We then iterated our approach to the self-consistent $V = 0$ solution, with the condition that once V is sufficiently small ($V \leq 10^{-2}$), we neglected the V term and solve

what is essentially the single site problem. The bottom panel in Fig. 4.3, Figs. 4.4 and 4.5, and the bottom panel in Fig. 4.6 show the resulting impurity Green's functions, self-energy, and spectral functions, respectively, obtained once the DMFT loop has converged. This regime gives poles for the impurity Green's function at $\pm\frac{U}{2}$. Although there is no Trotter error at self-consistency for this case, noise from the quantum computer gives a small but finite value for the amplitude α_2 of the second cosine in Eq. (4.6), even though the exact solution has $\alpha_2 = 0$. This error is the origin of the small peaks located near $\omega/t^* \approx \pm 2$ in the bottom panel of Fig. 4.6. Nevertheless, our results demonstrate that the DMFT loop for the two-site problem can be iterated to convergence for parameters in the Mott insulating regime.

4.4.5 Trotter Error Analysis

As mentioned previously, we found that the Trotter error accumulated after several Trotter steps implemented on a quantum computer results in shifted frequencies obtained from the fit. This error causes a mismatch between the poles in $G^{(0)}_{\text{imp}}(\omega)$ and G_{imp}, leading to unphysical poles in the self-energy. The noise introduced by the quantum computer will exacerbate this issue. This result agrees with the findings of Ref. 128. For a Trotterized unitary such that

$$||U - U_T|| \leq \delta_T, \tag{4.9}$$

where U is the full unitary, U_T is the Trotterized unitary, and δ_T is the Trotter error. For our case, we find that the Trotter error incurred in both $G^{>}_{\text{imp}}$ and $G^{<}_{\text{imp}}$ is less than or equal to $2\delta_T$. For our first order Trotter expansion, and our relatively large time step ($\Delta t = 0.5$) required to satisfy the Nyquist criteria with a reasonable number of Trotter steps, this Trotter error is significant.

4.5 Conclusions

We have implemented an algorithm to conduct the two-site dynamical mean-field theory calculations on a quantum computer, employing multiple error mitigation strategies. Due to limited connectivity of the IBM superconducting qubit quantum computers, we use a variational ansatz to prepare the ground state of the system, greatly reducing the cost in terms of CNOT gates. We found that Trotter error and noise lead to frequencies shifted from their true values, which in turn lead to an unphysical pole in the self-energy. These aspects lead to unreliable calculations for the quasiparticle weight, and the update of the impurity-bath hybridization parameter V. These limitations prevented the DMFT algorithm from reaching self-consistency. To overcome this problem, we integrated the quasiparticle peaks in the spectral function to obtain updates to the hybridization parameter. Using this alternative method, we were able to iterate the DMFT loop to self-consistency for a strong-coupling Mott insulating phase. We were, however, unable to obtain self-consistency in the metallic phase.

Our work highlights several of the challenges in implementing quantum many body algorithms on NISQ devices. For example, to go beyond two-site DMFT with currently available quantum computing hardware, other methods will need to be employed for calculating the Green's functions, such as those proposed in [117, 143], or a more complex version of the regularization proposed in Ref. 128. In this work, we have taken for granted that the ground state of the system is known and can be efficiently prepared on a quantum computer. To do this, we introduce an ansatz and find the parameters needed using a classical computer to construct the ground state on the quantum computer. In the following chapters, however, this assumption will be relaxed and state preparation will be explored.

I was also involved in an extension of this work as part of a different project [120] which used algebraic fast-forwarding techniques to allow us to simulate the system for an arbitrary amount of time without increasing the circuit depth, thus giving much better resolution of the Green's function in the time domain. Using this increased resolution along with an analytic formula for the two-site DMFT parameter updates, we were able to map the full

phase diagram of the two-site Anderson impurity model from the low U region denoting a Mott-metallic phase through the phase transition at critical $U_c = 6$ into a Mott-insulating phase up to $U = 8$.

Chapter 5

Hybrid quantum-classical approach for coupled cluster Green's function theory

This chapter is reproduced from Trevor Keen et al. Quantum 6, 675 (2022) [144]. The background and motivation have been edited to better fit within the larger body of work presented here. The results, data presented, and conclusions drawn remain mostly unchanged.

5.1 Introduction

As discussed in Sec. 3.1, current quantum algorithms for computing zero temperature Green's functions need to prepare the many-body ground state. Their complexity depends on the size the spectral gap Δ and (or) the overlap between the ground state and the initial trial state γ, which implies prior knowledge of the system. In my previous work (Ch. 4, Ref. 123), we bypass the problem of state preparation entirely by using a variational ansatz with classically computed parameters which are then fed to the quantum computer.

Here, we introduce a unitary formulation of the classical coupled cluster (CC) method (Sec. 2.5) that can be implemented using hybrid quantum/classical computers to compute Green's functions. In contrast to other reported quantum-based Green's function

approaches [145, 146], our method does not employ the commonly-used variational quantum eigensolver (VQE). Instead, it replaces the need for preparing a many-body ground state on a quantum computer with a simpler task of applying unitary operators to a product state. This new approach thus eliminates the need for prior information about the system. While our approach is versatile and can be applied to many model Hamiltonians, we benchmark it here for the case of the Anderson Impurity model (AIM), introduced in Sec. 2.4, which lies at the heart of other widely-used many-body approaches like dynamical mean-field theory (DMFT) [42].

As with the classical CC algorithm, our hybrid quantum-classical algorithm for calculating the Green's function requires a reference state $|\Phi\rangle$; however, we have found that we can obtain accurate results for the AIM using a simple product state. This aspect replaces the need for preparing a more complicated ground state on a quantum computer with a simpler task of applying unitary operators to a product state. To achieve this, we use the single CC amplitude obtained from fully converged classical CC calculations to construct the quantum measurement of the time-evolved unitary components of the non-Hermitian coupled cluster Green's function (CCGF). This scheme allows us to extract the value of the Green's function in the time domain. Using quantum computing algorithms for unitary time dynamics via product formula methods, our formalism can then calculate the impurity Green's function of our benchmark AIM model at time t to precision $\varepsilon = \varepsilon_s + \varepsilon_m$ with a total T-gate cost of

$$\mathcal{O}\big([1 - P_f]^{-1}\sqrt{\Upsilon}\varepsilon_s^{-1/2}\sqrt{t^3}N_{\text{bath}}^5\varepsilon_m^{-2}\big).$$

Here, P_f is the probability of failing to properly implement the linear combination of unitary operators (Sec. 3.2.2), ε_s is the synthesis error introduced by the time evolution operator, t is the total evolution time, N_{bath} is the number of continuum energy levels (or "bath sites") in the AIM, ε_m is the error introduced by the measurement scheme used, and $\Upsilon = \frac{1}{12}\left[|U_c|(\sum_i |V_i|)^2 + \frac{1}{2}U_c^2\sum_i |V_i|\right]$ is a constant dependent on the parameters of the AIM. This scaling could likely be significantly improved by using more advanced time evolution techniques such as qubitization [107], but it is more difficult to analyze the full T-gate scaling

Table 5.1: Number of required ancillae and T-gate count scaling as a function of allowed error in time evolution ϵ_s, total evolution time t, and the number of bath sites N_{bath} for three common time evolution procedures. Here, we take $H = \sum_{i=1}^{L} \alpha_i H_i$, $f(\eta) = \frac{\log \eta}{\log(\log \eta)}$, $\Upsilon = \frac{1}{12}\left(|U_c|(\sum_i |V_i|)^2 + \frac{1}{2}U_c^2 \sum_i |V_i|\right)$.

Algorithm	Ref.	Ancilla Qubits	Query Complexity	Gate/Query	Total Gate Count
Trotter (Givens rotation)	105	0	-	-	$\mathcal{O}\left(\sqrt{\Upsilon}\epsilon_s^{-1/2}\sqrt{t^3}N_{\text{bath}} \log N_{\text{bath}}\right)$
Taylor Series	110, 147	$\mathcal{O}\big(\log N_{\text{bath}} f(\|\vec{\alpha}\|_1 \frac{t}{\epsilon_s})\big)$	$\mathcal{O}\big(\|\vec{\alpha}\|_1 t f(\|\vec{\alpha}\|_1 \frac{t}{\epsilon_s})\big)$	$\mathcal{O}\big(N_{\text{bath}}\big)$	$\mathcal{O}\big(\|\vec{\alpha}\|_1 t N_{\text{bath}} f(\|\vec{\alpha}\|_1 \frac{t}{\epsilon_s})\big)$
Qubitization	107, 110	$\lceil \log N_{\text{bath}} \rceil + 2$	$\mathcal{O}\big(\|\vec{\alpha}\|_1 t + f(\frac{1}{\epsilon_s})\big)$	$\mathcal{O}(N_{\text{bath}})$	$\mathcal{O}\big(N_{\text{bath}}(\|\vec{\alpha}\|_1 t + f(\frac{1}{\epsilon_s}))\big)$

of such an algorithm, and such an analysis is beyond the scope of this project. In Tab. 5.1 we give the asymptotic gate scalings of various time evolution algorithms for the single-impurity Anderson model to aid those interested in using this method with more advanced time-evolution operator techniques. While our CC method is broadly applicable to many fermionic models of interest, we demonstrate and benchmark our approach using the AIM (Sec. 2.4). In terms of comparison to classical scaling, the T-gate count of a quantum algorithm is analogous to the time complexity of a classical algorithm.

5.1.1 Coupled Cluster Green's Functions from a Sum of Unitary Operators

Given a many-body system with a model Hamiltonian H, our goal is to construct the time-dependent single-particle retarded Green's function $G^R_{pq}(t)$ with the error of at most $\varepsilon > 0$. Here, we focus on the zero-temperature case, where the retarded Green's function is given by

$$\mathrm{i}G^R_{pq}(t) = \theta(t)\,\langle \mathrm{GS}|\{c_p(t), c_q^\dagger(0)\}|\mathrm{GS}\rangle \tag{5.1}$$

Our algorithm to compute $G^R_{pq}(t)$ consists of three main components, which address ground state preparation, time evolution, and measurements. This Green's function is analogous to the impurity Green's function of Eq. (2.16) when $p = q =$ impurity. It is worth noting, however, that our method is equally useful for the advanced Green's function and in general will extend to arbitrary p, q. As discussed in the introduction, the bottleneck for many quantum or quantum- classical algorithms lies in preparing the ground state of the system. A novel aspect of our CC method is that it allows us to approximate the ground state by considering excitations from a simple product reference state $|\Phi\rangle$. Specifically, the state $|\mathrm{GS}\rangle$ is approximated by applying cluster operators to $|\Phi\rangle$ (as in classical CC methods), but the operators are approximated here by a linear combination of unitary operators, as described in greater detail below. Our full quantum-classical hybrid algorithm is summarized in Fig. 5.1.

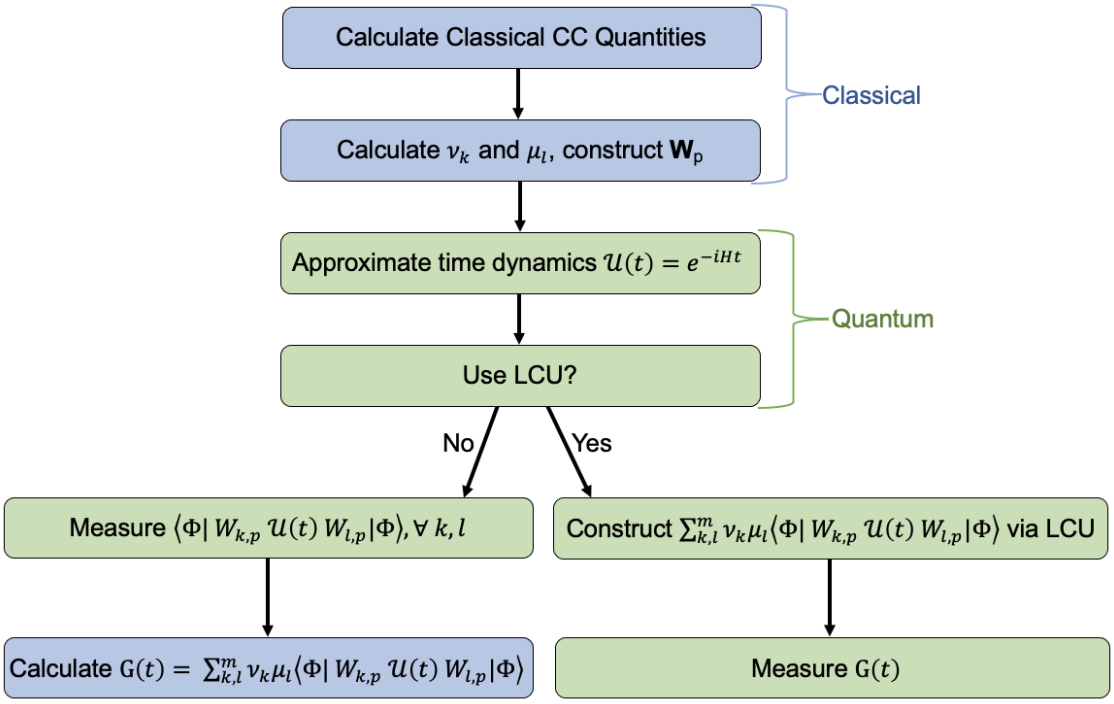

Figure 5.1: An overview of the quantum-classical coupled cluster algorithm for computing the Green's function at local site p of a fermionic model. Boxes in blue (green) indicate tasks completed on classical (quantum) computer hardware. $\mathbf{W}_p$ is the set of unitaries obtained using the CCGF fermion-to-unitary mapping.

5.1.2 State Preparation

As described in Refs. 58–60, the CCGF is built upon the CC bi-variational exponential parametrization of the reference state $|\Phi\rangle$ for approaching the many-body ground-state wave function of a system

$$|\mathrm{GS}\rangle = e^{T}\,|\Phi\rangle \tag{5.2}$$

and its dual

$$\langle \mathrm{GS}| = \langle\Phi|\,(1+\Lambda)e^{-T}, \tag{5.3}$$

where T and Λ are cluster (excitation) and de-excitation operators, respectively. In the language of second quantization, T and Λ are given by sum of multi-particle scattering operators

$$\begin{aligned} T &= \sum_{k=1}^{m} \frac{1}{(k!)^2} \sum_{\substack{i_1,\ldots,i_k;\\ a_1,\ldots,a_k}} t_{a_1\ldots a_k}^{i_1\ldots i_k} c_{a_1}^{\dagger}\cdots c_{a_k}^{\dagger} c_{i_k}\cdots c_{i_1}, \\ \Lambda &= \sum_{k=1}^{m} \frac{1}{(k!)^2} \sum_{\substack{i_1,\ldots,i_k;\\ a_1,\ldots,a_k}} \lambda_{i_1\ldots i_k}^{a_1\ldots a_k} c_{i_1}^{\dagger}\cdots c_{i_k}^{\dagger} c_{a_k}\cdots c_{a_1}. \end{aligned} \tag{5.4}$$

Here, the indices $i_1, i_2, \ldots$ $(a_1, a_2, \ldots)$ denote occupied (unoccupied) spin-orbitals in the reference $|\Phi\rangle$, the coefficients $t_{a_1\ldots a_k}^{i_1\ldots i_k}$'s and $\lambda_{i_1\ldots i_k}^{a_1\ldots a_k}$'s are scalar amplitudes, and m is the excitation level ($\leq$ number of electrons) that defines the approximation in the CC hierarchy (e.g. $m = 2$ corresponds to CC singles and doubles (CCSD) [67], $m = 3$ corresponds to CC singles, doubles, and triples (CCSDT) [148–150], etc., see Fig. 2.4).

By employing the CC bi-variational parametrization, the time-dependent CCGF for a many-body electron system can be expressed as

$$G_{pq}(t) = G_{pq}^{R}(t) + G_{pq}^{A}(t), \tag{5.5}$$

where

$$G_{pq}^{R}(t) = \langle (1+\Lambda)e^{-T} c_q^{\dagger} e^{-\mathrm{i}2\pi(H-E_{\mathrm{CC}})t} c_p e^{T}\rangle \tag{5.6}$$

is the retarded Green's function and

$$G^A_{pq}(t) = \langle (1+\Lambda) e^{-T} c_p e^{+\mathrm{i}2\pi(H-E_{\mathrm{CC}})t} c_q^\dagger e^T \rangle. \tag{5.7}$$

is the advanced time Green's function. Here, $\langle O \rangle = \langle \Phi | O | \Phi \rangle$ denotes the expectation value of an operator O with respect to the reference $|\Phi\rangle$. In the classical CCGF formulation, the operators appearing in Eqs. (5.6) and (5.7) are not unitary. This method must be modified for use on quantum computers, which require unitary operations.

We now illustrate how to develop a unitary formulation of the CC method using the lesser part $G^R_{pq}(t)$ (Eq. (5.6)). Similar considerations apply to the greater term $G^A_{pq}(t)$. We have found that at least one time-independent set of m unitaries $\mathbf{W}_p = \{W_{1,p}, W_{2,p}, \cdots, W_{m,p}\}$ can be employed to expand

$$c_p e^T |\Phi\rangle = \sum_i \mu_i W_{i,p} |\Phi\rangle \tag{5.8}$$

and

$$\langle \Phi | (1+\Lambda) e^{-T} c_q^\dagger = \sum_i \nu_i \langle \Phi | W_{i,q}^\dagger \tag{5.9}$$

with the scalar coefficients $\{\mu_i\}$ and $\{\nu_i\}$ such that Eq. (5.6) can be fully unitarized. If we limit our discussion to the CCSD framework (i.e. $T \approx T_1 + T_2 = \sum_{ai} t_i^a \hat{E}_i^a + \sum_{a<b,i<j} t_{ij}^{ab} \hat{E}_{ij}^{ab}$, where $\hat{E}_{ij\cdots}^{ab\cdots} = c_a^\dagger c_b^\dagger \cdots c_j c_i$ for $a, b \in S$ and $i, j \in O$, with S and O being the virtual and occupied subspace, respectively) and the index $p \in O$, then one option for $\mathbf{W}_p$ is (see detailed derivation in App. C.1)

$$\mathbf{W}_p = \left\{ \{\tilde{X}_p\}, \{\tilde{X}_a \tilde{X}_i \tilde{X}_p\}_{\substack{a; \\ i \neq p}}, \{\tilde{X}_a \tilde{X}_b \tilde{X}_j \tilde{X}_i \tilde{X}_p\}_{\substack{a<b, i<j; \\ i \neq p, j \neq p}} \right\}.$$

Here, $\tilde{X}_i$ denotes an X Pauli operator (or gate) acting on the i^{th} spin-orbital (or qubit) with Z Pauli operators acting on all qubits before it in our ordering, and $m \sim \mathcal{O}(N_S^2 N_O^2) \sim \mathcal{O}(N_{\mathrm{bath}}^4)$, where N_S and N_O denote the numbers of virtual and occupied spin-orbitals, respectively.

The coefficients $\{\mu_i\}$ and $\{\nu_i\}$ are given by cluster amplitudes (see App. C.1). Note that the CCSD ground state energy for a general AIM with one impurity site only depends on the single amplitude, i.e. $\Delta E_{\mathrm{CCSD}} = \sum_{i=1}^{N_{\mathrm{bath}}} V_i\, t_0^i$ since the double amplitudes in a CCSD calculation of AIM are only used to converge the single amplitudes corresponding to the excitation from the impurity to the bath. Thus, if we only use the converged T_1 amplitude to construct (or approximate) the correlated wave function, the associated ground state energy will be exactly same as the CCSD correlation energy but the number of unitary vectors m is greatly reduced from $\mathcal{O}(N_{\mathrm{bath}}^4)$ to $\mathcal{O}(N_{\mathrm{bath}})$.

Once the unitary set $\mathbf{W}_p$ and time propagator operator $\mathcal{U}(t)$ are constructed, the retarded CCGF can be expressed as

$$G_{pq}^R(t) = \sum_{k,l}^{m} \nu_k \mu_l \langle W_{k,q}^\dagger \mathcal{U}(t) W_{l,p} \rangle, \tag{5.10}$$

where the expectation values are computed using a quantum device. In the case of the AIM, the lesser CCGF for the impurity site would correspond to $p = q = 0$. Note that the gate depth for $W_{i,p}$ is just $\mathcal{O}(1)$, while the number of terms in Eq. (5.10) scales as $\mathcal{O}(m^2)$. The method(s) for constructing the time evolution operator $\mathcal{U}(t)$ and measuring the expected values in Eq. (5.10) are discussed in the next two subsections.

In analogy to the single-reference CC formulations discussed above, one can map to $\mathbf{W}_p$ other parametrizations of the ground wave function. For example, one can consider a unitary representation

$$c_p e^{\tau} |\Phi\rangle \ , \tag{5.11}$$

where τ is an anti-Hermitian cluster operator, or multi-reference CC expansions

$$c_p \sum_{\mu=1}^{M} \alpha_\mu e^{T^{(\mu)}} |\Phi_\mu\rangle \ , \tag{5.12}$$

where the coefficients α_μ define the eigenvector of the effective Hamiltonian, $\{|\Phi_\mu\rangle\}$ are reference functions defining model space, and the operators $T^{(\mu)}$ are reference-specific cluster

operators. If we choose a specific Slater determinant $|\Phi_\nu\rangle$ as a reference, other Slater determinants $|\Phi_\mu\rangle$ can be obtained as a $|\Phi_\mu\rangle = \Omega_{\mu\nu}|\Phi_\nu\rangle \quad \forall_{\mu\neq\nu}$, where the operator $\Omega_{\mu\nu}$ contains a string of creation/annihilation operators carrying active spin-orbital indices only.

5.1.3 Time evolution

There are multiple methods for approximating the time evolution operator. One option, which we adopt here for our scaling analyses, is to use a symmetrized Trotter formula with a Givens rotation, as described in Ref. 105 and Sec. 3.2.1.

For more advanced simulation methods such as qubitization [107] (Sec. 3.2.4) and Taylor series expansion [147] (Sec. 3.2.2), oracles are required. Oracle based models incur a cost based on the query complexity, i.e. the number of times an oracle must be accessed to perform the simulation. These oracles must also be constructed using basic gates and ancilla qubits, thus increasing the gate count. However, it was recently shown that the most expensive oracle to implement in the Taylor series and Qubitization methods, the Select(H) oracle, can be implemented with just $\mathcal{O}(N)$ gates [110]. For a comparison of time evolution methods in terms of gate count, see Tab. 5.1.

5.1.4 Measurement

Although the number of measurements needed to calculate the Green's function grows *quadratically* in the system size, the linear combination of the expectation values needed to calculate the impurity Green's function can be calculated in one circuit using the linear combination of unitaries (LCU) method described in Sec. 3.2.2.

We utilize the LCU method to measure each term in Eq. (5.10) with one circuit, thus reducing the measurement error. To measure the entire Green's function in the time-domain with just one circuit with LCU, we first construct the circuit that implements the LCU that is comprised of all of the terms in Eq. (5.10), and then measure the expectation value of the LCU operator with the Hadamard test (Sec. 3.3.1). It is also possible to measure each expectation value in Eq. (5.10) by using the Hadamard test with each term in an

independent circuit, and then combine them. The T-gate counts for the LCU method and the direct Hadamard test are given in the Error Analysis and Gate Count Scaling section. Because the LCU method has a failure probability, it is possible that the direct Hadamard test could be advantageous in terms of gate count, even though it has poorer scaling with respect to the system size.

We now focus on computing the local Green's function $G_{pp}(t)$ of the AIM. In this case, the circuit to measure the real part of $G_{pp}(t)$ in the time-domain via LCU is

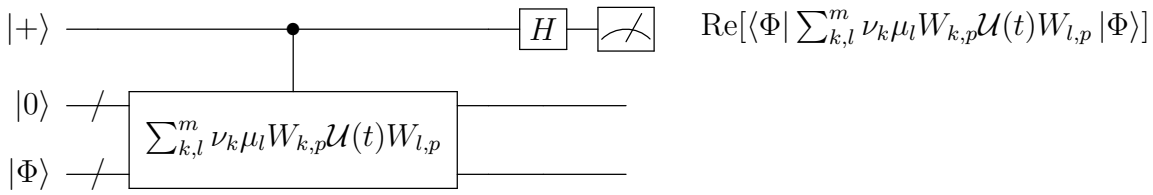

where the $\mathcal{O}(\log(N_{\mathrm{bath}}^2))$ qubit state of the ancilla register $|0\rangle$ is prepared in a state determined by the coefficients ν_k and μ_l of the LCU. The top single ancilla qubit is the one utilized for the Hadamard test. Finally, to measure the imaginary part of the expectation value instead of the real part as shown, one needs only to apply two single qubit gates to the ancilla qubit.

5.2 Results and Benchmarks

5.2.1 Two and Three-Site Examples

To demonstrate our method, we employed this hybrid quantum-classical algorithm to compute the many-body CCGF of AIM with $N_{\mathrm{bath}} = 1$ and 2 and compared our results with the exact solutions obtained with exact diagionalization.

For the $N_{\mathrm{bath}} = 1$ case, we employ four qubits on the quantum simulator within the Qiskit framework [119]. We represent the model system with qubit #1 and #3 denoting the impurity site, and use a simple reference state $|\Phi\rangle = |0110\rangle$. For the lesser CCGF, the set $\mathbf{W}_p$ ($p = 3$) then only includes two elements $\{\tilde{X}_3,\ \tilde{X}_1\tilde{X}_2\tilde{X}_3\}$, such that G^R_{imp} is given by a

linear combination of only three terms

$$G^R_{\rm imp} \Leftarrow \Big\{ \langle \tilde{X}_3 \mathcal{U}(t) \tilde{X}_3 \rangle, \langle \tilde{X}_3 \mathcal{U}(t) \tilde{X}_1 \tilde{X}_2 \tilde{X}_3 \rangle, \langle \tilde{X}_3 \tilde{X}_2 \tilde{X}_1 \mathcal{U}(t) \tilde{X}_1 \tilde{X}_2 \tilde{X}_3 \rangle \Big\} \tag{5.13}$$

with the coefficient for each term determined from the product of the elements of $\{\mu_i\}$ and $\{\nu_i\}$ $(i = 1, 2)$ as demonstrated in Eq. (5.10). The same strategy can be easily extended to an AIM with more bath levels. For example, for simulating a three-level model, six qubits can be employed to represent the model system with two qubits denoting the impurity site, and the trial state given by $|110010\rangle$. In this case, computing the lesser CCGF Green's function requires a set $\mathbf{W}_p$ $(p = 3)$ with six elements $\{\tilde{X}_3,\ \tilde{X}_5\tilde{X}_1\tilde{X}_3,\ \tilde{X}_4\tilde{X}_2\tilde{X}_3,\ \tilde{X}_6\tilde{X}_2\tilde{X}_3,\ \tilde{X}_5\tilde{X}_4\tilde{X}_2\tilde{X}_1\tilde{X}_3,\ \tilde{X}_5\tilde{X}_6\tilde{X}_2\tilde{X}_1\tilde{X}_3\}$, such that $G^R_{\rm imp}$ is given by a sum over twenty-one terms. However, based on our previous finding, these twenty-one terms can be reduced to just three terms related to only two elements of the set $\mathbf{W}_p$, $\{\tilde{X}_3, \tilde{X}_4\tilde{X}_2\tilde{X}_3\}$. This reduction is due to the fact that the CCSD ground state energy for the AIM only depends on the single excitation cluster amplitudes.

To implement the time evolution operator in our examples, we separate the potential (U_c and ϵ_i) terms from the hopping (V_i) terms and implement the former as a second order symmetric product formula similar to Eq. (3.5). However, for our two and three-site examples, we do not implement the more advanced Trotter method with Givens rotations and instead implement the terms in the second order symmetric expansion directly.

Figure 5.2 shows the impurity Green's function in the time domain for the two- (Fig. 5.2**a** and 5.2**b**) and three-site (Fig. 5.2**c** and 5.2**d**) AIM. (In both cases, our simulations were conducted for parameters that typically arise in the DMFT self-consistency loop, along with a parameter set that corresponds to the final self-consistent solution.) We then fast-fourier transform (FFT) the time domain impurity Green's function to the frequency domain to obtain the spectral functions $A_{\rm imp}(\omega) = -{\rm Im}G_{\rm imp}(\omega + {\rm i}\delta)/\pi$, as shown in Fig. 5.3. In all cases, our hybrid quantum-classical algorithm reproduces the exact solution obtained by exact diagonalization.

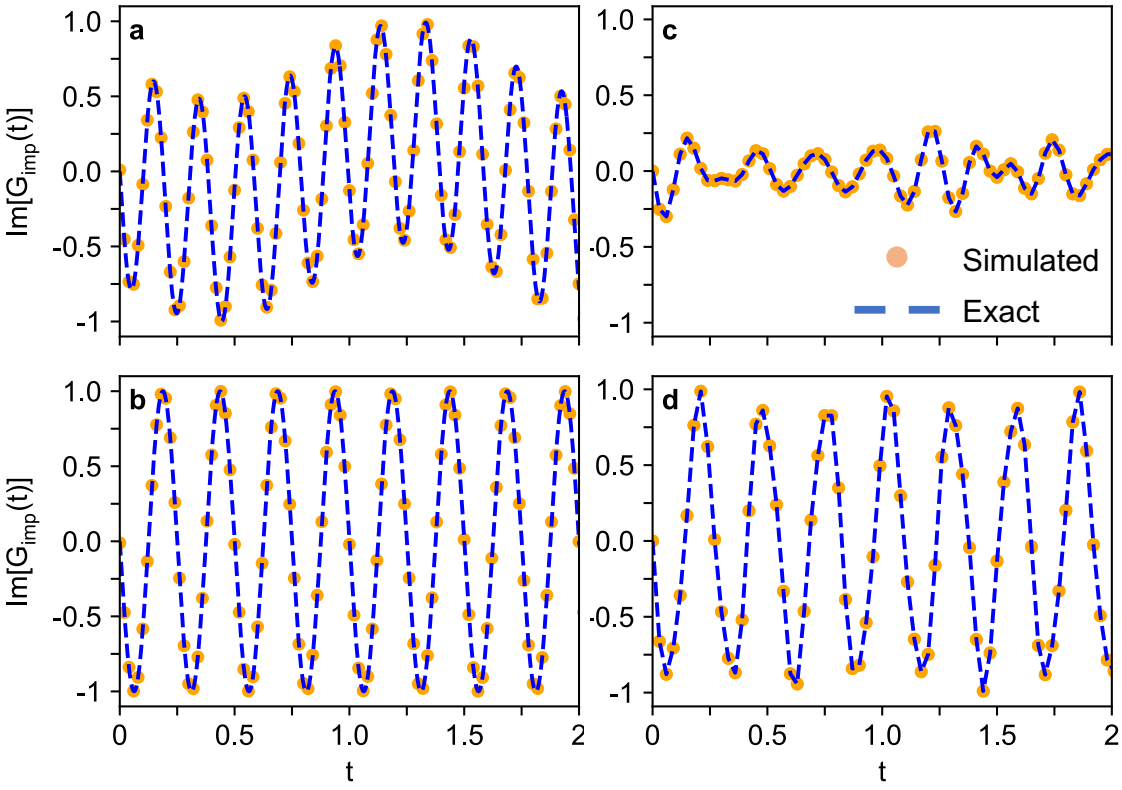

Figure 5.2: Impurity Green's function in the time domain for the AIM model with $U = 8$. The left panels show results for **a** $N_{\text{bath}} = 1$, $\epsilon_i = \{4, 0\}$, and $V_1 = 1$, and **b** $N_{\text{bath}} = 1$, $\epsilon_i = \{4, 0\}$, and $V_1 = 0$. The right panels show results for **c** $N_{\text{bath}} = 2$, $\epsilon_i = \{4, 3.61, 4.39\}$, and $V_i = \{0.63, 0.63\}$, and **d** $N_{\text{bath}} = 2$, $\epsilon_i = \{4, -0.13, 10.1\}$, and $V_i = \{1, 0.15\}$, These parameter values were selected to be representative of values that would typically arise when solving the AIM in the context of a dynamical mean-field theory algorithm.

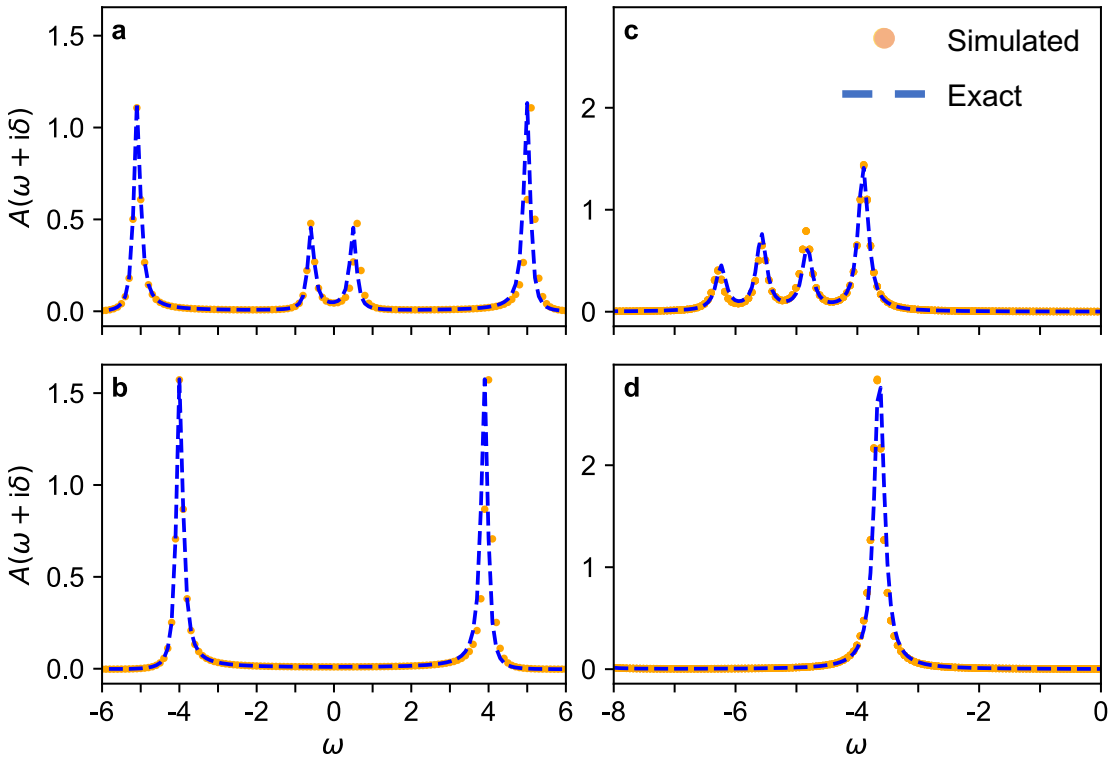

Figure 5.3: The local spectral function of the impurity site of the AIM model with $U = 8$. The left panels show results for **a** $N_{\text{bath}} = 1$, $\epsilon_i = \{4, 0\}$, and $V_1 = 1$, and **b** $N_{\text{bath}} = 1$, $\epsilon_i = \{4, 0\}$, and $V_1 = 0$. The right panels show results for **c** $N_{\text{bath}} = 2$, $\epsilon_i = \{4, 3.61, 4.39\}$, and $V_i = \{0.63, 0.63\}$, and **d** $N_{\text{bath}} = 2$, $\epsilon_i = \{4, -0.13, 10.1\}$, and $V_i = \{1, 0.15\}$, These parameter values were selected to be representative of values that would typically arise when solving the AIM in the context of a dynamical mean-field theory algorithm.

Although the examples of the two- and three-site Anderson impurity model are relatively simple, it is important to note that this method is very general. Here, we focused on the solutions of the two- and three-site problems for two sets of parameters (each) in order to emphasize that the efficacy of our approach does not depend strongly on the specific model parameters, even though the specifics of the model lead to simplifications in the method. It is also important to see the flexibility of the $\mathbf{W}_p$ operators in the construction of any form of the N-electron ground state wave functions.

5.3 Discussion

5.3.1 Advantages over VQE-based methods

Several VQE-based methods to calculate the Green's function have been proposed in the literature. For a review of the most common, see Sec. 3.4.

Our method differs from VQE-based methods in many important ways. First, we do not require any prior determination of the many-electron energy eigenvalues. Instead, we work directly in the time domain and use a Fourier transform to obtain them. Second, our method does not rely directly on classical optimization algorithms, thus bypassing the so called "barren minima" problem that can occur in VQE solutions. Third, we have flexibility in the definition of the time-independent $\mathbf{W}_p$ sets, which offers a tuning mechanism to the available quantum resources. The $\mathbf{W}_p$ sets also allow for the definition of selective sub-sets of excitations to describe correlations in the $(N \pm 1)$-electron space. This freedom could be exploited in the construction of a subspace representation of the Green's function, as is done in active-space formulations of ionization-potentials/electron-affinities equation-of-motion coupled cluster methods.

Finally, the $\mathbf{W}_p$ sets also provide great flexibility in emulating any form of the N-electron ground-state wave functions, including higher-order coupled cluster wave function expansions, configuration interaction representations, and multi-reference wave functions that may be required to handle strong correlation effects in the ground state. In this

chapter, we focused only on the single-reference CC parametrizations of the ground-state wave functions. From this perspective, the possibility of mapping arbitrary wave functions into the Pauli strings spanning the $\mathbf{W}_p$ subspace defines the universal character of the proposed quantum algorithm in dealing with various many-body systems.

5.3.2 Error Analysis and Gate Count Scaling

Suppose we want to calculate the impurity Green's function of an AIM with N_{bath} bath sites in the time domain, to within a total error ε for a total time t. We consider two main contributions to ε, namely the synthesis error ε_s from implementing the time evolution operator, and ε_m due to statistical errors in the measurement scheme. Here, we propose utilizing LCU with the Hadamard test to measure the entire impurity Green's function in the time domain with one circuit, using the Trotter (Givens rotations) method to approximate the time evolution operator. Alternatively, one could measure each expectation value in Eq. (5.10) separately with the Hadamard test, again using the Trotter (Givens rotation) method of Ref. 105 to approximate the time evolution operator. In our two-site example, we use the Hadamard test method for the convenience of implementation.

With the LCU method, for a given failure probability P_f, measurement error tolerance ε_m, and number of gates N_g required to implement the multiple controlled unitary operators, we need to use $(1 - P_f)^{-1} N_g \varepsilon_m^{-2}$ gates to successfully measure the full impurity Green's function. Here, we use the convention that the variance in a single measurement is ε_m, and grows as $\varepsilon_m = 1/\sqrt{N_s}$ with N_s the number of samples taken. In this case, the number of ancilla qubits required to implement the LCU will grow as $\mathcal{O}(\log N_{\text{bath}}^2)$, plus one ancilla for the Hadamard test. Breaking the multiple controlled qubits into basis gates requires extra "work qubits", and the number of work qubits needed grows as the number of ancillas in the control register minus one. This additional requirement does not change the asymptotic scaling of the number of ancilla qubits required; it remains $\mathcal{O}(\log N_{\text{bath}}^2)$. (See, e.g. Ref. 10 for gate construction of the multiple controlled unitaries.)

To implement the multiple controlled version of each unitary within the LCU method, $\mathcal{O}(\sqrt{\Upsilon}\varepsilon_s^{-1/2}\sqrt{t^3}N_{\text{bath}}^2)$ gates are required, where t is the total evolution time and $\Upsilon = \frac{1}{12}\left(|U_c|(\sum_i |V_i|)^2 + \frac{1}{2}U_c^2 \sum_i |V_i|\right)$ is a system-dependent factor from utilizing the Trotter decomposition of the time evolution operator. Implementing all $\mathcal{O}(N_{\text{bath}}^2)$ multiple controlled unitaries then requires $\mathcal{O}(\sqrt{\Upsilon}\varepsilon_s^{-1/2}\sqrt{t^3}N_{\text{bath}}^4)$ gates. Note, however, that *each* unitary will have some synthesis error due to the approximation of the time evolution operator and there will be $\mathcal{O}(N_{\text{bath}}^2)$ time evolution operators in the full circuit. Therefore, to maintain a maximum synthesis error of ε_s, each time evolution operator can contribute no more than $\varepsilon_s/N_{\text{bath}}^2$ error. In the above expression, substituting $\varepsilon_s \to \varepsilon_s/N_{\text{bath}}^2$ gives a total gate scaling of $\mathcal{O}(\sqrt{\Upsilon}\varepsilon_s^{-1/2}\sqrt{t^3}N_{\text{bath}}^5)$. Thus, we have a full gate count of $\mathcal{O}([1-P_f]^{-1}\sqrt{\Upsilon}\varepsilon_s^{-1/2}\sqrt{t^3}N_{\text{bath}}^5\varepsilon_m^{-2})$ to measure the impurity Green's function in the time domain. This implementation has the advantage of only requiring one circuit to measure with the Hadamard test.

If one uses the Hadamard test to measure each term in Eq. (5.10) separately, each controlled unitary will require $\mathcal{O}(\sqrt{\Upsilon}\varepsilon_s^{-1/2}\sqrt{t^3}N_{\text{bath}}^2)$ gates. Since there are $\mathcal{O}(N_{\text{bath}}^2)$ controlled unitaries to be implemented, this yields a gate complexity of $\mathcal{O}(\sqrt{\Upsilon}\varepsilon_s^{-1/2}\sqrt{t^3}N_{\text{bath}}^4)$. Since each unitary includes time evolution with some synthesis error, we again take $\varepsilon_s \to \varepsilon_s/N_{\text{bath}}^2$. Similarly, for each of the unitary operators to be measured, the measurement error ε_m grows as $1/\sqrt{N_s}$, where N_s is again the number of samples taken. Thus, to measure all of the $\mathcal{O}(N_{\text{bath}}^2)$ terms to a total measurement error ε_m, $N_s = \mathcal{O}\left(N_{\text{bath}}^2/\varepsilon_m^2\right)$ total samples are required. Substituting $\varepsilon_m \to \varepsilon_m/N_{\text{bath}}^2$ gives a total gate scaling of $\mathcal{O}(\sqrt{\Upsilon}\varepsilon_s^{-1/2}\sqrt{t^3}N_{\text{bath}}^9\varepsilon_m^{-2})$.

Figure 5.4 shows the ratio of the upper bound on the Trotter error from Ref. 105 to the actual Trotter error computed for our system in different parameter regimes for both the two and three-site systems. To obtain this figure, we compute the value of the factor Υ directly and utilize the 2-norm of the operators equal to the largest singular value.

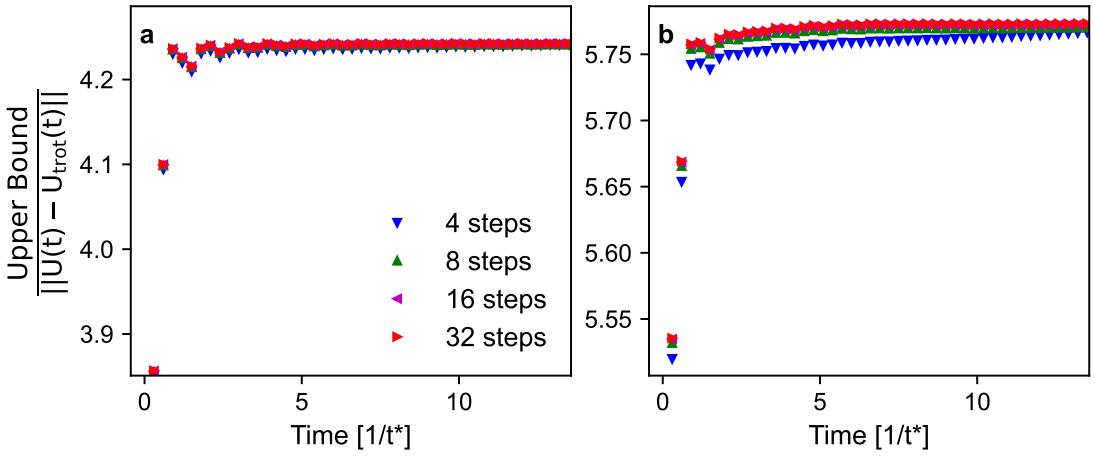

Figure 5.4: Ratio of the upper bound on the Trotter error from Ref. 105 to the actual Trotter error for **a** $N_{\text{bath}} = 1$, $\epsilon_i = \{4, 0\}$, and $V_1 = 1$ and **b** $N_{\text{bath}} = 2$, $\epsilon_i = \{4, 3.61, 4.39\}$, and $V_i = \{0.63, 0.63\}$. For testing purposes, the size of the time steps was set to 0.03 and the number of Trotter steps used per time step is given in the legend.

5.4 Conclusions

We have presented a hybrid quantum-classical approach for calculating time-domain Green's functions of fermionic models based on coupled cluster methods. Applying this approach to the AIM, we built a rigorous but straightforward fermion-to-unitary mapping for the non-unitary CCGF exponential operators. We then combined the cluster amplitudes calculated using the classical coupled cluster algorithm with measurements of time-evolution operators on a quantum device to extract the impurity Green's function in the real-time domain. On the quantum end, this approach replaces the need to prepare the ground state and can be easily generalized to many models. Our method has a T-gate count that scales as $\mathcal{O}([1-P_f]^{-1}\sqrt{\Upsilon}\varepsilon_s^{-1/2}\sqrt{t^3}N_{\text{bath}}^5\varepsilon_m^{-2})$ with no state preparation, if we use the LCU measurement scheme outlined here with the Trotter (Givens rotation) time evolution procedure.

We demonstrated the accuracy of our approach for the two- and three-level AIM models on a quantum simulator, where we obtained results in excellent agreement with the exact solutions. Further complexity analysis of the employed second-order symmetric time-evolution operator indicates that our method has comparable scaling of the gate counts (as a function of system size) in comparison with other state-of-the-art time evolution schemes. Our work provides a novel strategy for calculating the time-domain impurity Green's function using a controlled approximation for the ground state wave function. This approach could be beneficial for situations where we know little about the ground state of the system or when the system's spectral gap is small.

Chapter 6

Quantum Algorithms for Ground-State Preparation and Green's Function Calculation

This chapter is reproduced from Trevor Keen, Eugene Dumitrescu, and Yan Wang, arXiv:2112.05731 [91]. The introduction been edited to better fit within the larger body of work presented here. The results, data presented, and conclusions drawn remain mostly unchanged.

6.1 Introduction

As discussed in Ch. 3, two of the main components of simulating a quantum system on a quantum computer are state preparation and dynamics. Although there are many methods to prepare the ground state, including those explained in Sec. 3.1, there are no methods which use a unified quantum framework for both preparing the ground state and calculating the frequency domain response function that guarantees rigorous performance. Here, we present such a unified formalism under the framework of integral transforms and the linear combinations of unitaries method (Sec. 3.2.2). The method presented here is utilized in this

work to both prepare the ground state of the system and calculate the real frequency Green's function.

To prepare the ground state of the system and compute frequency-domain Green's functions, we utilize integral transformations of the projection operator $f(\hat{H}) = e^{-\frac{1}{2}t^2\hat{H}^2}$ and the resolvent operator $R(\omega) = (\omega - \hat{H})^{-1}$. For the ground-state preparation, the Hubbard-Stratonovich integral transformation [151, 152] is applied to $f(\hat{H})$ and implemented by the linear combinations of unitaries (LCU) [108] method reviewed in Sec. 3.2.2 . Our projective method saturates the optimal scaling of previous methods [83, 85] with a lower requirement on the precision of the ground-state energy than reported in Ge *et al.* [83]. Our second result is a quantum algorithm for implementing the resolvent operator to compute single-particle Green's function. This algorithm is based on a Fourier-Laplace integral transform (FIT) used in conjunction with the LCU, and it essentially only uses quantum resources, in contrast to variational [118, 153] and QPE [115, 116, 154] methods. Figure 6.1 shows a diagram of our unified integral transform framework and how it applies to our test cases of ground state preparation and response function calculation. Ref. 155 treats the Green's function calculation as a matrix inversion problem. However, this method has an inverse linear dependence on the smallest singular value of the resolvent matrix, which can become very small for certain systems. This is an issue which our method entirely avoids by treating the construction of the resolvent operator as an integral transform as opposed to an operator inversion problem. Further, although the authors of Ref. 155 provide a bound for the smallest singular value with its dependence on the broadening parameter, their bound also includes a parameter related to the block encoding of some part of the Hamiltonian. In contrast, our method uses the conceptually simpler linear combinations of unitaries method to implement a discretized integral transform of the resolvent operator, which could be done using qubitization methods. This is a matter of personal choice, and we chose to use the direct linear combinations of unitaries method to provide an easier method of implementing a unified framework of state preparation and Green's function calculation. The choice of method, as usual, depends on the use case and the desired level of abstraction and sophistication.

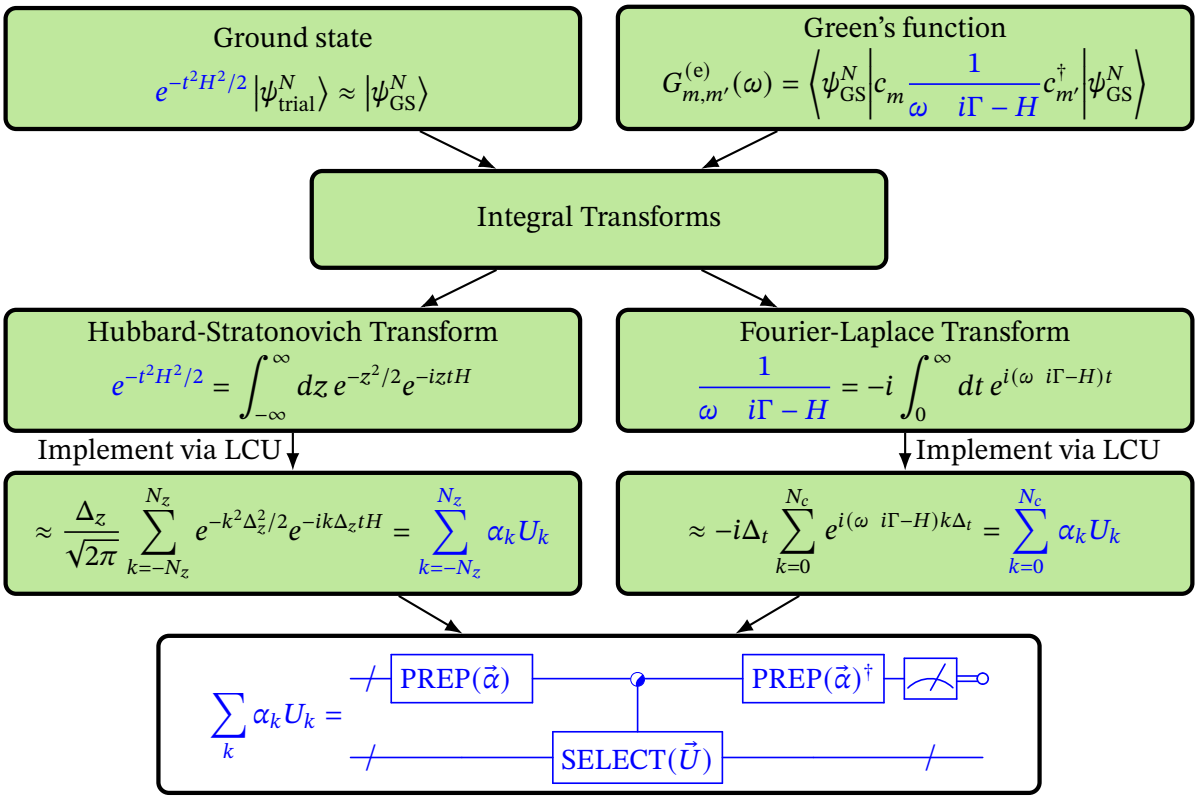

Figure 6.1: Overview of our unified framework for ground state preparation via integral transform of a ground state projection operator and integral transform of the resolvent operator. Both operators are implemented via linear combinations of unitaries (LCU) [108].

6.2 Methods

6.2.1 Projection based ground-state preparation

Recall the construction of the projection operator H^{-K} explained in Sec. 3.1.2 [84]. This method is based on a construction of H^{-1} in Eq. (3.2) with a double integral transform introduced in Ref. 92. Using the double integral representation to construct the operator $\hat{H}^{-K}$ is an overkill for ground-state projection. This can be seen as follows: dropping the z factor from the integrand (this factor is unnecessary for a positive-definite $\hat{H}$), the Gaussian z-integral in Eq. (3.2) is a Fourier transform of the Gaussian $e^{-\frac{1}{2}z^2}$ and thus, after being performed analytically, gives another Gaussian $e^{-\frac{1}{2}y^2\hat{H}^2}$. This operator can already be used for projecting out the ground state of Hamiltonians with nonnegative spectrum, without the need for a second integral transformation to obtain $\hat{H}^{-K}$.

By applying this concept to prepare our ground state, and applying the Hubbard-Stratonovich transformation [151, 152] to the ground state operator, the ground state projection operator can be defined as:

$$f(\hat{H}) = e^{-\frac{1}{2}t^2\hat{H}^2} = \frac{1}{\sqrt{2\pi}} \int_{-\infty}^{\infty} dz\, e^{-\frac{1}{2}z^2} e^{-izt\hat{H}}, \tag{6.1}$$

where variable y in Eq. (3.2) is changed to t as analogous to the imaginary time τ in the imaginary-time evolution operator $e^{-\tau\hat{H}}$. After discretizing and truncating the integral in Eq. (6.1), we apply the following approximate operator by LCU

$$h(\hat{H}) = \frac{\Delta_z}{\sqrt{2\pi}} \sum_{k=-N_z}^{N_z} e^{-\frac{1}{2}z_k^2} e^{-iz_k t\hat{H}} \equiv \sum_{k=-N_z}^{N_z} \alpha_k U_k, \tag{6.2}$$

where $(z_k = k\Delta_z)$. Since $\hat{H}^2$ instead of $\hat{H}$ is used in $f(\hat{H})$, it is the eigenstate corresponding to the eigenvalue with the smallest magnitude that is projected out. However, it is $\hat{H}$ that appears in the time-evolution unitary operators of LCU, as a result of the Hubbard-Stratonovich transformation.

Suppose that the ground energy λ_0 is only known within a given precision δ_0 to a given parameter $\bar{\lambda}_0$, i.e., $|\lambda_0 - \bar{\lambda}_0| \leq \delta_0$, and the precision satisfies $2\delta_0 < \Delta \leq \Delta_s$, where Δ is a given lower bound of the exact spectral gap Δ_s of the system. Then, the spectrum (the eigenvalue set) of $\hat{H}$ can be shifted to nonnegative domain by adding to $\hat{H}$ a constant E_c that satisfies $-\bar{\lambda}_0 + \delta_0 \leq E_c < -\bar{\lambda}_0 + \Delta/2$. The ground state of the original $\hat{H}$ now corresponds to the eigenenergy with the smallest magnitude. In addition, the shifted ground state energy $\lambda_0 + E_c$ and the first excited-state energy $\lambda_1 + E_c = \lambda_0 + \Delta_s + E_c$ satisfy $0 \leq \lambda_0 + E_c < \Delta \leq \Delta_s \leq \lambda_1 + E_c$. Next, assume that the spectrum is bounded from above so the domain of spectrum can be scaled to unity. Under these assumptions, only Hamiltonians $\hat{H}$ that have been shifted and normalized are considered, i.e., the spectrum $\sigma(\hat{H})$ is a subset of the domain $[0, 1]$.

For ground state preparation, using a sufficiently large $t = \mathcal{O}\left(\frac{1}{\Delta}\sqrt{\log \frac{1}{\gamma\eta}}\right)$ in Eq. (6.1) guarantees that the resulted state $|\psi\rangle = e^{-\frac{1}{2}t^2\hat{H}^2}|\psi_0\rangle$ is within fidelity $1-\epsilon$ to the ground state $|\lambda_0\rangle$. Here, $|\psi_0\rangle$ is a chosen trial state that has a nonzero overlap with the true ground state. This result is summarized in Lem. 1 and the proof is given in App. D.1.

Lemma 1. *Consider a Hamiltonian $\hat{H}$ with the spectrum $\sigma(\hat{H}) \subseteq [0, 1]$, the spectral gap $\Delta_s \geq \Delta > 0$, the ground state $|\lambda_0\rangle$, and the ground state energy $\lambda_0 \geq 0$. Given the operator $f(\hat{H}) = e^{-\frac{1}{2}t^2\hat{H}^2}$ and a trial state $|\psi_0\rangle$ with a fidelity $|\langle\lambda_0|\psi_0\rangle| \geq \gamma > 0$ to the ground state, the normalized state $|\psi\rangle = f(\hat{H})|\psi_0\rangle / \|f(\hat{H})|\psi_0\rangle\|$ is within fidelity $1-\epsilon$ to the ground state, that is,*

$$1 - |\langle\lambda_0|\psi\rangle| \leq \tfrac{1}{2}\||\psi\rangle - |\lambda_0\rangle\| \leq \tfrac{\eta^2}{2} \equiv \epsilon,$$

if

$$t \geq \tfrac{1}{\Delta}\sqrt{2\log\tfrac{1}{\gamma\eta}} = \mathcal{O}\left(\tfrac{1}{\Delta}\sqrt{\log\tfrac{1}{\gamma\eta}}\right).$$

When the operator $f(\hat{H})$ in Lem. 1 is implemented in the form $h(\hat{H})$ operator in Eq. (6.2) by LCU, the complexity and quantum resource cost for preparing ground state with $h(\hat{H})$ operator is summarized in Thm. 2 and the proof is given in App. D.3.

Theorem 2. *Consider a Hamiltonian $\hat{H}$ with the spectrum $\sigma(\hat{H}) \subseteq [0, 1]$, the spectral gap $\Delta_s \geq \Delta > 0$, the ground state $|\lambda_0\rangle$, and the ground energy $\lambda_0 \geq 0$. Given the LCU operator*

$h(\hat{H}) = \sum_{k=-N_z}^{N_z} \alpha_k U_k$, where $\alpha_k = \frac{\Delta_z}{\sqrt{2\pi}} e^{-\frac{1}{2}z_k^2}$, $U_k = e^{-iz_k t\hat{H}}$, and $z_k = k\Delta_z$, and a trial state $|\psi_0\rangle$ with a fidelity $|\langle\lambda_0|\psi_0\rangle| \geq \gamma > 0$ to the ground state, the normalized state $|\psi\rangle = h(\hat{H})|\psi_0\rangle / \|h(\hat{H})|\psi_0\rangle\|$ is within fidelity $1-\epsilon$ to the ground state, that is,

$$1 - |\langle\lambda_0|\psi\rangle| \leq \tfrac{1}{2}\||\psi\rangle - |\lambda_0\rangle\| \leq \tfrac{(5\eta)^2}{2} \equiv \epsilon,$$

if

$$\begin{aligned}
t &\geq \tfrac{1}{\Delta}\sqrt{2\log\tfrac{1}{\gamma\eta}} = \mathcal{O}\Big(\tfrac{1}{\Delta}\sqrt{\log\tfrac{1}{\gamma\eta}}\Big),\\
\lambda_0 &\leq \tfrac{1}{t} = \mathcal{O}\Big(\Delta/\sqrt{\log\tfrac{1}{\gamma\eta}}\Big),\\
z_c = N_z\Delta_z &\geq \sqrt{2\log\tfrac{2}{\gamma\eta}} = \mathcal{O}\Big(\sqrt{\log\tfrac{1}{\gamma\eta}}\Big),\\
\Delta_z &= \tfrac{2\pi}{z_c+t} = \mathcal{O}\Big(\Delta/\sqrt{\log\tfrac{1}{\gamma\eta}}\Big),\\
N_z &= \left\lceil \tfrac{z_c}{\Delta_z} \right\rceil = \mathcal{O}\Big(\tfrac{1}{\Delta}\log\tfrac{1}{\gamma\eta}\Big).
\end{aligned}$$

Implementing the LCU operator $h(\hat{H})$ requires $\mathcal{O}\Big(\frac{\alpha}{\gamma\Delta}\log\frac{1}{\gamma\eta}\Big)$ quantum queries to a time-evolution oracle for Hamiltonian $\hat{H}$ and $\mathcal{O}\Big(\log\frac{1}{\Delta} + \log\log\frac{1}{\gamma\eta}\Big)$ ancilla qubits using the standard formulation of LCU [156]. Here, $\alpha = \sum_{k=-N_z}^{N_z}|\alpha_k| = \mathcal{O}(1)$ is the L_1 norm of the coefficients in the LCU.

Our projective ground-state preparation algorithm presented here can be compared with the previous projective or iterative methods [83–86]. Notably, in terms of cost and efficiency, it has significant advantage over the inverse power iterative method in Ref. 84 using the operator $\hat{H}^{-K}$ by a double-integral representation. In Tab. 6.1, the asymptotic complexities of various ground-state preparation algorithms are compared in terms of the time-evolution query complexities, the required number of ancilla qubits, and the required precision to the *a priori* known ground energy. Comparing with the algorithm by Ge *et al.* [83] using the operator $\cos^M(\hat{H})$ (M is a sufficiently large integer), our method achieves very similar results. After tightening a few bounds they used to derive the original scaling and cost (see App. D.5), we find identical asymptotic scalings with that of Ref. 83. Our numerical results on the XXZ chain and Fermi-Hubbard chain confirm this identical asymptotic scaling, and our algorithm presented here shows small advantage over that of Ref. 83 in some of the examples of Hamiltonian models. Both algorithms saturate the near-optimal scaling proved

by Lin and Tong [85]. Refs. 83, 85 also extended their respective algorithms to prepare ground state with unknown ground state energy. By combining a quantum search subroutine with the ground-state projection operator, our algorithm can also be be applied in such cases by first estimating the ground energy to the required the precision, following similar strategy given in Ref. 83.

Improved scaling with spectral gap amplification

The Hubbard-Stratonovich transformation was also previously applied to prepare thermal Gibbs state [95], where a spectral-gap amplified Hamiltonian $\hat{H}_r$ satisfying $\hat{H}_r^2(|\mathbf{0}\rangle_{a_r} \otimes |\psi\rangle) = |\mathbf{0}\rangle_{a_r} \otimes (\hat{H}\,|\psi\rangle)$ is constructed using the spectral-gap amplification technique [95, 157], and the Hubbard-Stratonovich transformation is then applied to the thermal density operator as follows.

$$|\mathbf{0}\rangle_{a_r} \otimes \left(e^{-\frac{1}{2}t^2\hat{H}}\,|\psi\rangle\right) \tag{6.3a}$$

$$= \left(e^{-\frac{1}{2}t^2\hat{H}_r^2}\right)\left(|\mathbf{0}\rangle_{a_r} \otimes |\psi\rangle\right) \tag{6.3b}$$

$$= \left(\frac{1}{\sqrt{2\pi}}\int_{-\infty}^{\infty} dz\, e^{-\frac{1}{2}z^2} e^{-izt\hat{H}_r}\right)\left(|\mathbf{0}\rangle_{a_r} \otimes |\psi\rangle\right), \tag{6.3c}$$

where $|\mathbf{0}\rangle_{a_r}$ denotes the ancilla qubits for constructing the spectral-gap amplified Hamiltonian $\hat{H}_r$ whose action is equivalent to that of the square-root of $\hat{H}$. As mentioned before, in the long-imaginary time limit ($t \to \infty$), the thermal Gibbs state essentially becomes the pure ground state, so the algorithm from Ref. 95 can be directly applied to prepare the ground state. However, the operator $e^{-\frac{1}{2}t^2\hat{H}}$ alone can be used as a ground-state projection operator without applying the full thermal state preparation algorithm that carries a large amount of unnecessary cost. For frustration-free (FF) Hamiltonians, the integral transform LCU algorithm presented here and Thm. 2 are also applicable to the Hubbard-Stratonovic transformation in Eq. (6.3) involving Hamiltonian $\hat{H}_r$. Since the spectral gap of $\hat{H}_r$ is essentially $\sqrt{\Delta}$, the query complexity of our ground-state preparation algorithm combined with spectral gap amplification is reduced from $\mathcal{O}(1/\Delta)$ to $\mathcal{O}(1/\sqrt{\Delta})$, except for the cost

Table 6.1: Comparison of the complexity scaling for ground-state preparation with known ground energy. Here, α is the L_1 norm of the coefficients of the LCU, except in the case of Lin and Tong, where α refers to the $(\alpha, m, 0)$ block encoding of the Hamiltonian, Δ_s is the exact spectral gap of a given Hamiltonian, Δ is a given spectral-gap lower bound, γ is the lower bound of the overlap between the initial trial state and true ground state, and η is the additive error in the state vector.

Algorithm	**Query Complexity** $(\alpha,\ \Delta,\ \gamma,\ \eta)$	**Ancilla Qubits** $(\Delta,\ \gamma,\ \eta)$	**Required Ground Energy Precision**
Integral Transfoms+LCU (This Work)	$\mathcal{O}\left(\frac{\alpha}{\gamma\Delta}\log\frac{1}{\gamma\eta}\right)$	$\mathcal{O}\left(\log\frac{1}{\Delta}+\log\log\frac{1}{\gamma\eta}\right)$	$\mathcal{O}\left(\Delta\Big/\log^{1/2}\frac{1}{\gamma\eta}\right)$
Ge *et al.* [83]	$\mathcal{O}\left(\frac{\alpha}{\gamma\Delta}\log^{3/2}\frac{1}{\gamma\eta}\right)$	$\mathcal{O}\left(\log\frac{1}{\Delta}+\log\log\frac{1}{\gamma\eta}\right)$	$\mathcal{O}\left(\Delta\Big/\log\frac{1}{\gamma\eta}\right)$
Improved Ge *et al.* [83]	$\mathcal{O}\left(\frac{\alpha}{\gamma\Delta}\log\frac{1}{\gamma\eta}\right)$	$\mathcal{O}\left(\log\frac{1}{\Delta}+\log\log\frac{1}{\gamma\eta}\right)$	$\mathcal{O}\left(\Delta\Big/\log^{1/2}\frac{1}{\gamma\eta}\right)$
Lin and Tong [85]	$\mathcal{O}\left(\frac{\alpha}{\gamma\Delta}\log\frac{1}{\gamma\eta}\right)$	$\mathcal{O}(1)$	$\Delta\leq\Delta_{\mathrm{s}}$ $\frac{\Delta}{2}\leq\mu-\lambda_0\leq\Delta_{\mathrm{s}}-\frac{\Delta}{2}$

arising from using ancilla qubits $|\mathbf{0}\rangle_{a_r}$ to construct (i.e., block-encode) $\hat{H}_r$ and using time-evolution oracle of $\hat{H}_r$ instead of $\hat{H}$. Note that the quadratic speedup is only possible for FF Hamiltonians. Sec. 6.3.1 contains more details on the ground-state preparation of FF Hamiltonians and illustrate quadratic speedup in preparing the ground states of the FF q-deformed XXZ chain. For *nearly* FF Hamiltonians, Ref. 158 proposed a completely different algorithm giving a scaling *between* $\mathcal{O}(1/\Delta)$ and $\mathcal{O}(1/\sqrt{\Delta})$.

As described in Ch. 2, the single-particle Green's function describes the response of an interacting many-body system to the perturbation of injecting and later removing one particle. Specifically, for an N-particle system, at zero temperature $T = 0$, the retarded double-time Green's function in time domain is given by Eq. (2.10)

The double-time Green's function given in Eq. (2.10) can also be defined for more general n-body operators other than simple fermion creation and annihilation operators [1]. This leads to the general retarded linear response function

$$G^R_{AB}(t) = -i\theta(t) \left\langle \psi_0^N \middle| [\hat{A}(t), \hat{B}(0)]_\zeta \middle| \psi_0^N \right\rangle , \tag{6.4}$$

where $[\hat{A}(t), \hat{B}]_\zeta = e^{it\hat{H}'}\hat{A}e^{-it\hat{H}'}\hat{B} + \zeta \hat{B}e^{it\hat{H}'}\hat{A}e^{-it\hat{H}'}$, $\hat{H}' = \hat{H} - \mu\hat{N}$, and $\zeta = -1$ if $\hat{A}$ and $\hat{B}$ are bosonic and $\zeta = 1$ if both are fermionic. The particle rank n for the n-body operator $\hat{A}$ (or $\hat{B}$) is defined as the total number of (fermion or boson) creation and annihilation operators divided by two. If rank-n operator $\hat{A}$ is a product of fermion creation and annihilation operators, $\hat{A}$ is bosonic for integer n and fermionic for half-integer n. Eq. (6.4) reduces to the single-particle Green's function Eq. (2.10) for rank-$\frac{1}{2}$ operators $\hat{A} = \hat{c}_{j\sigma}$ and $\hat{B} = \hat{c}^\dagger_{j'\sigma'}$, while for the linear response to electromagnetic fields, such as charge and spin response functions, $\hat{A}$ and $\hat{B}$ are rank-1 operators given by a sum of products of two fermion (creation or annihilation) operators.

When the time domain Green's function $G^R_{AB}(t)$ is Fourier transformed to real-frequency domain, the resulted $G^R_{AB}(\omega)$ gives the dynamic response function. Calculating this dynamic

[1] The generalization to higher order Green's functions, such as four-time (four-point) Green's functions, is out of the scope of this paper.

response function requires construction of the resolvent operator. Methods for calculating dynamic response functions on quantum computers have been previously proposed and are reviewed in Sec. 3.4. Drastically different from many of these works, our method for computing the Green's functions does not reply on QPE; instead, after preparing the ground state using our projective algorithm introduced above, we construct the resolvent operator with LCU to compute the Green's functions. The details and complexity analysis are given in the following section.

6.2.2 Fourier-Laplace integral transform and LCU construction of resolvent operator

In the real frequency domain, the Green's function is related to the resolvent via

$$G^R_{jj'}(\omega) = \langle \psi_0^N | \hat{c}_{j'} R\Big(\omega_+ + i\Gamma, \hat{H}'\Big) \hat{c}_j^\dagger | \psi_0^N \rangle + \langle \psi_0^N | \hat{c}_j^\dagger R\Big(\omega_- + i\Gamma, -\hat{H}'\Big) \hat{c}_{j'} | \psi_0^N \rangle \,, \tag{6.5}$$

after taking the appropriate zero-temperature limit and the retarded resolvent operator is given by

$$R(\omega + i\Gamma, \hat{H}) = -i \int_0^\infty dt\, e^{i(\omega + i\Gamma - \hat{H})t}. \tag{6.6}$$

Performing the integral in Eq. (6.6) analytically we indeed obtain the usual definition of the resolvent operator,

$$R(\omega + i\Gamma, \hat{H}) = (\omega + i\Gamma - \hat{H})^{-1}. \tag{6.7}$$

Discretizing the integral in Eq. (6.6) we obtain the following LCU approximation to the resolvent operator,

$$h(\omega + i\Gamma, \hat{H}) = -i \sum_{k=0}^{N_c} \Delta_t\, e^{i(\omega + i\Gamma - \hat{H})k\Delta_t} = \sum_{k=0}^{N_c} \alpha_k U_k, \tag{6.8}$$

where $\alpha_k = \Delta_t e^{-\Gamma k \Delta_t}$ and $U_k = e^{-i[(\hat{H}-\omega)k\Delta_t + \frac{\pi}{2}]}$. The computational complexity of constructing the resolvent operator Eq. (6.6) via the LCU approximant Eq. (6.8) is summarized in Thm. 3 and the proof is given in App. D.4.

Theorem 3. *Consider a Hamiltonian H with the spectrum $\sigma(\hat{H}) \subseteq [0,1]$. Given $|\omega| \in \sigma(\hat{H})$ and an artificial broadening Γ, the resolvent operator $R(\omega + i\Gamma, \hat{H})$ can be constructed via the LCU approximant Eq. (6.8) with an additive error within ϵ, that is, $\|R(\omega + i\Gamma, \hat{H}) - h(\omega + i\Gamma, \hat{H})\| \leq \epsilon$, if $N_c = \mathcal{O}\big(\frac{1}{\Gamma\epsilon} \log \frac{2}{\Gamma\epsilon}\big)$, $\Delta_t = \min\{\epsilon/2, 3/\|\hat{H}\|\} = \mathcal{O}(\epsilon)$. Implementing the LCU approximant Eq. (6.8) requires $\mathcal{O}(\frac{1}{\Gamma^2} \log \frac{2}{\Gamma\epsilon})$ queries to a time-evolution oracle for Hamiltonian $\hat{H}$ and $\log N_c$ ancilla qubits using the standard LCU formulation [156].*

6.2.3 Quantum circuit for resolvent operator and measurements of Green's function

To simulate and measure the real-frequency domain Green's function $G^R_{jj'}(\omega)$ given in Eq. (6.5) on quantum computer, we first apply the LCU approximant Eq. (6.8) to the resolvent,

$$R(\omega_+ + i\Gamma, \hat{H}') \approx h_+ \equiv \sum_{k=0}^{N_c} \alpha_k U_k^+ = \sum_{k=0}^{N_c} (\Delta_t e^{-\Gamma k \Delta_t}) e^{-i[\hat{H} - E_0^N - \omega - \mu(\hat{N}-N)]k\Delta_t - i\frac{\pi}{2}}, \tag{6.9a}$$

$$R(\omega_- + i\Gamma, -\hat{H}') \approx h_- \equiv \sum_{k=0}^{N_c} \alpha_k U_k^- = \sum_{k=0}^{N_c} (\Delta_t e^{-\Gamma k \Delta_t}) e^{-i[-\hat{H} + E_0^N - \omega + \mu(\hat{N}-N)]k\Delta_t - i\frac{\pi}{2}}. \tag{6.9b}$$

Next, we also need to express the fermion creation and annihilation operators, $\hat{c}_j^\dagger$ and $\hat{c}_j$, in terms of unitary operators. This can be done through the following (Bogoliubov or Majorana) transformation.

$$\hat{b}_{0j} = \hat{c}_j + \hat{c}_j^\dagger, \quad \hat{b}_{1j} = i(\hat{c}_j - \hat{c}_j^\dagger). \tag{6.10}$$

It is easy to verify that for $m \in \{0,1\}$, $\hat{b}_{mj}^\dagger = \hat{b}_{mj}$ and $\hat{b}_{mj}$ is unitary, i.e., $\hat{b}_{mj}^\dagger \hat{b}_{mj} = 1$. Substituting $\hat{c}_j^\dagger = (\hat{b}_{0j} + i\hat{b}_{1j})/2$, $\hat{c}_j = (\hat{b}_{0j} - i\hat{b}_{1j})/2$, and the LCU approximant for the resolvent $R(\omega_\pm + i\Gamma, \pm\hat{H}') \approx h_\pm$ into Eq. (6.5), we obtain

$$G^R_{jj'}(\omega) \approx \left\langle \psi_0^N \middle| \hat{c}_{j'} h_+ \hat{c}_j^\dagger + \hat{c}_j^\dagger h_- \hat{c}_{j'} \middle| \psi_0^N \right\rangle, \tag{6.11a}$$

$$= \frac{1}{4} \langle \psi_0^N | \begin{pmatrix} \hat{b}_{0j'} h_+ \hat{b}_{0j} + i\hat{b}_{0j'} h_+ \hat{b}_{1j} - i\hat{b}_{1j'} h_+ \hat{b}_{0j} + \hat{b}_{1j'} h_+ \hat{b}_{1j} \\ \\ +\hat{b}_{0j} h_- \hat{b}_{0j'} - i\hat{b}_{0j} h_- \hat{b}_{1j'} + i\hat{b}_{1j} h_- \hat{b}_{0j'} + \hat{b}_{1j} h_- \hat{b}_{1j'} \end{pmatrix} | \psi_0^N \rangle . \tag{6.11b}$$

Since $h_\pm$ are LCU operators and all $\hat{b}_{mj}$ are unitary operators, each of the eight individual operators $\hat{b}_{mj} h_\pm \hat{b}_{m'j'} = \sum_{k=0}^{N_c} \alpha_k (\hat{b}_{mj} U_k^\pm \hat{b}_{m'j'})$ inside the parentheses in Eq. (6.11b) is also an LCU operator. Their sum gives an LCU expression for the operator $\left(\hat{c}_{j'} h_+ \hat{c}_j^\dagger + \hat{c}_j^\dagger h_- \hat{c}_{j'}\right)$ that completely determines the Green's function $G^R_{jj'}(\omega)$. This leads to two types of quantum circuits shown in Fig. 6.2. The circuit in panel (a) implements the sum $\left(\hat{c}_{j'} h_+ \hat{c}_j^\dagger + \hat{c}_j^\dagger h_- \hat{c}_{j'}\right)$ as a single LCU operator, while the circuit in panel (b) implements individual LCU terms, for example, $\hat{b}_{0j'} h_+ \hat{b}_{0j}$. The Green's function $G^R_{jj'}(\omega)$ is given by the expectation values of various LCU operators in the ground state. To measure such non-Hermitian operators, we use the straightforward Hadamard test as shown in Fig. 6.2. In the Hadamard test, the operator to be measured is controlled on a single ancilla qubit and the real and imaginary expected values of the operator can be obtained by measuring the ancilla qubit.

As shown in Fig. 6.2, to measure the Green's function, it involves implementing the controlled application of fermion operators c_j and $c_j^\dagger$ or rank-n operators $\hat{A}$ and $\hat{B}$ in more general cases. When these operators are expressed in a linear combination of $\mathcal{O}(2^n)$ unitaries (each unitary can be a fermionic operator from the above Bogoliubov transformation or a Pauli string operator from the Jordan-Wigner transformation), the controlled application of the LCU operator can be implemented probablistically similar to Fig. 6.2(a) and there is some quantum advantage in this case since $\mathcal{O}(n)$ ancilla qubits are sufficient even for high order (large n) correlation functions. However, the success probability of implementing the

controlled application of $\hat{A}$ and $\hat{B}$ via LCU will decrease exponentially, and the best method to boost the success probability is still an open question. Since the n-body operator $\hat{A}$ (or $\hat{B}$) and its LCU representation are far from being unitary itself for high order correlation functions, methods such as oblivious amplitude amplification [159] will fail in the extreme cases.

Alternatively, the controlled application of each individual term can be implemented deterministically similar to Fig. 6.2(b) and the measured expectation values of all terms can be summed on classical computer. For individual terms represented by Pauli strings using the Jordan-Wigner encoding of fermion operators, the number of qubits acted on by the Pauli strings can be much larger than the rank of the operators $\hat{A}$ and $\hat{B}$. For specific hardware such as trapped ions, Ref. 160 suggested using Mølmer-Sørensen gates to efficiently implement these controlled long Pauli strings.

6.3 Applications and discussion

In this section, we show numerical results using our algorithms for ground-state preparation and Green's function calculation for some of the important models in condensed matter physics, specifically the q-deformed XXZ chain in Sec. 6.3.1 and the one-dimensional Hubbard model in Sec. 6.3.2. The Hamiltonian for the q-deformed XXZ chain is frustration-free, while the Hamiltonian for the Hubbard model is frustrated. For the q-deformed XXZ chain, we only demonstrate the quadratic speedup of ground-state preparation when combining our projective method and the spectral gap amplification technique. For the Hubbad model, we give results on both ground-state preparation and Green's function calculation.

6.3.1 q-deformed XXZ chain

The frustration-free Hamiltonian for q-deformed XXZ chain [161–163] is 2-local and includes only nearest-neighbor spin-spin interactions. The Hamiltonian is given by $\hat{H} = \sum_{j=1}^{L-1} H_{j,j+1}$

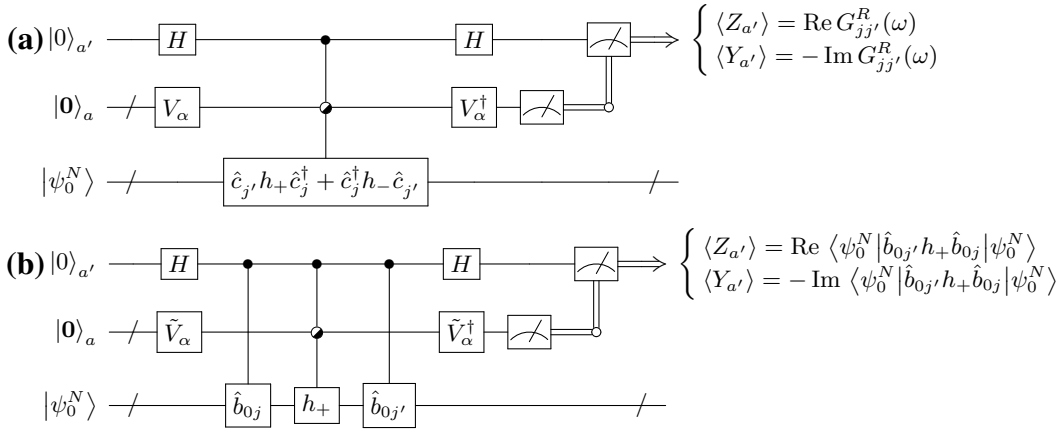

Figure 6.2: (a) Circuit for the measurement of the frequency domain Green's function $G^R_{jj'}(\omega) = \langle\psi_0^N|\big(\hat{c}_{j'}h_+\hat{c}_j^\dagger + \hat{c}_j^\dagger h_-\hat{c}_{j'}\big)|\psi_0^N\rangle$ using the Hadamard test. (b) Circuit for the measurement of a subterm of $G^R_{jj'}(\omega)$, e.g., $\langle\psi_0^N|\hat{b}_{0j'}h_+\hat{b}_{0j}|\psi_0^N\rangle$ using the Hadamard test. A single ancilla qubit $|0\rangle_{a'}$ is used for Hadamard test. The ancilla qubits $|\mathbf{0}\rangle_a$ are used for constructing LCU operators. $\tilde{V}_\alpha$ in (b) prepares the ancillary state with amplitudes given by the LCU coefficients in Eq. (6.9a), while V_α in (a) prepares a more complicated ancillary state to probabilistically implement the LCU operator $\big(\hat{c}_{j'}h_+\hat{c}_j^\dagger + \hat{c}_j^\dagger h_-\hat{c}_{j'}\big)$. The half-black-half-white controls in (a) and (b) imply a network of controls and controls-on-zero on the ancilla qubits. The gate ($\hat{c}_{j'}h_+\hat{c}_j^\dagger + \hat{c}_j^\dagger h_-\hat{c}_{j'}$ or h_+) connected to this network of controls represents a sequence of controlled unitaries corresponding to individual terms of the LCU operators. The ancilla qubit for Hadamard test is only measured when the measured outcome of the LCU ancilla system state is $|\mathbf{0}\rangle_a$.

for a L-site chain with an open boundary condition. The local term is given by [162]

$$H_{j,j+1} = \frac{-q}{2(1+q^2)}(X_jX_{j+1} + Y_jY_{j+1}) \tag{6.12}$$

$$+ \frac{1}{4}(1 - Z_jZ_{j+1}) + \frac{1-q^2}{4(1+q^2)}(Z_j - Z_{j+1}), \tag{6.13}$$

where X_j, Y_j, Z_j are Pauli matrices and the parameter $q > 0$. The last terms in all $H_{j,j+1}$ $(1 \leq j \leq L-1)$ add up to a boundary term $\frac{1-q^2}{4(1+q^2)}(Z_1 - Z_L)$ of $\hat{H}$. It is easy to verify $H_{j,j+1}^2 = 1$ so each $H_{j,j+1}$ is a projector .

For $q \neq 1$, the spectrum is gapped, including in the thermodynamic limit $(L \to \infty)$ [164]. The undeformed case $q = 1$ is a fully isotropic ferromagnetic Heisenberg chain (the boundary term also vanishes) and it is well known that the spectral gap of isotropic ferromagnetic Heisenberg chain vanishes in the thermodynamic limit [162]. However, since the spectrum is discrete for a finite chain, it is gapped, i.e., the spectral gap $\Delta_s > 0$ for any $q > 0$. For simplicity, we choose a finite number $L \in \{4, 6, 8, 10\}$ and $q = 1$ corresponding to the finite isotropic ferromagnetic Heisenberg chain, and use this model to demonstrate the quadratic speedup of ground-state preparation with our projective algorithm combined with the spectral gap amplification [95, 157]. Since each local term $H_{j,j+1}$ is a projector, it is straightforward to apply the spectral gap amplification algorithm given in Ref. 95. Specifically, the spectral-gap amplified Hamiltonian $\hat{H}_r$ introduced in Sec. 6.2.1 has the following block matrix form in the computational basis $\hat{H}_r = \left(\begin{smallmatrix} \mathbf{0} & \mathbf{\Pi} \\ \mathbf{\Pi}^\dagger & \mathbf{0} \end{smallmatrix}\right)$, where $\mathbf{\Pi} = \begin{pmatrix} H_{1,2} & H_{2,3} & \dots & H_{L-1,L} \end{pmatrix}$ is a row-vector of sub-block matrices. We use this matrix representation in numerical calculations, but in quantum simulations, we can use the following equivalent form $\hat{H}_r = \sum_{j=1}^{L-1} \left(|0\rangle\langle j|_{a_r} + |j\rangle\langle 0|_{a_r}\right) \otimes H_{j,j+1}$, which satisfies Eq. (6.3) relating $\hat{H}$ and its "square-root" $\hat{H}_r$. Therefore, the minimal number of ancilla qubits to construct $\hat{H}_r$ is $\lceil \log_2 L \rceil$.

Another reason we consider the isotropic case is that for $q = 1$ the $(L+1)$-fold degenerate ground states are the $L+1$ Dicke states [165] $\left|D_j^L\right\rangle = \sqrt{j!(L-j)!/L!} \sum_{|x|=j} |x\rangle$, where

$0 \leq j \leq L$, $x \in \{0,1\}^L$ is a bit string, and $|x|$ is the Hamming weight defined as the number of ones in x. The sum $\sum_{|x|=j}$ includes all bit strings with the same Hamming weight j. Dicke states have applications in areas such as quantum metrology and quantum computing, and various probabilistic and deterministic methods have been proposed to prepare Dicke states in quantum systems [165, 166] or on quantum computers [167, 168]. Since LCU is a core routine in our algorithm, our projective state preparation method is probabilistic. To prepare a Dicke state $\left|D_j^L\right\rangle$ with Hamming weight j, we choose a simple initial state $|x_0\rangle = |1\cdots10\cdots0\rangle$ with the Hamming weight $|x_0| = j$. For such an initial state, we will consider preparing the state $\left|D_j^L\right\rangle$ with $j = L/2$ below. This is the most challenging case since the overlap between the initial state and the true ground state is smaller than any other different j.

In Fig. 6.3, we compare the query complexity of three different projective ground-state preparation algorithms: (i) our algorithm using $e^{-\frac{1}{2}t^2\hat{H}^2}$ operator, (ii) algorithm of Ge *et al.* [83] using $\cos^M(\hat{H})$ operator, (iii) our algorithm with spectral gap amplification using $e^{-\frac{1}{2}t^2\hat{H}_r^2}$. The results from LCU implementation of these operators given by Thm. 2 are plotted alongside the results from the exact implementation using sparse matrix representation. We quantify the query complexity with the parameter t_H defined as the longest effective time evolved by the Hamiltonian time-evolution oracle. For our algorithm (i) and (iii), $t_H = tz_c = t\sqrt{2\log\frac{2}{\gamma\eta}}$, where t is varied from 0 to the the lower bound $\frac{1}{\Delta}\sqrt{2\log\frac{1}{\gamma\eta}}$ given by Thm. 2, which is the lower bound required to ensure the fidelity error within $\epsilon = \eta^2/2$ (we used $\epsilon = 0.01$). In (i) we used $\Delta = \Delta_s$, which is the true spectral gap of $\hat{H}$, and in (iii) we used $\Delta = \sqrt{\Delta_s}$, which is the spectral gap of $\hat{H}_r$. For algorithm (ii) of Ge *et al.*, $t_H = 2 \times \min\left\{\left\lceil\sqrt{\frac{M}{2}\log\frac{2}{\gamma\eta}}\right\rceil, \frac{M}{2}\right\}$, where the even integer M is varied from 0 to the lower bound $2\left\lceil\frac{1}{\Delta^2}\log\frac{1}{\gamma\eta}\right\rceil$ that is required to ensure the fidelity error within ϵ. Note that we used the tightened bounds derived in App. D.5 in the algorithm (ii) of Ge *et al.*; taking the integer value in the t_H definition causes the zig-zag appearance in some of results from algorithm (ii) of Ge *et al.*, for example, Fig. 6.3(a), the blue line and the blue dots.

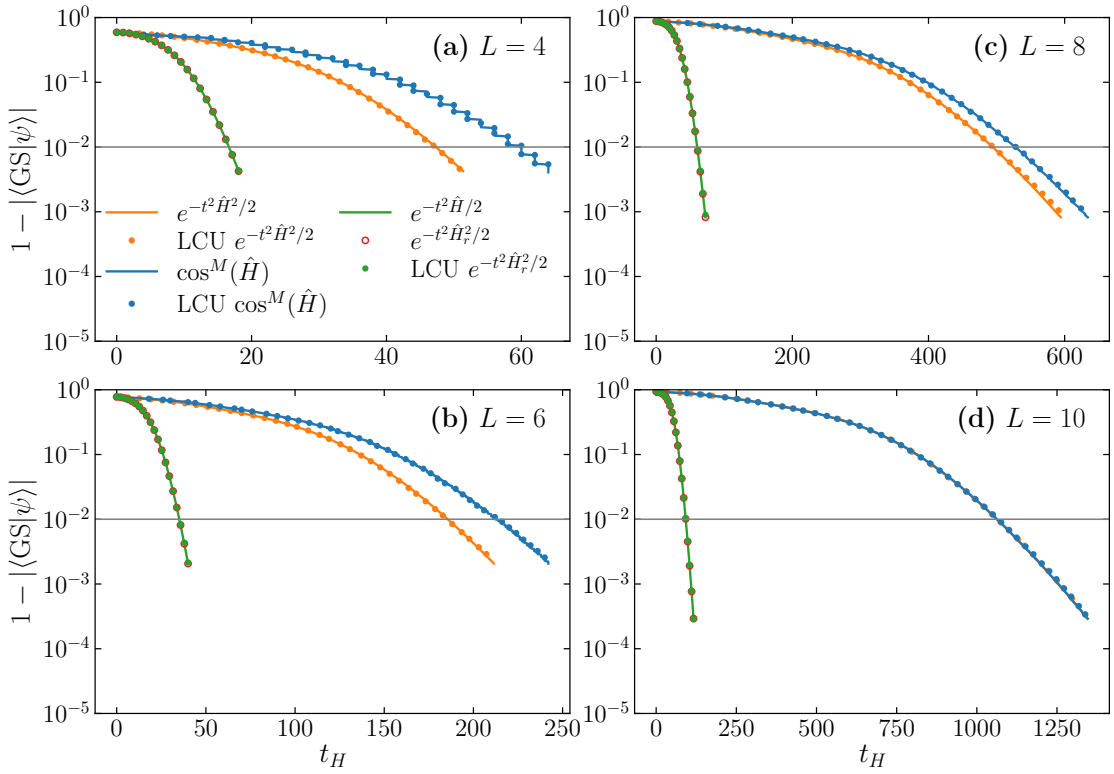

Figure 6.3: Projective ground-state preparation for isotropic ferromagnetic Heisenberg chain with (a) $L = 4$, (b) $L = 6$, (c) $L = 8$, and (d) $L = 10$ sites. The true ground state is the Dicke state $\left|D^L_{L/2}\right\rangle$ and the initial state used is $|x_0\rangle = |1\ldots10\ldots0\rangle$ with Hamming weight $|x_0| = L/2$. Each panel compares the query complexity of three different projective ground-state preparation algorithms: (i) $e^{-\frac{1}{2}t^2\hat{H}^2}$ operator, (ii) $\cos^M(\hat{H})$ operator, (iii) $e^{-\frac{1}{2}t^2\hat{H}_r^2}$ operator with spectral gap amplified Hamiltonian $\hat{H}_r$. The Hamiltonian is renormalized and its spectrum lies between 0 and 1. The results from LCU (dots) implementation using Thm. 2 are plotted alongside the results from the exact implementation using sparse matrix representation (red circles for $e^{-\frac{1}{2}t^2\hat{H}_r^2}$ and solid lines for others). t_H quantifies the query complexity to Hamiltonian time-evolution oracle and is defined as the longest effective time evolved by the oracle. The full definition of t_H is given in the main text. The gray horizontal line marks the targeted fidelity error $\epsilon = 0.01$ for which we set various parameters given in Thm. 2.

From Fig. 6.3, we see algorithm (iii), our method combined with the spectral gap amplification, gives the best scaling. For larger system size with decreasing normalized spectral gap, the query complexity reduction can be quite significant. As a side note, our algorithm (i) and the algorithm (ii) of Ge *et al.* show similar scalings and the difference becomes smaller as the system size grows.

6.3.2 Application to the Hubbard model

In this chapter, we apply our algorithms to prepare the ground state and compute the single-particle Green's function of the one-dimensional Hubbard model (Sec. 2.3) with L lattice sites and the periodic boundary condition. We will compare the results for $L \in \{2, 3, 4, 5\}$ for which the number of fermion modes is $2L$ (factor of 2 from two spin species) and the dimensions of the Hilbert space are 2^{2L}. We also choose the chemical potential so that the average particle number density $n = \frac{1}{L}\sum_{i\sigma}\langle \hat{n}_{i\sigma}\rangle = 1$, i.e., the system is at half-filling. We have written the Hamiltonian Eq. (2.14) in a particle-hole symmetric form, as indicated by the subtraction of $\frac{1}{2}$ in the interaction term proportional to U. For this form, the chemical potential $\mu = 0$ at half-filling. We consider a strong correlation case with an electron repulsion strength of $U/\tilde{t} = 8$.

Ground-state preparation

The choice of initial trial state is crucial to the success of projective state preparation procedure. For the strong interaction U we choose, a single-component antiferromagnetic product state is a good initial trial state. This corresponds to the fermionic state $|\uparrow_0, \downarrow_1, \cdots, \uparrow_L, \downarrow_{L-1}\rangle$ for even L (the state $|\uparrow_0, \downarrow_1, \cdots, \uparrow_{L-1}\rangle$ for odd L), where each lattice site is singly-occupied by either up- or down-spin electrons in a staggered pattern. At $U/\tilde{t} = 8$ the interaction strength imposes the large penalty for doubly occupied configurations which our input state avoids.

In Fig. 6.4, we compare the query complexity of two different projective ground-state preparation algorithms: (i) our algorithm using $e^{-\frac{1}{2}t^2\hat{H}^2}$ operator, and (ii) algorithm of Ge

et al. [83] using $\cos^M(\hat{H})$ operator and the tightened bounds derived in App. D.5. For each algorithm, the parameter t_H quantifying the query complexity is defined above in Sec. 6.3.1. Similar to the XXZ chain, we find our algorithm performs slightly better than the algorithm of Ge *et al.* [83] in smaller system sizes. By the panel of Fig. 6.4(d) both algorithms show almost identical scalings, which agrees with the asymptotic query complexity given in Tab. 6.1 for these two algorithms.

In Fig. 6.5, we plot the difference $|E - E_{\mathrm{GS}}|$ between the approximate ground energy E using the prepared ground state and the true ground energy E_{GS}. Note that the Hamiltonian is renormalized and its spectrum lies between 0 and 1, so the true ground energy E_{GS} is set to exactly zero (within machine precision in our numerical simulation and, for quantum simulation, within the required precision given in Tab. 6.1). We notice that the additive error $|E - E_{\mathrm{GS}}|$ for the ground energy in Fig. 6.5 computed via both our algorithm and the algorithm of Ge *et al.*, approaches the chosen $\epsilon = 0.01$ more quickly than the error in the fidelity does in Fig. 6.4. This is likely due to the fact that our choice of trial initial state is an excellent trial state with respect to energy for the strong interaction U we chose.

Single-particle Green's function calculation

In the Hubbard model, the single particle Green's function in the frequency domain can be rewritten from Eq. (6.5) as

$$G^R_{jj'}(\omega) = \sum_\alpha \frac{(M^\alpha_{j'})^* M^\alpha_j}{\omega + \mu - E^{N+1}_\alpha + E^N_0 + i\delta} \tag{6.14}$$

$$+ \sum_\beta \frac{(L^\beta_j)^* L^\beta_{j'}}{\omega + \mu + E^{N-1}_\beta - E^N_0 + i\delta}, \tag{6.15}$$

where $E^{N\pm1}_\alpha$ is the eigenenergy of the $\psi^{N\pm1}_\alpha$ eigenstate of the $N \pm 1$ particle sector, μ is the chemical potential which we set to 0, E^N_0 is the ground state energy of the N particle sector, and δ is a convergence factor from the Fourier integral transform of the time domain Green's

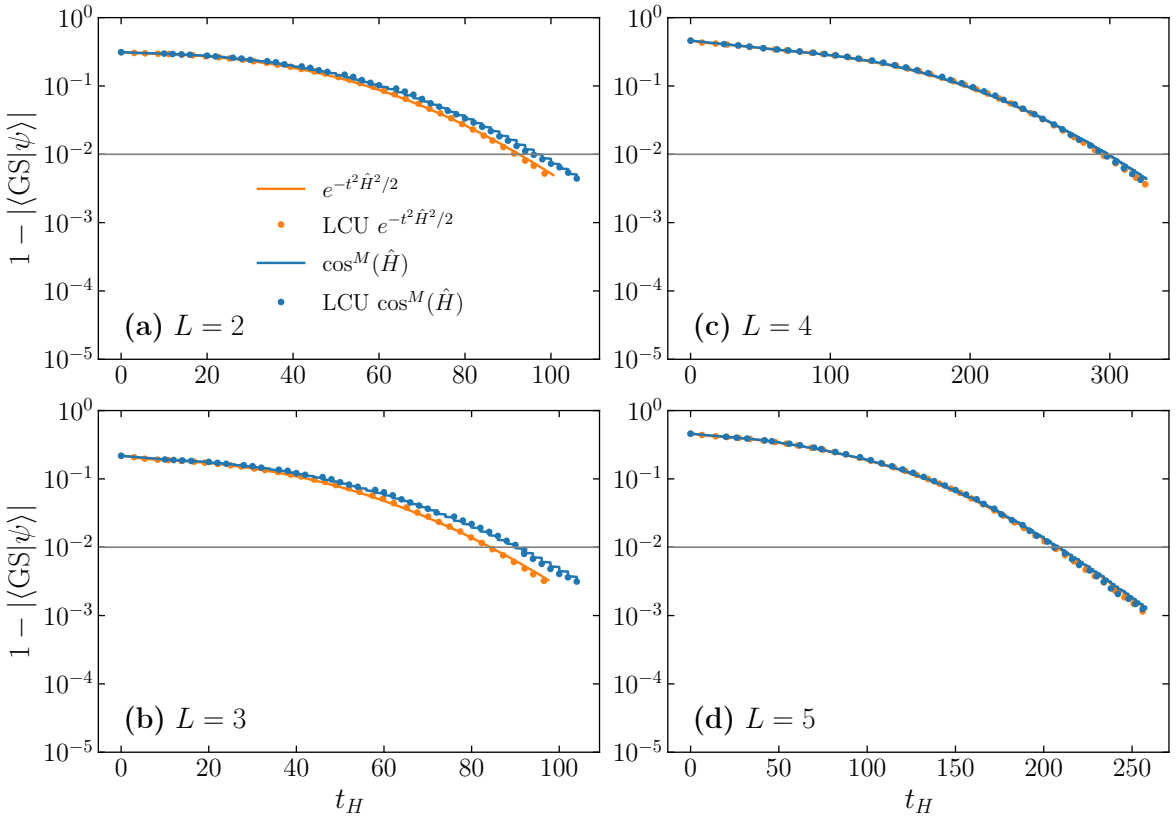

Figure 6.4: Projective ground-state preparation for Hubbard model Eq. (2.14) with (a) $L = 2$, (b) $L = 3$, (c) $L = 4$, and (d) $L = 5$ sites. The parameters $\tilde{t} = 1$, $U = 8$, and at half-filling $\mu = 0$. Each panel compares the query complexity of two different projective ground-state preparation algorithms: (i) $e^{-\frac{1}{2}t^2\hat{H}^2}$ operator and (ii) $\cos^M(\hat{H})$ operator. The Hamiltonian has been renormalized and its spectrum lies between 0 and 1. The results from LCU (dots) implementation using Thm. 2 are plotted alongside the results from the exact implementation using sparse matrix representation (solid lines). t_H is defined in the same way as in Fig. 6.3. The gray horizontal line marks the targeted fidelity error $\epsilon = 0.01$ for which we set various parameters given in Thm. 2.

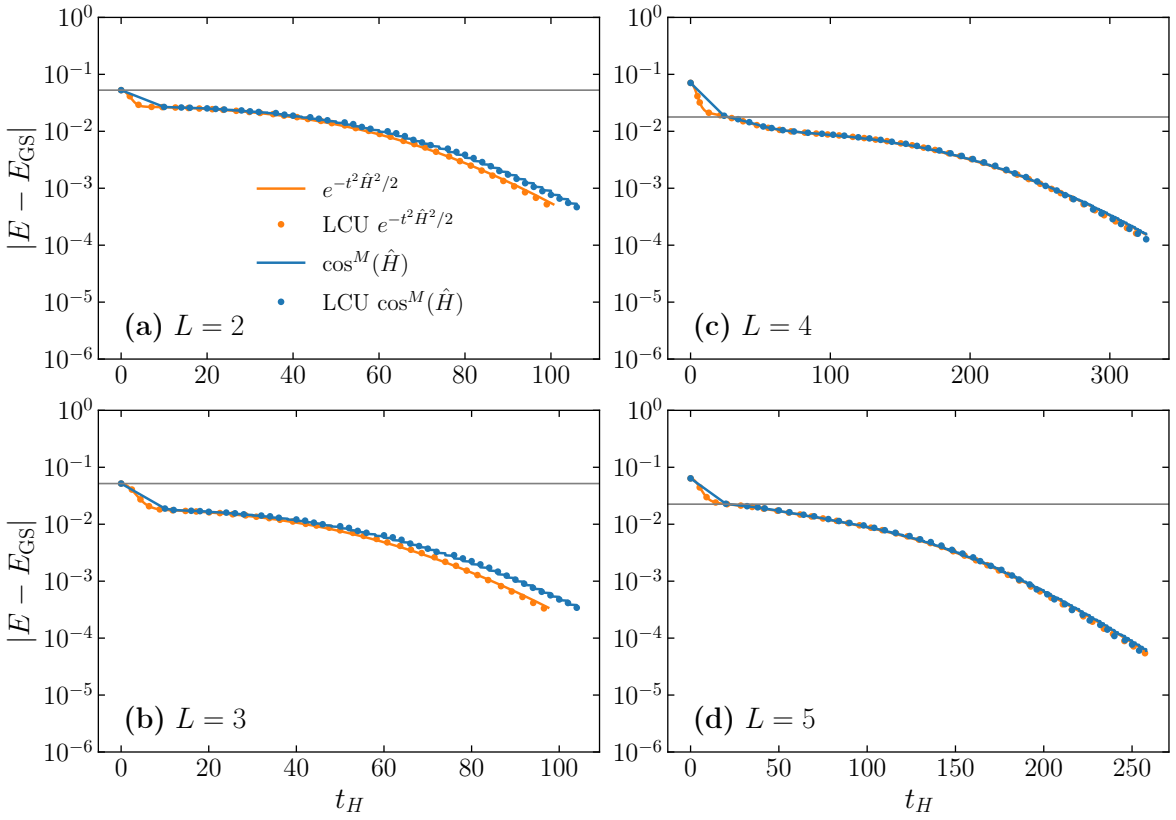

Figure 6.5: Additive error of the ground state energy of the Hubbard model Eq. (2.14) with (a) $L = 2$, (b) $L = 3$, (c) $L = 4$, and (d) $L = 5$ sites. The ground state used in calculating the energy expectation values are those shown in Fig. 6.4. Each panel compares the query complexity of two different projective ground-state preparation algorithms: (i) $e^{-\frac{1}{2}t^2\hat{H}^2}$ operator and (ii) $\cos^M(\hat{H})$ operator. The horizontal gray line denotes the value of the true spectral gap Δ_s.

function. The weights of the poles in the Green's function are given by

$$M_j^\alpha = \langle \psi_\alpha^{N+1} | \hat{c}_j^\dagger | \psi_0^N \rangle = \langle \psi_0^N | \hat{c}_j | \psi_\alpha^{N+1} \rangle^* , \tag{6.16}$$

$$L_j^\beta = \langle \psi_\beta^{N-1} | \hat{c}_j | \psi_0^N \rangle = \langle \psi_0^N | \hat{c}_j^\dagger | \psi_\beta^{N-1} \rangle^* . \tag{6.17}$$

In our numerical simulations, we utilize Eq. (6.14) to compute the Green's function and local density of states. However, on the quantum computer the Green's function will be calculated with equation Eq. (6.11a) (probabilistically) or Eq. (6.11b) (deterministically). This discrepancy is due to convenience for the classical numerical simulations and the fact that, for our numerical simulations, it suffices to show that the resolvent operator can be constructed via the discretized FIT given in Eq. (6.8). To show this, we calculate the resolvent via Eq. (6.8) and use it to compute the local Green's function of the first lattice site, i.e. $G_{00}^R(\omega)$, using Eq. (6.14). In Fig. 6.6, we plot the local density of states for Hubbard chains of size 2–5 corresponding to panels (a)–(d). We see that for a conservative allowable error of $\epsilon' = 0.05$ and broadening 0.1, we are able to reproduce the relevant peaks and their relative weights in the local density of states. For the degeneracy in the ground state for the 3 and 5-site cases, we trace over the degenerate ground states, and we renormalize the local density of states for all cases. Our choice of strong electron interactions ($U/\tilde{t} = 8$) allows us to clearly see the gap in the local density of states characteristic of a Mott insulating phase.

6.4 Conclusion

We have presented quantum algorithms for ground state preparation and response function calculation. Our projective method for preparing the ground state of a system based on the Hubbard-Stratonovich transformation of an imaginary time like operator. Our state preparation algorithm matches the optimal scaling in the spectral gap Δ and initial overlap γ between trial and ground states [85]. However, our algorithm quadratically reduced the precision to which a ground state estimate must be known (compared to that reported in

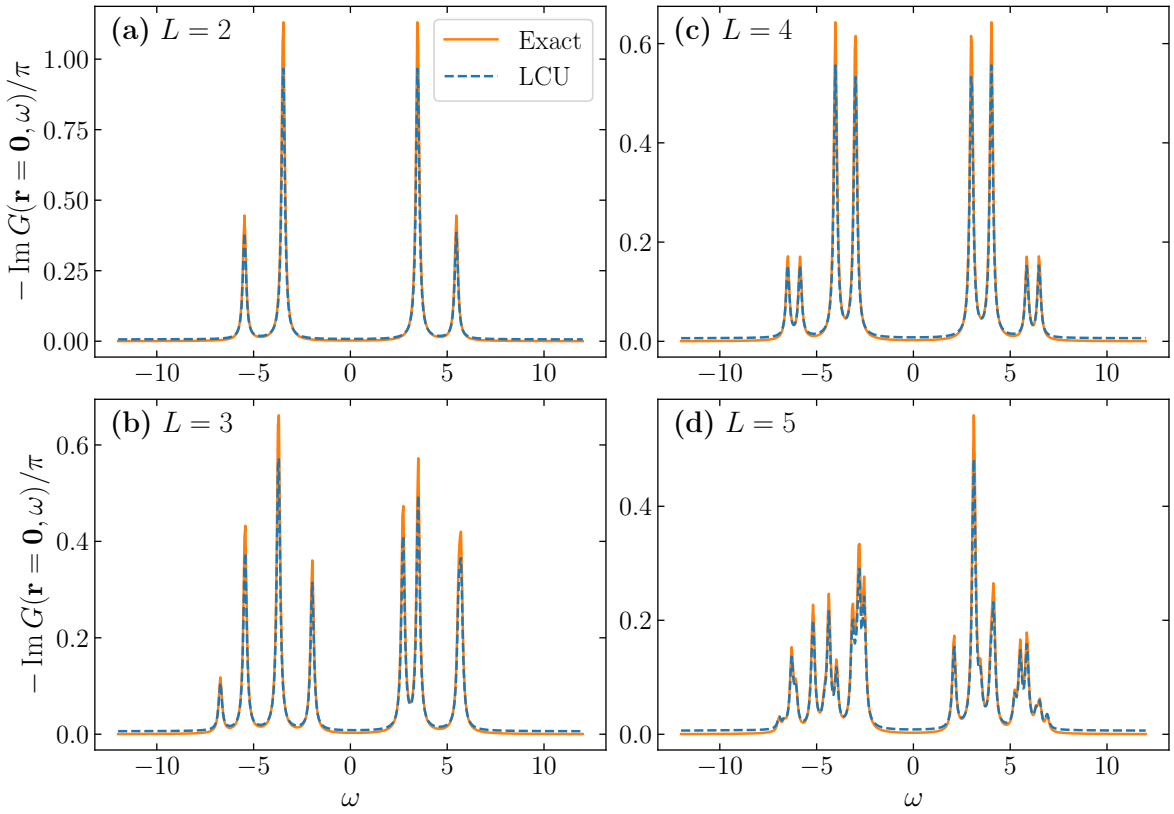

Figure 6.6: Calculations of the local density of states for the first lattice site of the two, three, four, and five site Hubbard model with parameters $t = 1$ and $U = 8$ at half-filling. Here, we have constructed the resolvent operator both exactly (orange) and via LCU (blue), traced over the degenerate ground states of the 3 and 5-site models, and renormalized each to 1. LCU refers to the linear combination of unitaries approximant to the Laplace transform construction of the resolvent operator given in Eq. (6.8).

Ref. 83), but matches the scaling of Ref. 83 when their bounds are tightened as shown in App. D.5.

Our algorithm for computing the response function of a system via construction of the resolvent through the discretized Fourier-Laplace transform using LCU shows good agreement with the exact value and tractable scaling. Our algorithm is the first proposed to directly construct the general response function of a system on a quantum computer. It does not rely on variational principles or statistical sampling, but instead directly constructs the resolvent operator integral transformations and LCU.

To verify our algorithms and determine the algorithm's complexity in practice we have performed numerical simulations for both ground state preparation and computation of the Green's function in the context of the paradigmatic Fermi-Hubbard model in one dimension with different numbers of sites. We have also performed numerical simulations for ground state preparation of the q-deformed XXZ model, since the Fermi-Hubbard model does not satisfy the frustration free requirement of spectral gap amplification. We find that our method for ground state preparation and that of Ref. 83 rapidly asymptotically converge even for relatively small system sizes.

Chapter 7

Conclusions

In the field of condensed matter physics, and specifically when considering systems of strongly correlated electrons, there is no efficient simulation method to describe these systems in all cases. For some systems where there is no fermionic sign problem (Sec. 1.2.1), Monte-Carlo methods can describe systems of hundreds of orbitals and is considered a "state of the art" technique. In systems where the fermionic sign problem dominates, exact diagonalization, coupled cluster, or density matrix renormalization group methods (Sec. 1.2.2) can still be used, and quantum Monte-Carlo methods can still be used for certain temperatures. However, these methods suffer from exponential scalings of their own in certain systems, making them intractable for simulation on classical computers.

In this thesis, I have shown multiple ways in which the power of quantum computing can be leveraged to simulate physical systems. Specifically, I have focused on simulations of strongly-correlated electron systems that have exponential classical computation costs for certain parameter regimes. As a simulation end result, I have focused on the calculation of various Green's functions and correlation functions of systems. The reason for this focus is two-fold: Green's functions contain the most physically relevant information about the system without needing to reconstruct the entire many body state, and because Green's functions are expressed as expectation values they can be efficiently calculated on quantum computers. To recover the entire quantum many-body state of the system requires

exponentially many quantum resources, which defeats the purpose of using a quantum computer. To simulate many-body systems by computing their Green's functions, I have focused not only on what currently available quantum hardware can efficiently simulate, but also on algorithmic developments that can be applied to the next generation of quantum hardware.

In Ch. 4, I show a simulation of a two-site Anderson impurity model within the framework of dynamical mean-field theory (DMFT). This simulation includes both quantum computation of the Green's function, as well as a classical feedback loop for the DMFT procedure. This project was carried out by utilizing quantum computing resources at IBM. We found that even for our small problem the noise in the quantum computer was a significant hurdle and required the development of different techniques than those previously proposed to simulate the system. To address the problem of ground state preparation, we created an ansatz circuit suited to the device we were using and solved entirely classically for parameters that, when fed into that ansatz, would prepare the ground state (assuming perfect gate execution). We considered doing this part classically justifiable since the main focus of this work was to run the DMFT loop (see Fig. 4.1) and we had used a hardware efficient ansatz. However, in the future I chose to turn in the direction of how to prepare ground states on a quantum computer because it is an integral part of many quantum simulation algorithms and in future simulations it will not be feasible to find the ground state of the system classically.

Turning to the problem of quantum state preparation, which was mostly ignored in Ch. 4, in Ch. 5 I present a method that uses classically computed coupled cluster quantities (Sec. 2.5) to compute the Green's function, but with the most intractable part of the problem being offloaded to the quantum computer (Fig. 5.1). In doing so, we are able to obtain a polynomial speedup over coupled cluster simulations that use purely classical computing. By computing the coupled cluster amplitudes on the classical computer and then computing the Green's function on the quantum computer, our method is efficient at every step. Note that this is not a quantum variational state preparation (Sec. 3.1.1), but a different kind of hybrid quantum classical procedure to approximate the ground state of the system and calculate the Green's function using coupled cluster methods. This work provided a hybrid

quantum-classical method with quantum speedup for calculating the Green's function of the system in the time domain by approximating the ground state of the system. However, it would suffer in many of the same parameter regimes as regular coupled cluster theory, and does not allow for computation of the Green's function directly in the frequency domain which is desirable for many applications.

To address the shortcomings of the method presented in previous chapters, in Ch. 6 I introduce a unified framework for state preparation and Green's function calculation. This unified framework is based on discretized and truncated integral transformations of non-unitary operators. Specifically, we consider the non-unitary ground state projection operator $e^{-t^2H^2/2}$ and the non-unitary resolvent operator $R(\omega, \Gamma) = (\omega + i\Gamma - H)^{-1}$ used for real frequency domain Green's function calculation. There have been other proposed methods for ground state preparation by projection operator such as those presented in Sec. 3.1.2, as well as proposed methods for Green's function calculation (Sec. 3.4). However, the method presented in Ch. 6 has the advantage of an easy to follow, unified workflow for both calculations.

Although my research projects through time became more abstract and more focused on algorithmic development as opposed to running simulations on real quantum devices, I always tried to keep practicality and ease of application in mind during the algorithmic development. The progression from running small, hybrid quantum-classical simulations to developing fault-tolerant algorithms is mainly due to the noise in the quantum device and the general difficulty of running even a very small simulation on real quantum hardware. However, it is worth noting that the data shown in Ch. 4 was collected in late 2019, and since then quantum devices have greatly improved in terms of the amount of noise causing errors in the device and the number of available qubits. In fact, just two years after the work presented in Ch. 4, I was involved in another project for simulating two-site dynamical mean-field theory on IBM quantum hardware in late 2021 [120]. In this case, we utilized recent advances in simulating time evolution along with other advancements specific to the two-site problem (see the discussion at the end of Ch. 4). The improvements in quantum devices and these new techniques allowed us to map the full phase diagram of the two-site dynamical

mean-field theory, i.e. a two-site Anderson impurity model iterated to self-consistency, from the Mott-metal regime through the phase transition and into the Mott-insulating regime. This new and improved implementation shows the rate at which these devices are improving and the simulation power they will soon have. In addition to improved error rates and noise, the number of qubits available for use in these devices is growing extremely quickly [14]. Soon, this increase in the number of qubits will make quantum error-correction feasible and thus vastly improve the simulations.

Future work could include improved quantum-classical hybrid methods, which should be a top priority for achieving quantum advantage in the simulation of physical systems. Although there are many simulation methods proposed that utilize the quantum-classical variational quantum eigensolver (VQE), there are many other avenues to explore. The most straightforward avenue to develop hybrid quantum-classical algorithms is to explore how and when current classical simulation algorithms fail, and attempt to find a way to offload the problematic aspects to the quantum computer. Specifically, different variations of quantum Monte Carlo (QMC), such as auxiliary field QMC are being investigated [169, 170] but could be investigated further. For techniques that require an exponential amount of memory have a more straightforward relief on quantum computers. A less direct, but still important, avenue for furthering simulations that leverage quantum computers is the application of existing and development of new algorithms that are designed for quantum computers as opposed to adapting classical algorithms to quantum computers. This method is much more difficult in practice, but is where the full power of quantum computing will be utilized. This includes methods that, for example, utilize the Grover search algorithm which uses a quantum computer to search an unstructured set of elements using just $\mathcal{O}(\sqrt{N})$ function evaluations instead of the $\mathcal{O}(N)$ function evaluations a classical computer would require. Another direction for future research would be to investigate how the worst-case asymptotic scalings of many proposed algorithms compare to an average case for physically relevant systems, such as those with restricted locality. The research presented in this thesis highlights the need for development of quantum-classical hybrid simulation techniques for the NISQ

era along with fault-tolerant regime algorithmic developments and the importance of actual implementation of proposed algorithms to discover their viability on real quantum devices.

Bibliography

Bibliography

[1] P. W. Shor, in *Proceedings 35th Annual Symposium on Foundations of Computer Science* (1994), pp. 124–134, ISSN null. 1

[2] R. P. Feynman, International Journal of Theoretical Physics **21**, 467 (1982), ISSN 00207748. 1

[3] S. Lloyd, Science **273**, 1073 (1996), ISSN 0036-8075. 1, 2, 8

[4] J. Preskill, Quantum **2**, 79 (2018), ISSN 2521-327X, URL https://doi.org/10.22331/q-2018-08-06-79. 2

[5] D. S. Abrams and S. Lloyd, Phys. Rev. Lett **79**, 2586–2589 (1997), ISSN 1079-7114, URL http://dx.doi.org/10.1103/PhysRevLett.79.2586. 2, 7

[6] A. Liebsch and H. Ishida, Journal of Physics: Condensed Matter **24**, 053201 (2011), URL https://doi.org/10.1088%2F0953-8984%2F24%2F5%2F053201. 2, 7, 26

[7] A. Y. Kitaev, A. H. Shen, and M. N. Vyalyi, *Classical and Quantum Computation* (American Mathematical Society, USA, 2002), ISBN 0821832298. 2

[8] C. P. Williams, *Explorations in Quantum Computing*, Texts in Computer Science (Springer-Verlag London Limited, London, 2011), ISBN 9781846288876. 2, 42

[9] F. Arute, K. Arya, R. Babbush, D. Bacon, J. Bardin, R. Barends, R. Biswas, S. Boixo, F. Brandao, D. Buell, et al., Nature **574**, 505–510 (2019), URL https://www.nature.com/articles/s41586-019-1666-5. 3, 8

[10] M. A. Nielsen and I. L. Chuang, *Quantum Computation and Quantum Information: 10th Anniversary Edition* (Cambridge University Press, New York, NY, USA, 2011), 10th ed., ISBN 1107002176, 9781107002173. 3, 8, 10, 11, 12, 13, 59, 84, 135, 137

[11] A. Kandala, A. Mezzacapo, K. Temme, M. Takita, M. Brink, J. M. Chow, and J. M. Gambetta, Nature **549**, 242 (2017), ISSN 14764687, URL http://dx.doi.org/10.1038/nature23879. 3, 56, 140, 141

[12] S. Endo, S. C. Benjamin, and Y. Li, Phys. Rev. X **8**, 031027 (2018), URL https://link.aps.org/doi/10.1103/PhysRevX.8.031027. 3, 56

[13] S. Endo, Q. Zhao, Y. Li, S. Benjamin, and X. Yuan, Phys. Rev. A **99**, 012334 (2019), URL https://link.aps.org/doi/10.1103/PhysRevA.99.012334. 3, 56

[14] P. Ball, Nature **599**, 542–542 (2021), URL https://www.nature.com/articles/d41586-021-03476-5. 3, 8, 115

[15] B. Bauer, D. Wecker, A. J. Millis, M. B. Hastings, and M. Troyer, Physical Review X **6**, 1 (2016), ISSN 21603308. 3, 23, 50, 51, 53, 135

[16] S. Endo, I. Kurata, and Y. O. Nakagawa (2019), 1909.12250, URL http://arxiv.org/abs/1909.12250.

[17] I. D. Kivlichan, J. McClean, N. Wiebe, C. Gidney, A. Aspuru-Guzik, G. K.-L. Chan, and R. Babbush, Phys. Rev. Lett. **120**, 110501 (2018), URL https://link.aps.org/doi/10.1103/PhysRevLett.120.110501.

[18] D. Wecker, M. B. Hastings, N. Wiebe, B. K. Clark, C. Nayak, and M. Troyer, Phys. Rev. A **92**, 062318 (2015), URL https://link.aps.org/doi/10.1103/PhysRevA.92.062318. 3, 31, 43, 50

[19] E. Gull, A. J. Millis, A. I. Lichtenstein, A. N. Rubtsov, M. Troyer, and P. Werner, Rev. Mod. Phys. **83**, 349 (2011), URL https://link.aps.org/doi/10.1103/RevModPhys.83.349. 4, 5

[20] M. Troyer and U.-J. Wiese, Phys. Rev. Lett. **94**, 170201 (2005), URL https://link.aps.org/doi/10.1103/PhysRevLett.94.170201. 5

[21] S. Sakai, R. Arita, and H. Aoki, Phys. Rev. B **70**, 172504 (2004), URL https://link.aps.org/doi/10.1103/PhysRevB.70.172504. 5

[22] S. Johnston, E. A. Nowadnick, Y. F. Kung, B. Moritz, R. T. Scalettar, and T. P. Devereaux, Phys. Rev. B **87**, 235133 (2013), URL https://link.aps.org/doi/10.1103/PhysRevB.87.235133. 5, 6

[23] V. I. Iglovikov, E. Khatami, and R. T. Scalettar, Physical Review B - Condensed Matter and Materials Physics **92** (2015), ISSN 1550235X. 5

[24] S. Wiesner (1996), 9603028. 7

[25] R. J. Bartlett and M. Musiał, Rev. Mod. Phys. **79**, 291 (2007), URL https://link.aps.org/doi/10.1103/RevModPhys.79.291. 7

[26] *Report of the Basic Energy Sciences Roundtable Opportunities for Quantum Computing in Chemical and Materials Sciences: October 31-November 1, 2017, Gaithersburg, Maryland* (U.S. Department of Energy, 2018). 7

[27] S. R. White, Phys. Rev. Lett. **69**, 2863 (1992), URL https://link.aps.org/doi/10.1103/PhysRevLett.69.2863. 7

[28] F. A. Wolf, I. P. McCulloch, and U. Schollwöck, Physical Review B **90** (2014), ISSN 1550-235X. 7

[29] U. Schollwöck, Annals of Physics **326**, 96–192 (2011), ISSN 0003-4916, URL http://dx.doi.org/10.1016/j.aop.2010.09.012. 7

[30] D. P. DiVincenzo, Fortschritte der Physik **48**, 771 (2000). 8

[31] Glosser.ca, *Bloch sphere* (2012), URL https://commons.wikimedia.org/wiki/File:Bloch_Sphere.svg. 9

[32] P. Krantz, M. Kjaergaard, F. Yan, T. P. Orlando, S. Gustavsson, and W. D. Oliver, Applied Physics Reviews **6**, 021318 (2019), https://doi.org/10.1063/1.5089550, URL https://doi.org/10.1063/1.5089550. 10

[33] K. Wright, K. M. Beck, S. Debnath, J. M. Amini, Y. Nam, N. Grzesiak, J. S. Chen, N. C. Pisenti, M. Chmielewski, C. Collins, et al., Nature Communications **10**, 5464 (2019), URL https://doi.org/10.1038/s41467-019-13534-2. 10

[34] M. Q. Team, *Developing a topological qubit* (2020), URL https://cloudblogs.microsoft.com/quantum/2018/09/06/developing-a-topological-qubit/. 11

[35] G. P. Collins, Scientific American **294**, 56 (2006), ISSN 00368733, 19467087, URL http://www.jstor.org/stable/26061414.

[36] J. Preskill, *Topological Quantum Computation*, http://www.theory.caltech.edu/~preskill/ph219/topological.pdf (2004), [Online; accessed 7-February-2022]. 11

[37] G. Mahan, *Many-Particle Physics*, Physics of Solids and Liquids (Springer US, 1990), ISBN 9780306434235, URL https://books.google.com/books?id=v8du6cp0vUAC. 16, 17, 18, 20, 22

[38] T. Matsubara, Progress of Theoretical Physics **14**, 351 (1955), ISSN 0033-068X, https://academic.oup.com/ptp/article-pdf/14/4/351/5286981/14-4-351.pdf, URL https://doi.org/10.1143/PTP.14.351. 16

[39] J. Hubbard and B. H. Flowers, Proceedings of the Royal Society of London. Series A. Mathematical and Physical Sciences **276**, 238 (1963), https://royalsocietypublishing.org/doi/pdf/10.1098/rspa.1963.0204, URL https://royalsocietypublishing.org/doi/abs/10.1098/rspa.1963.0204. 20

[40] N. F. MOTT, Rev. Mod. Phys. **40**, 677 (1968), URL https://link.aps.org/doi/10.1103/RevModPhys.40.677. 20

[41] M. Imada, A. Fujimori, and Y. Tokura, Rev. Mod. Phys. **70**, 1039 (1998), URL https://link.aps.org/doi/10.1103/RevModPhys.70.1039.

[42] A. Georges and G. Kotliar, Phys. Rev. B **45**, 6479 (1992), URL https://link.aps.org/doi/10.1103/PhysRevB.45.6479. 20, 71

[43] S. R. White, D. J. Scalapino, R. L. Sugar, E. Y. Loh, J. E. Gubernatis, and R. T. Scalettar, Phys. Rev. B **40**, 506 (1989), URL https://link.aps.org/doi/10.1103/PhysRevB.40.506. 20

[44] B.-X. Zheng, C.-M. Chung, P. Corboz, G. Ehlers, M.-P. Qin, R. M. Noack, H. Shi, S. R. White, S. Zhang, and G. K.-L. Chan, Science **358**, 1155 (2017), ISSN 0036-8075, https://science.sciencemag.org/content/358/6367/1155.full.pdf, URL https://science.sciencemag.org/content/358/6367/1155. 20

[45] E. W. Huang, C. B. Mendl, H.-C. Jiang, B. Moritz, and T. P. Devereaux, npj Quantum Materials **3**, 22 (2018), URL https://doi.org/10.1038/s41535-018-0097-0. 20

[46] E. H. Lieb and F. Y. Wu, Phys. Rev. Lett. **20**, 1445 (1968), URL https://link.aps.org/doi/10.1103/PhysRevLett.20.1445. 20

[47] E. W. Huang, R. Sheppard, B. Moritz, and T. P. Devereaux, Science **366**, 987 (2019), ISSN 0036-8075, https://science.sciencemag.org/content/366/6468/987.full.pdf, URL https://science.sciencemag.org/content/366/6468/987. 20

[48] E. Gull, O. Parcollet, and A. J. Millis, Phys. Rev. Lett. **110**, 216405 (2013), URL https://link.aps.org/doi/10.1103/PhysRevLett.110.216405. 20

[49] X. Chen, J. P. F. LeBlanc, and E. Gull, Phys. Rev. Lett. **115**, 116402 (2015), URL https://link.aps.org/doi/10.1103/PhysRevLett.115.116402. 20

[50] T. A. Maier, M. Jarrell, T. C. Schulthess, P. R. C. Kent, and J. B. White, Phys. Rev. Lett. **95**, 237001 (2005), URL https://link.aps.org/doi/10.1103/PhysRevLett.95.237001. 20

[51] J. R. Schrieffer and P. A. Wolff, Phys. Rev. **149**, 491 (1966), URL https://link.aps.org/doi/10.1103/PhysRev.149.491. 22

[52] A. Hewson, *The Kondo Problem to Heavy Fermions. Cambridge Studies in Magnetism, Vol. 2.* (Cambridge University Press, Cambridge, 1993). 22

[53] A. Georges, G. Kotliar, W. Krauth, and M. J. Rozenberg, Reviews of Modern Physics **68**, 13 (1996), ISSN 1526498X. 22, 23

[54] S. Yamada, T. Imamura, and M. Machida, in *Supercomputing Frontiers*, edited by R. Yokota and W. Wu (Springer International Publishing, Cham, 2018), pp. 243–256, ISBN 978-3-319-69953-0. 21

[55] C. Lanczos, Journal of Research of the National Bureau of Standards **45**, 255 (1950), URL https://nvlpubs.nist.gov/nistpubs/jres/045/jresv45n4p255_A1b.pdf. 26

[56] E. Pavarini, E. Koch, A. Lichtenstein, and D. Vollhardt, eds., *The LDA+DMFT approach to strongly correlated materials*, vol. 1 of *Schriften des Forschungszentrums Jülich. Reihe modeling and simulation* (Forschungszenrum Jülich GmbH Zentralbibliothek, Verlag, Jülich, 2011), record converted from VDB: 12.11.2012, URL https://juser.fz-juelich.de/record/17645. 26

[57] G. H. Golub and C. F. van Loan, *Matrix computations* (Johns Hopkins University Press, 2013), 4th ed. 26

[58] M. Nooijen and J. G. Snijders, Int. J. Quantum Chem. **44**, 55 (1992), ISSN 1097-461X, URL http://dx.doi.org/10.1002/qua.560440808. 26, 75

[59] M. Nooijen and J. G. Snijders, Int. J. Quantum Chem. **48**, 15 (1993), ISSN 1097-461X, URL http://dx.doi.org/10.1002/qua.560480103.

[60] M. Nooijen and J. G. Snijders, J. Chem. Phys. **102**, 1681 (1995), URL http://scitation.aip.org/content/aip/journal/jcp/102/4/10.1063/1.468900. 26, 75

[61] T. Zhu, C. A. Jiménez-Hoyos, J. McClain, T. C. Berkelbach, and G. K.-L. Chan, Phys. Rev. B **100**, 115154 (2019), URL https://link.aps.org/doi/10.1103/PhysRevB.100.115154. 26

[62] A. Shee and D. Zgid, Journal of Chemical Theory and Computation **15**, 6010 (2019), pMID: 31518129, https://doi.org/10.1021/acs.jctc.9b00603, URL https://doi.org/10.1021/acs.jctc.9b00603. 26

[63] F. Coester, Nucl. Phys. **7**, 421 (1958), ISSN 0029-5582, URL http://www.sciencedirect.com/science/article/pii/0029558258902803. 27

[64] F. Coester and H. Kümmel, Nucl. Phys. **17**, 477 (1960), ISSN 0029-5582, URL http://www.sciencedirect.com/science/article/pii/0029558260901401.

[65] J. Čížek, J. Chem. Phys. **45**, 4256 (1966), URL http://scitation.aip.org/content/aip/journal/jcp/45/11/10.1063/1.1727484.

[66] J. Paldus, J. Čížek, and I. Shavitt, Phys. Rev. A **5**, 50 (1972), URL http://link.aps.org/doi/10.1103/PhysRevA.5.50.

[67] G. Purvis and R. Bartlett, J. Chem. Phys. **76**, 1910 (1982), URL http://scitation.aip.org/content/aip/journal/jcp/76/4/10.1063/1.443164. 27, 75

[68] R. J. Bartlett and M. Musiał, Rev. Mod. Phys. **79**, 291 (2007), URL https://link.aps.org/doi/10.1103/RevModPhys.79.291. 27

[69] K. Bhaskaran-Nair, K. Kowalski, and W. A. Shelton, J. Chem. Phys. **144**, 144101 (2016), URL http://scitation.aip.org/content/aip/journal/jcp/144/14/10.1063/1.4944960. 27

[70] B. Peng and K. Kowalski, J. Chem. Theory Comput. **14**, 4335 (2018), URL https://doi.org/10.1021/acs.jctc.8b00313.

[71] B. Peng, R. Van Beeumen, D. B. Williams-Young, K. Kowalski, and C. Yang, Journal of Chemical Theory and Computation **15**, 3185 (2019), pMID: 30951302, https://doi.org/10.1021/acs.jctc.9b00172, URL https://doi.org/10.1021/acs.jctc.9b00172.

[72] F. D. Vila, J. J. Rehr, J. J. Kas, K. Kowalski, and B. Peng, Journal of Chemical Theory and Computation **16**, 6983 (2020), pMID: 33108872, https://doi.org/10.1021/acs.jctc.0c00639, URL https://doi.org/10.1021/acs.jctc.0c00639. 27

[73] J. Kempe, A. Kitaev, and O. Regev, SIAM Journal on Computing **35**, 1070 (2006). 29

[74] J. Kempe and O. Regev, Quantum Info. Comput. **3**, 258–264 (2003), ISSN 1533-7146.

[75] A. Y. Kitaev, A. Shen, M. N. Vyalyi, and M. N. Vyalyi, *Classical and quantum computation*, 47 (American Mathematical Soc., 2002). 29

[76] A. Peruzzo, J. McClean, P. Shadbolt, M.-H. Yung, X.-Q. Zhou, P. J. Love, A. Aspuru-Guzik, and J. L. O'Brien, Nature Communications **5**, 4213 (2014). 30

[77] D. Wecker, M. B. Hastings, and M. Troyer, Phys. Rev. A **92**, 1 (2015), ISSN 10941622. 30, 31

[78] J.-M. Reiner, F. Wilhelm-Mauch, G. Schön, and M. Marthaler, Quantum Science and Technology **4**, 035005 (2019), URL https://doi.org/10.1088%2F2058-9565%2Fab1e85. 30, 31

[79] M. Cerezo, A. Sone, T. Volkoff, L. Cincio, and P. J. Coles, Nature Communications **12** (2021), ISSN 2041-1723, URL http://dx.doi.org/10.1038/s41467-021-21728-w. 30

[80] A. G. Taube and R. J. Bartlett, International Journal of Quantum Chemistry **106**, 3393 (2006). 30

[81] K. M. Nakanishi, K. Mitarai, and K. Fujii, Phys. Rev. Research **1**, 033062 (2019), URL https://link.aps.org/doi/10.1103/PhysRevResearch.1.033062. 31

[82] D. S. Abrams and S. Lloyd, Phys. Rev. Lett. **83**, 5162 (1999), URL https://link.aps.org/doi/10.1103/PhysRevLett.83.5162. 31, 135

[83] Y. Ge, J. Tura, and J. I. Cirac, J. Math. Phys. **60**, 022202 (2019). 32, 89, 93, 94, 95, 103, 106, 111, 147, 152, 159, 161

[84] O. Kyriienko, npj Quantum Information **6**, 7 (2020), ISSN 2056-6387. 32, 33, 91, 93

[85] L. Lin and Y. Tong, Quantum **4**, 372 (2020), ISSN 2521-327X. 41, 89, 94, 95, 109, 152

[86] T. A. Bespalova and O. Kyriienko, PRX Quantum **2**, 030318 (2021), URL https://link.aps.org/doi/10.1103/PRXQuantum.2.030318. 33, 93

[87] M.-Q. He, D.-B. Zhang, and Z. D. Wang, *Quantum gaussian filter for exploring ground-state properties* (2021), 2112.06026.

[88] P. Zeng, J. Sun, and X. Yuan, *Universal quantum algorithmic cooling on a quantum computer* (2021), 2109.15304. 32

[89] D. Amaro, C. Modica, M. Rosenkranz, M. Fiorentini, M. Benedetti, and M. Lubasch, Quantum Science and Technology (2021), URL http://iopscience.iop.org/article/10.1088/2058-9565/ac3e54. 32

[90] S. Apers, S. Chakraborty, L. Novo, and J. Roland, *Quadratic speedup for spatial search by continuous-time quantum walk* (2021), 2112.12746. 32

[91] T. Keen, E. Dumitrescu, and Y. Wang, *Quantum algorithms for ground-state preparation and green's function calculation* (2021), 2112.05731. 32, 49, 88

[92] A. M. Childs, R. Kothari, and R. D. Somma, SIAM Journal on Computing **46**, 1920 (2017). 32, 33, 48, 91

[93] M. Motta, C. Sun, A. T. K. Tan, M. J. O'Rourke, E. Ye, A. J. Minnich, F. G. S. L. Brandão, and G. K.-L. Chan, Nat. Phys. (2019), URL https://doi.org/10.1038/s41567-019-0704-4. 32, 33

[94] B. Bauer, S. Bravyi, M. Motta, and G. K.-L. Chan (2020), 2001.03685. 32, 33

[95] A. N. Chowdhury and R. D. Somma, Quantum Information and Computation **17**, 41 (2017). 33, 94, 102

[96] A. W. Harrow, A. Hassidim, and S. Lloyd, Phys. Rev. Lett. **103**, 150502 (2009). 33, 48

[97] K. Seki and S. Yunoki, PRX Quantum **2**, 010333 (2021), URL https://link.aps.org/doi/10.1103/PRXQuantum.2.010333. 33

[98] E. A. R. Guzman and D. Lacroix, *Predicting ground state, excited states and long-time evolution of many-body systems from short-time evolution on a quantum computer* (2021), 2104.08181. 33

[99] H. F. Trotter, Pacific J. Math. **8**, 887 (1958), ISSN 0030-8730, URL http://projecteuclid.org/euclid.pjm/1103039709. 34

[100] M. Suzuki, Communications in Mathematical Physics **51**, 183 (1976), ISSN 1432-0916, URL https://doi.org/10.1007/BF01609348. 34

[101] M. Suzuki, Journal of Mathematical Physics **32**, 400 (1991), https://doi.org/10.1063/1.529425, URL https://doi.org/10.1063/1.529425. 34

[102] A. M. Childs, D. Maslov, Y. Nam, N. J. Ross, and Y. Su, Proceedings of the National Academy of Sciences **115**, 9456 (2018), ISSN 0027-8424, https://www.pnas.org/content/115/38/9456.full.pdf, URL https://www.pnas.org/content/115/38/9456. 39

[103] A. M. Childs, Y. Su, M. C. Tran, N. Wiebe, and S. Zhu, Phys. Rev. X **11**, 011020 (2021), URL https://link.aps.org/doi/10.1103/PhysRevX.11.011020. 34

[104] J. E. Campbell, Proceedings of the London Mathematical Society **s1-29**, 14 (1897), https://londmathsoc.onlinelibrary.wiley.com/doi/pdf/10.1112/plms/s1-29.1.14, URL https://londmathsoc.onlinelibrary.wiley.com/doi/abs/10.1112/plms/s1-29.1.14. 35

[105] I. D. Kivlichan, C. Gidney, D. W. Berry, N. Wiebe, J. McClean, W. Sun, Z. Jiang, N. Rubin, A. Fowler, A. Aspuru-Guzik, et al., Quantum **4**, 296 (2020), ISSN 2521-327X. 35, 72, 78, 84, 85, 86

[106] G. H. Low and N. Wiebe (2018), 1805.00675. 35

[107] G. H. Low and I. L. Chuang, Quantum **3**, 163 (2019), ISSN 2521-327X, URL https://doi.org/10.22331/q-2019-07-12-163. 36, 40, 56, 71, 72, 78

[108] A. M. Childs and N. Wiebe, Quantum Information and Computation **12** (2012), ISSN 1533-7146, URL http://dx.doi.org/10.26421/QIC12.11-12. 36, 37, 38, 39, 89, 90

[109] D. W. Berry, A. M. Childs, R. Cleve, R. Kothari, and R. D. Somma, Phys. Rev. Lett. **114**, 90502 (2015), URL https://link.aps.org/doi/10.1103/PhysRevLett.114.090502. 39, 40

[110] K. Wan, Quantum **5**, 380 (2021), ISSN 2521-327X, URL http://dx.doi.org/10.22331/q-2021-01-12-380. 40, 72, 78

[111] J. M. Martyn, Y. Liu, Z. E. Chin, and I. L. Chuang, pp. 1–22 (2021), 2110.11327, URL http://arxiv.org/abs/2110.11327. 41

[112] R. Somma, G. Ortiz, J. E. Gubernatis, E. Knill, and R. Laflamme, Phys. Rev. A **65**, 17 (2002), ISSN 10941622. 43, 44, 45

[113] H.-Y. Huang, R. Kueng, and J. Preskill, Nature Physics **16**, 1050 (2020). 45, 46

[114] C. Hadfield, S. Bravyi, R. Raymond, and A. Mezzacapo, arXiv **10598**, 19 (2020), 2006.15788, URL http://arxiv.org/abs/2006.15788. 46

[115] T. Kosugi and Y. I. Matsushita, Physical Review A **101**, 1 (2020). 47, 89

[116] T. Kosugi and Y.-i. Matsushita, Phys. Rev. Research **2**, 033043 (2020), URL https://link.aps.org/doi/10.1103/PhysRevResearch.2.033043. 47, 89

[117] S. Endo, I. Kurata, and Y. O. Nakagawa, Phys. Rev. Research **2**, 033281 (2020), URL https://link.aps.org/doi/10.1103/PhysRevResearch.2.033281. 47, 68

[118] H. Chen, M. Nusspickel, J. Tilly, and G. H. Booth, *A variational quantum eigensolver for dynamic correlation functions* (2021), 2105.01703. 47, 89

[119] G. Aleksandrowicz, T. Alexander, P. Barkoutsos, L. Bello, Y. Ben-Haim, D. Bucher, F. J. Cabrera-Hernández, J. Carballo-Franquis, A. Chen, C.-F. Chen, et al., *Qiskit: An Open-source Framework for Quantum Computing* (2019), URL https://doi.org/10.5281/zenodo.2562111. 48, 79

[120] T. Steckmann, T. Keen, A. F. Kemper, E. F. Dumitrescu, and Y. Wang, *Simulating the mott transition on a noisy digital quantum computer via cartan-based fast-forwarding circuits* (2021), URL https://arxiv.org/abs/2112.05688. 48, 68, 114

[121] A. Roggero, Phys. Rev. A **102**, 022409 (2020), URL https://link.aps.org/doi/10.1103/PhysRevA.102.022409. 49

[122] A. Ciavarella, Phys. Rev. D **102**, 094505 (2020), URL https://link.aps.org/doi/10.1103/PhysRevD.102.094505. 49

[123] T. Keen, T. Maier, S. Johnston, and P. Lougovski, Quantum Science and Technology **5**, 035001 (2020), URL https://doi.org/10.1088/2058-9565/ab7d4c. 50, 70

[124] R. Babbush, N. Wiebe, J. McClean, J. McClain, H. Neven, and G. K.-L. Chan, Phys. Rev. X **8**, 011044 (2018), URL https://link.aps.org/doi/10.1103/PhysRevX.8.011044. 50

[125] J. Preskill, Quantum **2**, 79 (2018), ISSN 2521-327X, URL https://doi.org/10.22331/q-2018-08-06-79. 50

[126] M. Potthoff, Phys. Rev. B **64**, 165114 (2001), URL https://link.aps.org/doi/10.1103/PhysRevB.64.165114. 51, 53, 63, 65, 66

[127] J. M. Kreula, L. García-Álvarez, L. Lamata, S. R. Clark, E. Solano, and D. Jaksch, EPJ Quantum Technol. **3**, 1 (2016), ISSN 21960763, URL http://dx.doi.org/10.1140/epjqt/s40507-016-0049-1. 51, 54, 56, 58

[128] I. Rungger, N. Fitzpatrick, H. Chen, C. H. Alderete, H. Apel, A. Cowtan, A. Patterson, D. M. Ramo, Y. Zhu, N. H. Nguyen, et al. (2019), arXiv:1910.04735. 51, 53, 67, 68

[129] J. R. McClean, J. Romero, R. Babbush, and A. Aspuru-Guzik, New Journal of Physics **18**, 023023 (2016), URL https://doi.org/10.1088%2F1367-2630%2F18%2F2%2F023023. 53

[130] J. M. Kreula, S. R. Clark, and D. Jaksch, Scientific Reports **6**, 1 (2016), ISSN 20452322, URL http://dx.doi.org/10.1038/srep32940. 54, 58

[131] R. Dorner, S. R. Clark, L. Heaney, R. Fazio, J. Goold, and V. Vedral, Phys. Rev. Lett. **110**, 230601 (2013), URL https://link.aps.org/doi/10.1103/PhysRevLett.110.230601. 54, 58

[132] A. M. Childs and N. Wiebe, Quantum Information and Computation **12** (2012), ISSN 1533-7146, URL http://dx.doi.org/10.26421/QIC12.11-12. 56

[133] L. Gui-Lu, Communications in Theoretical Physics **45**, 825–844 (2006), ISSN 0253-6102.

[134] L. Gui-Lu, L. Yang, and W. Chuan, Communications in Theoretical Physics **51**, 65 (2009). 56

[135] P. Jordan and E. Wigner, Zeitschrift für Physik **47**, 631 (1928), ISSN 0044-3328, URL https://doi.org/10.1007/BF01331938. 56

[136] S. B. Bravyi and A. Y. Kitaev, Annals of Physics **298**, 210 (2002), ISSN 0003-4916, URL http://www.sciencedirect.com/science/article/pii/S0003491602962548. 56

[137] H. F. Trotter, Pacific J. Math. **8**, 887 (1958), ISSN 0030-8730, URL http://projecteuclid.org/euclid.pjm/1103039709. 57

[138] M. Suzuki, Communications in Mathematical Physics **51**, 183 (1976), ISSN 1432-0916, URL https://doi.org/10.1007/BF01609348. 57

[139] G. Vidal and C. M. Dawson, Phys. Rev. A **69**, 010301 (2004), URL https://link.aps.org/doi/10.1103/PhysRevA.69.010301. 57

[140] M. W. Coffey, R. Deiotte, and T. Semi, Phys. Rev. A **77**, 066301 (2008), URL https://link.aps.org/doi/10.1103/PhysRevA.77.066301.

[141] N. Klco, E. F. Dumitrescu, A. J. McCaskey, T. D. Morris, R. C. Pooser, M. Sanz, E. Solano, P. Lougovski, and M. J. Savage, Phys. Rev. A **98**, 032331 (2018), URL https://link.aps.org/doi/10.1103/PhysRevA.98.032331. 57

[142] E. Jones, T. Oliphant, P. Peterson, et al., *SciPy: Open source scientific tools for Python* (2001–), URL http://www.scipy.org/. 58

[143] T. Kosugi and Y.-I. Matsushita (2019), 1908.03902. 68

[144] T. Keen, B. Peng, K. Kowalski, P. Lougovski, and S. Johnston, Quantum **6**, 675 (2022), ISSN 2521-327X, URL https://doi.org/10.22331/q-2022-03-30-675. 70

[145] T. Kosugi and Y.-i. Matsushita, Phys. Rev. A **101**, 012330 (2020), URL https://link.aps.org/doi/10.1103/PhysRevA.101.012330. 71

[146] S. Endo, I. Kurata, and Y. O. Nakagawa, Phys. Rev. Research **2**, 033281 (2020), URL https://link.aps.org/doi/10.1103/PhysRevResearch.2.033281. 71

[147] D. W. Berry, A. M. Childs, R. Cleve, R. Kothari, and R. D. Somma, Phys. Rev. Lett. **114**, 90502 (2015), URL https://link.aps.org/doi/10.1103/PhysRevLett.114.090502. 72, 78

[148] J. Noga and R. J. Bartlett, J. Chem. Phys. **86**, 7041 (1987), https://doi.org/10.1063/1.452353, URL https://doi.org/10.1063/1.452353. 75

[149] J. Noga and R. J. Bartlett, J. Chem. Phys. **89**, 3401 (1988), https://doi.org/10.1063/1.455742, URL https://doi.org/10.1063/1.455742.

[150] G. E. Scuseria and H. F. Schaefer, Chem. Phys. Lett. **152**, 382 (1988), ISSN 0009-2614, URL https://www.sciencedirect.com/science/article/pii/0009261488801106. 75

[151] J. Hubbard, Phys. Rev. Lett. **3**, 77 (1959), URL https://link.aps.org/doi/10.1103/PhysRevLett.3.77. 89, 91

[152] R. L. Stratonovich, Soviet Physics Doklady **2**, 416 (1957). 89, 91

[153] S. Endo, I. Kurata, and Y. O. Nakagawa, Physical Review Research **2**, 33281 (2020). 89

[154] A. Roggero and J. Carlson, Phys. Rev. C **100**, 034610 (2019), URL https://link.aps.org/doi/10.1103/PhysRevC.100.034610. 89

[155] Y. Tong, D. An, N. Wiebe, and L. Lin, Physical Review A **104** (2021), ISSN 24699934, arXiv:2008.13295v2. 89

[156] A. M. Childs and N. Wiebe, Quantum Information and Computation **12**, 901 (2012), ISSN 15337146. 93, 98

[157] R. D. Somma and S. Boixo, SIAM Journal on Computing **42**, 593 (2013). 94, 102

[158] M. Thibodeau and B. K. Clark (2021), 2108.03249. 96

[159] D. W. Berry, A. M. Childs, R. Cleve, R. Kothari, and R. D. Somma, in *Proceedings of the Forty-Sixth Annual ACM Symposium on Theory of Computing* (Association for Computing Machinery, New York, NY, USA, 2014), STOC '14, p. 283–292, ISBN 9781450327107. 100

[160] J. S. Pedernales, R. Di Candia, I. L. Egusquiza, J. Casanova, and E. Solano, Phys. Rev. Lett. **113**, 020505 (2014). 100

[161] J. Wouters, H. Katsura, and D. Schuricht, SciPost Phys. Core **4**, 27 (2021). 100

[162] C. T. Gottstein and R. F. Werner, *Ground states of the infinite q-deformed heisenberg ferromagnet* (1995), cond-mat/9501123. 102

[163] F. C. Alcaraz, S. R. Salinas, and W. F. Wreszinski, Phys. Rev. Lett. **75**, 930 (1995), URL https://link.aps.org/doi/10.1103/PhysRevLett.75.930. 100

[164] T. Koma and B. Nachtergaele, Lett. Math. Phys. **40**, 1 (1997). 102

[165] J. Zhou, Y. Hu, X.-B. Zou, and G.-C. Guo, Phys. Rev. A **84**, 042324 (2011). 102, 103

[166] Y. Wang and B. M. Terhal, Phys. Rev. A **104**, 032407 (2021). 103

[167] A. Bärtschi and S. Eidenbenz, in *Fundamentals of Computation Theory*, edited by L. A. Gąsieniec, J. Jansson, and C. Levcopoulos (Springer International Publishing, Cham, 2019), pp. 126–139, ISBN 978-3-030-25027-0. 103

[168] C. S. Mukherjee, S. Maitra, V. Gaurav, and D. Roy, IEEE Trans. Quantum Eng. **1**, 1 (2020). 103

[169] W. J. Huggins, B. A. O'Gorman, C. Neil, N. C. Rubin, P. Roushan, D. R. Reichman, R. Babbush, and J. Lee, pp. 1–28 (2021), 2106.16235, URL http://arxiv.org/abs/2106.16235. 115

[170] Y. Yang, B.-N. Lu, and Y. Li, pp. 1–20 (2021), 2106.09880, URL http://arxiv.org/abs/2106.09880. 115

[171] A. Aspuru-Guzik, A. D. Dutoi, P. J. Love, and M. Head-Gordon, Science **309**, 1704 (2005), ISSN 0036-8075, https://science.sciencemag.org/content/309/5741/1704.full.pdf, URL https://science.sciencemag.org/content/309/5741/1704. 139

[172] Y. Li and S. C. Benjamin, Phys. Rev. X **7**, 021050 (2017), URL https://link.aps.org/doi/10.1103/PhysRevX.7.021050. 140

[173] S. Endo, S. C. Benjamin, and Y. Li, Phys. Rev. X **8**, 031027 (2018), URL https://link.aps.org/doi/10.1103/PhysRevX.8.031027. 140

[174] M. Abramowitz and I. A. Stegun, eds., *Handbook of Mathematical Functions* (National Bureau of Standards, 1964). 148

[175] L. N. Trefethen and J. A. C. Weideman, SIAM Review **56**, 385 (2014). 149, 154

Appendices

A Quantum Sub-Algorithms with Circuit Constructions

A.1 Quantum Fourier Transform

The quantum phase estimation [82] state preparation algorithm includes a quantum Fourier transform [10], so I will introduce that first.

A binary decimal is an object of the form $0.j_l j_{l+1} \ \ldots \ j_m$ where $j_i \in \{0, 1\}$ that stands in place of the number $\frac{j_l}{2} + \frac{j_{l+1}}{4} + \cdots + \frac{j_m}{2^{m-l+1}}$. A quantum Fourier transform maps a state $|j_1, \ldots, j_n\rangle$ as follows [10]:

$$|j_1, \ldots, j_n\rangle \mapsto \frac{1}{2^{n/2}}\big(|0\rangle + e^{2\pi i 0.j_n}|1\rangle\big)\big(|0\rangle + e^{2\pi i 0.j_{n-1}j_n}|1\rangle\big)\ldots\big(|0\rangle + e^{2\pi i 0.j_1 \ldots j_n}|1\rangle\big)$$

Let $R_k \equiv \begin{bmatrix} 1 & 0 \\ 0 & e^{\frac{2\pi i}{2^k}} \end{bmatrix}$. In terms of a circuit diagram the QFT is given in Fig. 1.

A.2 Quantum Phase Estimation

Suppose that we want to estimate an eigenvalue φ_u of a given unitary operator U with corresponding eigenvector $|u\rangle$. To estimate the eigenvalue using quantum phase estimation, we need two quantum registers. The first contains t qubits all initially in the state $|0\rangle$, and we pick t based on the number of digits of accuracy and success probability desired (more on this later). The second register starts in the state $|u\rangle$, or if we don't know the eigenstates of U, start it in a state $|\psi\rangle$ since any state can be written as

$$|\psi\rangle = \sum_u c_u |u\rangle.$$

Quantum phase estimation essentially interferes two trajectories that have a phase difference e^{iEt}, which rotates the qubit, and thus measurement of the qubit's angle of rotation allows us to find that phase difference [15].

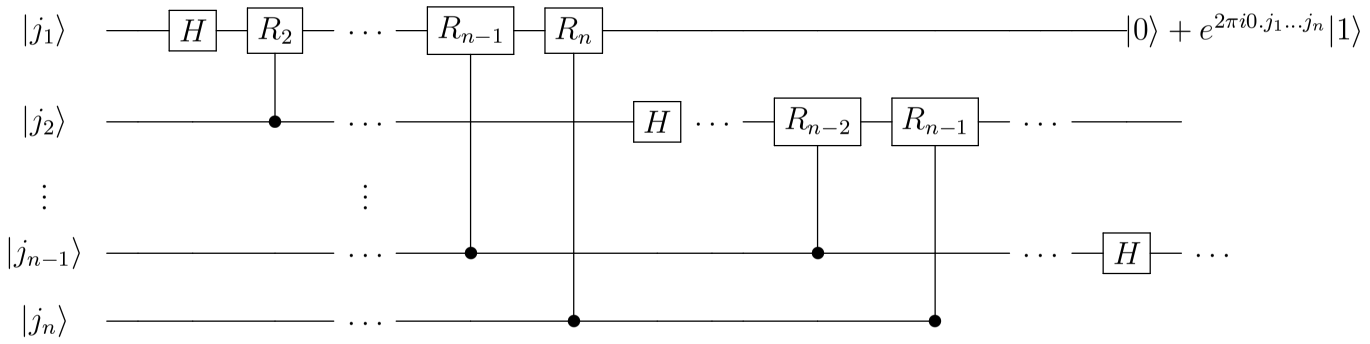

Figure 1: Quantum Fourier Transform circuit diagram. Here it is important to keep in mind that after this procedure, we must also reverse the ordering of the qubits.

Algorithmically, phase estimation can be described as follows:

1. Initialize state $|0\rangle^{\otimes t}|\psi\rangle$

2. Apply Hadamard gates to all qubits in the first register to get the state

$$\frac{1}{2^{t/2}}\sum_{j=0}^{2^t-1}|j\rangle|\psi\rangle$$

3. Apply unitary operators in successive powers of 2 on the second register with the controls on the first register in descending order (see diagram). The state then is

$$\frac{1}{2^{t/2}}\sum_{j=0}^{2^t-1}|j\rangle U^j|\psi\rangle = \frac{1}{2^{t/2}}\sum_{j=0}^{2^t-1}\sum_u c_u e^{2\pi i j\varphi_u}|j\rangle|u\rangle$$

4. Take the inverse Quantum Fourier Transform (see appendix A.1) to get the state

$$\sum_u c_u|\tilde{\varphi}_u\rangle|u\rangle$$

5. Measure the qubits of the first register in the computational basis and convert to binary decimal notation to acquire an n bit approximation $\tilde{\varphi}_u$ to the true eigenvalue φ_u.

Diagrammatically, steps 1-3 of the quantum phase estimation procedure are given in Fig. 2.

When we run the phase estimation algorithm on some arbitrary initial state $|\psi\rangle$, we will get an estimate for the eigenvalue and $|u\rangle$ is randomly chosen with probability $|c_u|^2$. We will get some amount of different frequencies from the inverse quantum Fourier transform. So if $|\psi\rangle$ is a good approximation (or has good "overlap" with) the eigenstate, there will be primarily one frequency with a high probability, giving us the energy. If there are many terms in the expansion, then the algorithm must be repeated many times to find the frequency spectrum.

Suppose we want the eigenvalue accurate to n bits, i.e. we want φ to an accuracy of 2^{-n}, with a success probability $\geq 1-\epsilon$, we should choose $t = n + \lceil \log_2\left(2+\frac{1}{2\epsilon}\right)\rceil$ [10].

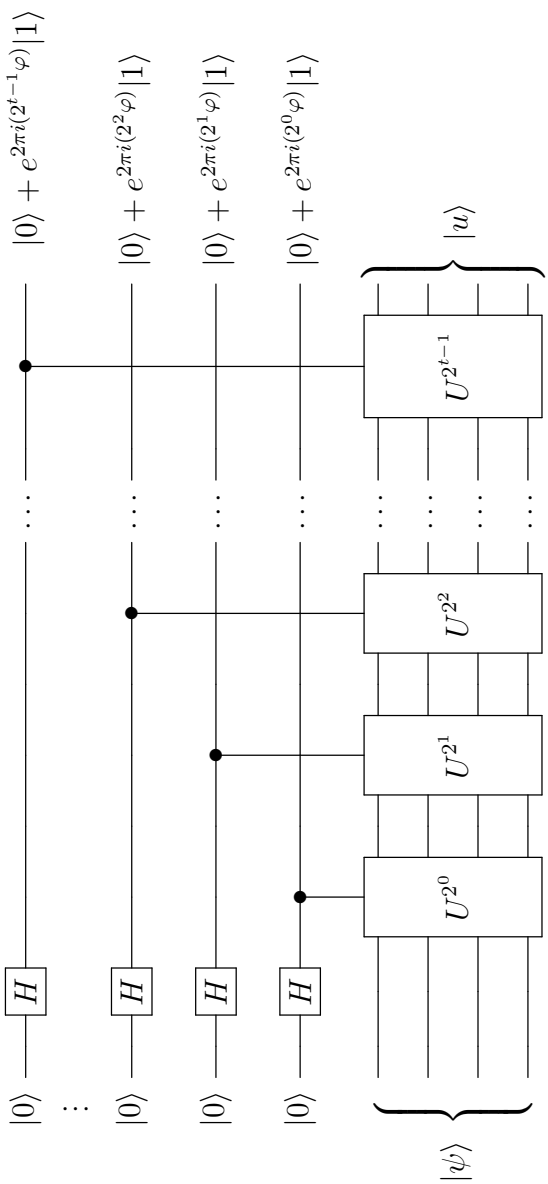

Figure 2: Circuit showing the main parts of the QPE algorithm

There is also a method for finding energies using a recursive QPE technique [171]. Each iteration of the recursive QPE algorithim uses the previous value, thereby giving a lower bound, to calculate the energy for the new iteration. At iteration k, construct $\hat{V}_k = [e^{-2\pi i \phi_{k-1}} \hat{V}_{k-1}]^2$ and shift ϕ_k. By choosing ϕ_k to be one-fourth of the phase estimate for $\hat{V}_k$, we can ensure that the phase of the $\hat{V}_{k+1}$ eigenvalue is approximately centered on the interval zero to one. Then for each iteration, an additional bit of accuracy for the phase is obtained.

B Appendices for Ch. 4

B.1 Error Mitigation Techniques

In the course of the project outlined in Ch. 4, we attempted multiple error mitigation techniques. First, we attempted the linear extrapolation method described in Ref. 172, where we add pairs of CNOTS in parts of the circuit with a CNOT gate, measure the desired expectation value, and use a linear fit to extrapolate the noiseless expectation value. This method proved to be inadequate for the relatively large number of CNOT gates required due to the assumption of a purely depolarizing channel. We saw that the assumption of a purely depolarizing channel breaks down for a large number of CNOT gates, even using the noise model for a device provided by IBM on a simulator, which is known to give more accurate results than the real machine.

We instead use an exponential error mitigation technique as described in Ref. 173. First, we introduced noisy identities composed of one Trotter step unitary and its inverse repeatedly. We then calculated the state fidelity after application and fit the fidelity vs. number of noisy identities data with a decaying exponential. We again assume that the channel is a depolarizing (white noise) channel of the form

$$\mathcal{E}(\rho) = \frac{\epsilon}{d}\mathbb{1} + (1-\epsilon)\rho \tag{1}$$

where d is the dimension of the system. Assuming this white noise channel, the measured expectation value of operator O with respect to density operator ρ is shifted via the equation [173]

$$Tr[O\rho] = \frac{\langle O\rangle_\epsilon}{(1-\epsilon)} - \frac{\epsilon}{d(1-\epsilon)}Tr[O] \tag{2}$$

where d is the dimension of the system and ϵ is the probability of depolarization and decay rate of the exponential fit.

We also implemented a readout error mitigation scheme following the procedure of Ref. 11. First, we put the qubit of interest (in our case the ancillary qubit used for our

measurement scheme) into a known state of $|0\rangle$ or $|1\rangle$. We then measure the qubit without doing any other operations and thus know what the state of the qubit "should" be. Using this, we can find probabilities of measuring $|1\rangle$ when we know it "should" be in state $|0\rangle$ and vice versa. This method allows us to find a shift and contrast factor for making measurements of $\langle Z\rangle$ parameterized by η_0 and η_1, specifically [11]:

$$Z_{\text{new}} = \frac{\hat{Z} - (1 - 2\eta_0)\mathbb{1}}{2\eta_1}. \tag{3}$$

Here, η_0 and η_1 are found by solving

$$1 - \eta_0 - \eta_1 = P(1|0) \tag{4}$$

$$\eta_0 - \eta_1 = P(0|1) \tag{5}$$

with $P(1|0)$ being the probability of reading a qubit in state $|1\rangle$ when it is in the state $|0\rangle$ and similarly for $P(0|1)$.

B.2 Different Methods of Calculating Quasiparticle Weight

A possible alternative to the proposed methods for calculating the quasiparticle weight is to use the Kramers-Kronig relations between the real and imaginary parts of the self-energy to relate $\frac{d\text{Re}[\Sigma(\omega)]}{d\omega}\big|_{\omega=0}$ to an integral over the imaginary part of the self-energy. This method may be preferable since in many cases the "quasiparticle peaks" in the spectral function may not be as pronounced and/or well separated from the rest of the spectrum as here. The integration over the entire spectral range should make this method less sensitive to the unphysical near zero frequency structure in the self-energy, but it is not expected to be entirely immune to this problem. For our case, we found this Kramers-Kronig based method for calculating the derivative of $\frac{d\text{Re}[\Sigma(\omega)]}{d\omega}\big|_{\omega=0}$ to be more accurate than directly taking the derivative on the real axis, but less accurate than integrating the quasiparticle peak of the spectral function for the number of Trotter steps implementable on available quantum computers.

In another attempt to mitigate the errors in calculating the quasiparticle weight, we introduced a small fictitious temperature and transformed all of our quantities to the Matsubara frequency domain, which is described in Sec. 2.1. Specifically, we performed the Hilbert transform of Eq. (4.7) to obtain the Green function in terms of Matsubara frequency. From this, we obtained the self-energy at the first Matsubara frequency as a function of (ficticious) temperature from the Dyson equation. From these quantities, we obtained the imaginary frequency quasiparticle weight as a function of temperature

$$\mathcal{Z}(T) = \frac{1}{1 - \frac{\mathrm{Im}[\Sigma(\pi T)]}{\pi T}}$$

which becomes identical to the real frequency quasiparticle weight in the zero temperature limit. We calculated $\mathcal{Z}(T)$ for many small fictitious temperatures and extrapolated to zero temperature. We again found that the Trotter error caused this method to give completely unreliable results for a Trotter step size of more than a few thousandths, making this method completely impractical for near-term applications. Figure 3(a) shows the Matsubara Green function at the first Matsubara frequency vs. temperature for different size Trotter steps. Figure 3(b) shows the difference between the Matsubara self-energy with no Trotter error and the Matsubara self-energy with different Trotter step sizes vs. temperature, with both self-energies being evaluated at the first Matsubara frequency.

While the Green's function appears to converge rapidly with decreasing Trotter step size, the non-linear relation between the self-energy and the Green's function leads to a large error in the self-energy even for Trotter step sizes where the Green's function is very close to the exact result.

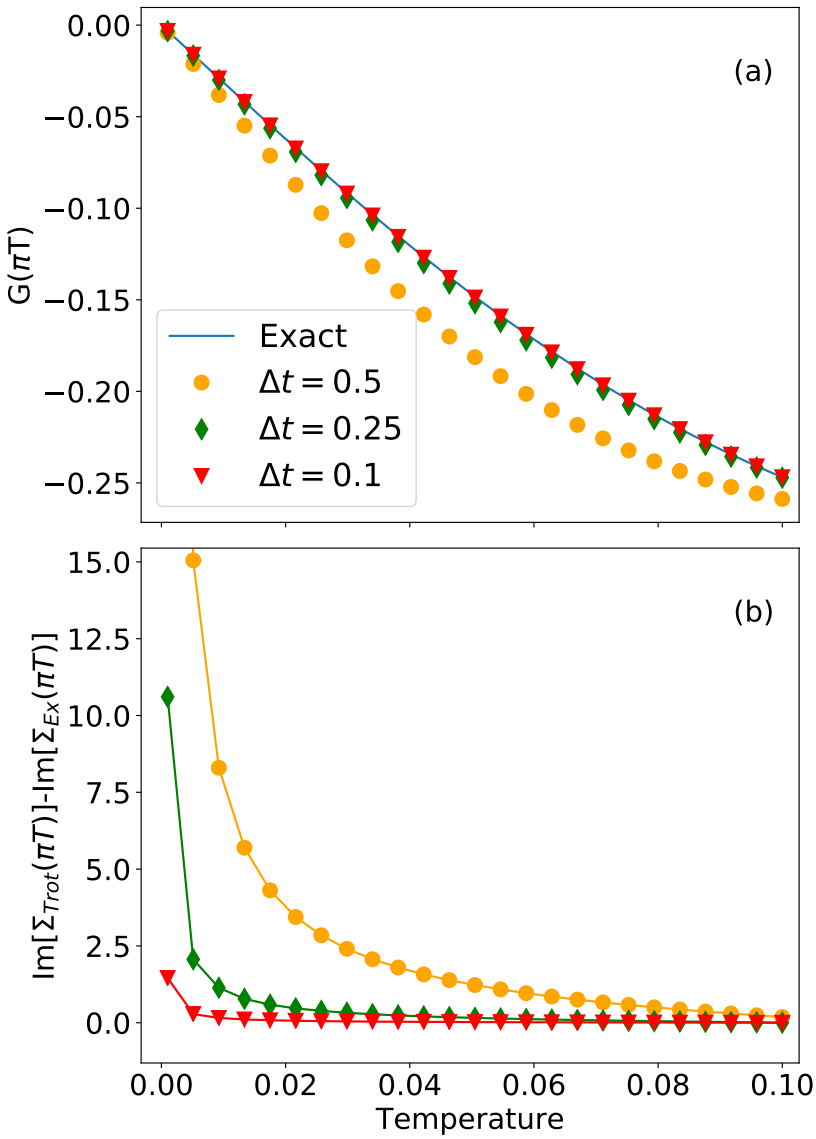

Figure 3: (a) Matsubara Green function at the first Matsubara frequency vs. temperature for different Trotter step sizes at $U = 8t^*$ and $V = t^*$. (b) Difference between the self-energy computed with Trotter fit parameters and the exact self-energy at the first Matsubara frequency vs. temperature for different Trotter step sizes at $U = 8t^*$ and $V = t^*$.

C Appendices for Ch. 5

C.1 Finding Unitaries W and scalar coefficients $\{\mu_i\}$.

If index $p \in O$ denotes impurity site, then one option of $\mathbf{W}_p$ can be obtained through the Jordan-Wigner mapping of the transformed $c_p e^T|\Phi\rangle$. Here, we use the Jordan-Wigner transformation given by

$$\begin{aligned} c_{j\downarrow}^\dagger &= \frac{1}{2}\bigotimes_{k=0}^{j-1} Z_k(X_j - iY_j) \\ c_{j\uparrow}^\dagger &= \frac{1}{2}\bigotimes_{k=0}^{N_{\text{bath}}+j} Z_k(X_{N_{\text{bath}}+j+1} - iY_{N_{\text{bath}}+j+1}), \end{aligned} \tag{6}$$

where the first $N_{\text{bath}}+1$ qubits hold the down occupation information for each site, and the second $N_{\text{bath}}+1$ qubits hold the up occupation information for each site. In the CCSD approximation, this can be expressed as

$$\begin{aligned} c_p e^T|\Phi\rangle &\approx c_p\Big(1 + \sum_{ai} t_i^a c_a^\dagger c_i + \sum_{a<b,i<j} \tilde{t}_{ij}^{ab} c_a^\dagger c_b^\dagger c_j c_i\Big)|\Phi\rangle \\ &= \Big(1 + \sum_{a,i\neq p} t_i^a c_a^\dagger c_i + \sum_{\substack{a<b,i<j \\ i\neq p, j\neq p}} \tilde{t}_{ij}^{ab} c_a^\dagger c_b^\dagger c_j c_i\Big) c_p|\Phi\rangle \\ &= \Big(1 + \sum_{a,i\neq p} t_i^a \big(c_a^\dagger + c_a\big)\big(c_i + c_i^\dagger\big) + \\ &+ \sum_{\substack{a<b,i<j \\ i\neq p, j\neq p}} \tilde{t}_{ij}^{ab} \big(c_a^\dagger + c_a\big)\big(c_b^\dagger + c_b\big)\big(c_j + c_j^\dagger\big)\big(c_i + c_i^\dagger\big)\Big)\big(c_p + c_p^\dagger\big)|\Phi\rangle \\ &= \Big(\tilde{X}_p + \sum_{a,i\neq p} t_i^a \tilde{X}_a \tilde{X}_i \tilde{X}_p + \sum_{\substack{a<b,i<j \\ i\neq p, j\neq p}} \tilde{t}_{ij}^{ab} \tilde{X}_a \tilde{X}_b \tilde{X}_j \tilde{X}_i \tilde{X}_p\Big)|\Phi\rangle, \end{aligned}$$

where $\tilde{t}_{ij}^{ab} = t_{ij}^{ab} + t_i^a t_j^b - t_i^b t_j^a$. The $\mathbf{W}_p$ can then be chosen as

$$\big\{\tilde{X}_p, \{\tilde{X}_a \tilde{X}_i \tilde{X}_p\}_{a,i\neq p}, \{\tilde{X}_a \tilde{X}_b \tilde{X}_j \tilde{X}_i \tilde{X}_p\}_{a<b,i<j,i\neq p,j\neq p}\big\}$$

, and the scalars $\{\mu_i\}$ are the corresponding cluster amplitudes in Eq. (7). $\langle\Phi|(1+\Lambda)e^{-T}c_q^\dagger$ can be expanded by the same set $\mathbf{W}_p$ with the corresponding scalars given by

$$\begin{aligned}
\langle(1+\Lambda)e^{-T}c_q^\dagger c_p\rangle &= \delta_{pq}\big(1-\sum_{i,a}\lambda_a^i t_i^a-\sum_{i<j,a<b}\lambda_{ab}^{ij}\tilde{t}_{ij}^{ab}\big)- \\
&\quad (1-\delta_{pq})\big(\sum_a \lambda_a^p t_q^a-\sum_{i,a<b}\lambda_{ab}^{pi}\tilde{t}_{qi}^{ab}\big), \\
\langle(1+\Lambda)e^{-T}c_q^\dagger c_p c_a^\dagger c_i\rangle &= \delta_{pq}\big(\lambda_a^i-\sum_{j,b}\lambda_{ab}^{ij}t_j^b\big)-(1-\delta_{pq})\sum_b\lambda_{ab}^{ip}t_q^b, \\
\langle(1+\Lambda)e^{-T}c_q^\dagger c_p c_a^\dagger c_b^\dagger c_j c_i\rangle &= \delta_{pq}\lambda_{ab}^{ij}.
\end{aligned}$$

Similarly, we can transform $c_q^\dagger e^T|\phi\rangle$,

$$\begin{aligned}
c_q^\dagger e^T|\Phi\rangle &\approx c_q^\dagger\Big(1+\sum_{ai}t_i^a c_a^\dagger c_i+\sum_{a<b,i<j}\tilde{t}_{ij}^{ab}c_a^\dagger c_b^\dagger c_j c_i\Big)|\Phi\rangle \\
&= \Big(1+\sum_{a\neq q,i}t_i^a c_a^\dagger c_i+\sum_{\substack{a<b,i<j\\a\neq q,b\neq q}}\tilde{t}_{ij}^{ab}c_a^\dagger c_b^\dagger c_j c_i\Big)c_q^\dagger|\Phi\rangle \\
&= \Big(\tilde{X}_q+\sum_{a\neq q,i}t_i^a\tilde{X}_a\tilde{X}_i\tilde{X}_q+\sum_{\substack{a<b,i<j\\a\neq q,b\neq q}}\tilde{X}_j\tilde{X}_i\tilde{X}_q\Big)|\Phi\rangle,
\end{aligned}$$

to get another set of unitaries and corresponding scalars for greater part of the coupled cluster Green's function.

It is worth mentioning that the cluster amplitudes, t's, in the present context are obtained from classical CCSD calculation on AIM, which numerically scales $\mathcal{O}(N_s^2N_o^2)$ (N_o denoting the number of occupied spin-orbitals and N_s denoting the number of virtual spin-orbitals).

D Appendices for Ch. 6

D.1 Proof of Lemma 1

Consider a Hamiltonian $\hat{H}$ with a spectral representation $\hat{H} = \sum_l \lambda_l |\lambda_l\rangle\langle\lambda_l|$, where all eigenvalues $\lambda_l \geq 0$. Denote the ground state $|\lambda_0\rangle$ and the first excited state $|\lambda_1\rangle$, and the spectral gap $\Delta_s = \lambda_1 - \lambda_0 > 0$. Given a normalized initial state $|\psi_0\rangle$ that has overlap with ground state $|\langle\lambda_0|\psi_0\rangle| = \gamma > 0$, we derive a lower bound for the parameter t in the operator $f(\hat{H}) = e^{-\frac{1}{2}t^2\hat{H}^2}$ so that the projected state $|\tilde{\psi}\rangle = f(\hat{H})|\psi_0\rangle$, after the normalization $|\psi\rangle = |\tilde{\psi}\rangle / \||\tilde{\psi}\rangle\|$, is ϵ-close to the ground state. That is, the infidelity $1 - |\langle\lambda_0|\psi\rangle| < \epsilon$, and, equivalently, the Euclidean distance $\||\psi\rangle - |\lambda_0\rangle\| < \sqrt{2\epsilon} \equiv \eta$.

Expand $|\psi_0\rangle$ in the eigenbasis: $|\psi_0\rangle = c_0|\lambda_0\rangle + \sum_{l>0} c_l|\lambda_l\rangle$. For degenerate ground states, $\hat{H}|\lambda_0^\alpha\rangle = \lambda_0|\lambda_0^\alpha\rangle$, the initial state is given by $|\psi_0\rangle = \sum_\alpha c_0^\alpha|\lambda_0^\alpha\rangle + \sum_{l>0} c_l|\lambda_l\rangle = c_0|\lambda_0\rangle + \sum_{l>0} c_l|\lambda_l\rangle$, where $c_0 \equiv (\sum_\alpha |c_0^\alpha|^2)^{1/2}$ and $|\lambda_0\rangle \equiv \sum_\alpha (c_0^\alpha/c_0)|\lambda_0^\alpha\rangle$.

Note that although we define Δ_s to be the exact spectral gap $\lambda_1 - \lambda_0$ and γ the exact overlap $|c_0|$ between the initial state and the ground state, lower bounds of these parameters can be used when the exact values are not known *a priori* and all complexity bounds proved here still hold, just not as tight as when exact values are used.

$$|\tilde{\psi}\rangle = f(\hat{H})\,|\psi_0\rangle = e^{-\frac{1}{2}t^2\hat{H}^2}\,|\psi_0\rangle \tag{7}$$

$$= c_0 e^{-\frac{1}{2}t^2\lambda_0^2}\left[|\lambda_0\rangle + \sum_{l>0}\frac{c_l}{c_0}e^{-\frac{1}{2}t^2(\lambda_l^2-\lambda_0^2)}\,|\lambda_l\rangle\right], \tag{8}$$

$$|\psi\rangle = |\tilde{\psi}\rangle\,/\|\,|\tilde{\psi}\rangle\|\,. \tag{9}$$

$$1 - |\,\langle\lambda_0|\psi\rangle\,| = 1 - \left[1 + \sum_{l>0}\frac{|c_l|^2}{|c_0|^2}e^{-t^2(\lambda_l^2-\lambda_0^2)}\right]^{-1/2} \tag{10}$$

$$\leq 1 - \left[1 + e^{-t^2(\lambda_1^2-\lambda_0^2)}\sum_{l>0}\frac{|c_l|^2}{|c_0|^2}\right]^{-1/2} \tag{11}$$

$$= 1 - \left[1 + e^{-t^2(\lambda_1^2-\lambda_0^2)}\frac{1-\gamma^2}{\gamma^2}\right]^{-1/2} \tag{12}$$

$$< 1 - \left[1 - \frac{1}{2}e^{-t^2(\lambda_1^2-\lambda_0^2)}\frac{1-\gamma^2}{\gamma^2}\right] \tag{13}$$

$$= e^{-t^2(\lambda_1^2-\lambda_0^2)}\frac{1-\gamma^2}{2\gamma^2}. \tag{14}$$

To make the infidelity $1 - |\,\langle\lambda_0|\psi\rangle\,| < \epsilon$, it is sufficient to set

$$e^{-t^2(\lambda_1^2-\lambda_0^2)}\frac{1-\gamma^2}{2\gamma^2} = e^{-t^2[(\lambda_0+\Delta_s)^2-\lambda_0^2]}\frac{1-\gamma^2}{2\gamma^2} \tag{15}$$

$$\leq e^{-t^2[(\lambda_0+\Delta)^2-\lambda_0^2]}\frac{1-\gamma^2}{2\gamma^2} < \epsilon \tag{16}$$

$$\implies t > \frac{1}{\Delta}\left[\log\left(\frac{1-\gamma^2}{2\gamma^2\epsilon}\right)\right]^{1/2}\left(1 + \frac{2\lambda_0}{\Delta}\right)^{-1/2} \tag{17}$$

$$= \frac{1}{\Delta}\left[2\log\left(\frac{1}{\gamma\eta}\right) + \log\left(1-\gamma^2\right)\right]^{1/2}\left(1 + \frac{2\lambda_0}{\Delta}\right)^{-1/2} \tag{18}$$

$$= \mathcal{O}\left(\frac{1}{\Delta}\sqrt{2\log\frac{1}{\gamma\eta}}\right). \tag{19}$$

The final expression has been given in a form to easily compare with Ge *et al.* [83] involving the typical factors $\frac{1}{\Delta}$ and $\log\frac{1}{\gamma\eta}$.

D.2 Discretization and truncation

Now we proceed to give the conditions to satisfy $\|h(\hat{H}) - f(\hat{H})\| \leq \epsilon' = \gamma\eta$. Since $\|h(\hat{H}) - f(\hat{H})\| \leq \|h(\hat{H}) - h^{\infty}(\hat{H})\| + \|h^{\infty}(\hat{H}) - f(\hat{H})\| \equiv \epsilon_t + \epsilon_d$, where the first term is the truncation error and the second discretization error. Here, $h^{\infty}(\hat{H})$ is the infinite sum without truncation at $k = \pm N_z$. Now we find the conditions so that $\epsilon_t + \epsilon_d < \epsilon'$; and we find the optimal conditions in the balanced case $\epsilon_t = \epsilon_d < \epsilon'/2$.

The truncation error $\epsilon_t < e^{-z_c^2/2}$ can be shown as follows.

$$
\begin{aligned}
\epsilon_t &= \left\| h(\hat{H}) - h^{\infty}(\hat{H}) \right\| && (20)\\
&= \left\| \frac{1}{\sqrt{2\pi}} \sum_{|k|=N_z+1}^{\infty} \Delta_z e^{-\frac{1}{2}k^2\Delta_z^2} e^{-itk\Delta_z \hat{H}} \right\| && (21)\\
&\leq \frac{2}{\sqrt{2\pi}} \sum_{k=N_z+1}^{\infty} \Delta_z e^{-\frac{1}{2}k^2\Delta_z^2} && (22)\\
&< \frac{2}{\sqrt{2\pi}} \int_{N_z\Delta_z}^{\infty} dz\, e^{-\frac{1}{2}z^2} = \frac{2}{\sqrt{\pi}} \int_{z_c/\sqrt{2}}^{\infty} dx\, e^{-x^2} && (23)\\
&\leq \frac{e^{-z_c^2/2}}{\frac{\sqrt{\pi}z_c}{2\sqrt{2}} + \sqrt{\left(\frac{\sqrt{\pi}z_c}{2\sqrt{2}}\right)^2 + 1}} && (24)\\
&= \exp\left(-\frac{z_c^2}{2} - \operatorname{arcsinh} \frac{\sqrt{\pi}z_c}{2\sqrt{2}} \right) && (25)\\
&= \exp\left(-\frac{z_c^2}{2} - \frac{1}{2} \operatorname{arccosh}\left(\frac{\pi z_c^2}{4} + 1 \right) \right) && (26)\\
&\equiv e^{-z_c'^2/2} < e^{-z_c^2/2}, && (27)
\end{aligned}
$$

where $z_c \equiv N_z\Delta_z$ and $z_c' \equiv [z_c^2 + \operatorname{arccosh}(\pi z_c^2/4 + 1)]^{1/2}$. In the above, we used the fact that $\sum_{k=N_z+1}^{\infty}$ is the right Riemann sum of the integral $\int_{N_z\Delta_z}^{\infty} dz$ of a monotonically decreasing function and hence is an underestimation. In the third to the last step, the inequality used to bound the integral is from Eq. (7.1.13) of Ref. 174.

$\forall b \in (-a, a)$, we define M as an upper bound of the following integral

$$\int_{-\infty}^{\infty} dx \, \|f(x+ib)\| = \frac{1}{\sqrt{2\pi}} \int_{-\infty}^{\infty} dx \left\| e^{-\frac{1}{2}(x+ib)^2} e^{-it(x+ib)\hat{H}} \right\| \tag{28}$$

$$= \frac{1}{\sqrt{2\pi}} \int_{-\infty}^{\infty} dx \, e^{-\frac{1}{2}x^2} e^{\frac{1}{2}b^2} \left\| e^{tb\hat{H}} \right\| \tag{29}$$

$$= e^{\frac{1}{2}b^2} \left\| e^{tb\hat{H}} \right\| \leq e^{\frac{1}{2}b^2 + t|b|} \leq e^{\frac{1}{2}a^2 + ta} \equiv M. \tag{30}$$

We have assumed the spectrum of Hamiltonian operator $\sigma(\hat{H}) \in [0, 1]$ so the spectrum norm $\|\hat{H}\| \leq 1$. Then, by the Theorem 5.1 of Ref. 175, the discretization error is

$$\epsilon_d = \left\| h^{\infty}(\hat{H}) - f(\hat{H}) \right\| \tag{31}$$

$$\leq \frac{2M}{e^{2\pi a/\Delta_z} - 1} = \frac{2e^{\frac{1}{2}a^2 + ta}}{e^{2\pi a/\Delta_z} - 1} \tag{32}$$

$$\approx 2 \exp\left(\frac{1}{2}a^2 + ta - \frac{2\pi a}{\Delta_z} \right) \tag{33}$$

$$= 2 \exp\left[-a \left(\frac{2\pi}{\Delta_z} - t - \frac{a}{2} \right) \right]. \tag{34}$$

Now, we solve for a that minimizes the above for $2\pi/\Delta_z > t$. That is, we find a that maximizes $a\left(\frac{2\pi}{\Delta_z} - t - \frac{a}{2}\right)$ for $a > 0$. So $a = \frac{2\pi}{\Delta_z} - t$ and $\epsilon_d \leq e^{-[(2\pi/\Delta_z) - t]^2/2}$. At this optimal condition, the balance condition $\epsilon_d = \epsilon_t$ leads to $(2\pi/\Delta_z) - t = z_c'$, i.e., the step size $\Delta_z = 2\pi/(z_c' + t)$. Therefore, $N_z = z_c/\Delta_z = z_c(z_c' + t)/2\pi$. Finally, $\epsilon_t = \epsilon_d < \epsilon'/2 = \gamma\eta/2$ gives $z_c = \mathcal{O}\left(\sqrt{\log \frac{1}{\gamma\eta}}\right)$.

D.3 Proof of Theorem 2

So far we have proved that $1 - |\langle \lambda_0 | \psi \rangle| < \epsilon$, provided $t > \frac{1}{\Delta_s}\sqrt{2 \log \frac{1}{\gamma\eta}}$. Combining this bound with Eqs. (7), (8), (10), we have

$$\gamma e^{-\frac{1}{2}t^2\lambda_0^2} \leq \left\| f(\hat{H}) \, |\psi_0\rangle \right\| \leq \gamma e^{-\frac{1}{2}t^2\lambda_0^2} \frac{1}{1-\epsilon} \tag{35}$$

$$\implies \left\| f(\hat{H}) \, |\psi_0\rangle \right\| = \gamma e^{-\frac{1}{2}t^2\lambda_0^2} (1 + \mathcal{O}(\eta^2)). \tag{36}$$

If we use the discretized and truncated LCU formula $h(\hat{H})$ instead of $f(\hat{H})$, we will prove below that given $t = \mathcal{O}\Big(\frac{1}{\Delta_s}\sqrt{\log\frac{1}{\gamma\eta}}\Big)$, $|\lambda_0| < \delta_0 = \mathcal{O}\Big(\Delta_s/\sqrt{\log\frac{1}{\gamma\eta}}\Big)$, and $\|h(\hat{H}) - f(\hat{H})\| < \epsilon' = \gamma\eta$ then the state prepared by applying $h(\hat{H})$ is ϵ-close to the ground state,

$$\left\| \frac{h(\hat{H})\,|\psi_0\rangle}{\|h(\hat{H})\,|\psi_0\rangle\|} - |\lambda_0\rangle \right\| \leq \eta(1 + 2e^{\frac{1}{2}t^2\lambda_0^2}) = \mathcal{O}(\eta). \tag{37}$$

Here, δ_0 is equivalent to the precision of the ground energy $\tilde{\lambda}_0$ known *a priori* for a given Hamiltonian $\tilde{H}$. Before executing our algorithm, we shift $\tilde{H}$ to $\hat{H}$ by a constant so that the same ground state now has the ground energy λ_0 satisfying $|\lambda_0| < \delta_0$. First, for any two vectors $|u\rangle$ and $|v\rangle$,

$$\left\| \frac{|u\rangle}{\||u\rangle\|} - \frac{|v\rangle}{\||v\rangle\|} \right\| = \left\| \frac{|u\rangle - |v\rangle}{\||u\rangle\|} + \frac{|v\rangle}{\||u\rangle\|} - \frac{|v\rangle}{\||v\rangle\|} \right\| \tag{38}$$

$$\leq \frac{\||u\rangle - |v\rangle\|}{\||u\rangle\|} + \frac{\||v\rangle\,(\||v\rangle\| - \||u\rangle\|)\|}{\||u\rangle\|\||v\rangle\|} \tag{39}$$

$$= \frac{\||u\rangle - |v\rangle\|}{\||u\rangle\|} + \frac{|\||u\rangle\| - \||v\rangle\||}{\||u\rangle\|} \tag{40}$$

$$\leq \frac{\||u\rangle - |v\rangle\|}{\||u\rangle\|} + \frac{\||u\rangle - |v\rangle\|}{\||u\rangle\|} \tag{41}$$

$$= \frac{2\||u\rangle - |v\rangle\|}{\||u\rangle\|}. \tag{42}$$

In the second to the last step, we used the reverse triangle inequality. Similarly, we have $\| |u\rangle / \||u\rangle\| - |v\rangle / \||v\rangle\| \| \leq 2\||u\rangle - |v\rangle\|/\||v\rangle\|$. Then,

$$\left\| \frac{h(\hat{H})\,|\psi_0\rangle}{\|h(\hat{H})\,|\psi_0\rangle\|} - |\lambda_0\rangle \right\| = \left\| \frac{h(\hat{H})\,|\psi_0\rangle}{\|h(\hat{H})\,|\psi_0\rangle\|} - \frac{f(\hat{H})\,|\psi_0\rangle}{\|f(\hat{H})\,|\psi_0\rangle\|} + \frac{f(\hat{H})\,|\psi_0\rangle}{\|f(\hat{H})\,|\psi_0\rangle\|} - |\lambda_0\rangle \right\| \tag{43}$$

$$\leq \left\| \frac{h(\hat{H})\,|\psi_0\rangle}{\|h(\hat{H})\,|\psi_0\rangle\|} - \frac{f(\hat{H})\,|\psi_0\rangle}{\|f(\hat{H})\,|\psi_0\rangle\|} \right\| + \left\| \frac{f(\hat{H})\,|\psi_0\rangle}{\|f(\hat{H})\,|\psi_0\rangle\|} - |\lambda_0\rangle \right\| \tag{44}$$

$$\leq \frac{2\|[h(\hat{H}) - f(\hat{H})]\,|\psi_0\rangle\|}{\|f(\hat{H})\,|\psi_0\rangle\|} + \eta \tag{45}$$

$$\leq \frac{2\gamma\eta}{\gamma e^{-\frac{1}{2}t^2\lambda_0^2}} + \eta \tag{46}$$

$$= \eta(1 + 2e^{\frac{1}{2}t^2\lambda_0^2}) = \mathcal{O}(\eta). \tag{47}$$

In the second to the last step, we used $\|[h(\hat{H}) - f(\hat{H})]\,|\psi_0\rangle\| \leq \|h(\hat{H}) - f(\hat{H})\| < \gamma\eta$ and $\|f(\hat{H})\,|\psi_0\rangle\| \geq \gamma e^{-\frac{1}{2}t^2\lambda_0^2}$. In the last step, we used $t\lambda_0 = \mathcal{O}(1)$.

Denote the normalized ground state prepared by the LCU operator as

$$|\psi\rangle = h(\hat{H})\,|\psi_0\rangle\,/\|h(\hat{H})\,|\psi_0\rangle\|\,,$$

the error bound on the fidelity can be derived as follows:

$$1 - |\langle\lambda_0|\psi\rangle| \leq |1 - \langle\lambda_0|\psi\rangle| \tag{48}$$

$$= |\langle\lambda_0|\lambda_0\rangle - \langle\lambda_0|\psi\rangle)| = |\langle\lambda_0|\,(|\lambda_0\rangle - |\psi\rangle)| \tag{49}$$

$$\leq \||\lambda_0\rangle\|\||\lambda_0\rangle - |\psi\rangle\| \tag{50}$$

$$= \left\| |\lambda_0\rangle - \frac{h(\hat{H})\,|\psi_0\rangle}{\|h(\hat{H})\,|\psi_0\rangle\|} \right\| \tag{51}$$

$$\leq \eta(1 + 2e^{\frac{1}{2}t^2\lambda_0^2}). \tag{52}$$

In the first step above, we used the reverse triangle inequality $1 - |z| \leq |1 - z|$, $\forall z \in \mathbb{C}$. The second inequality used is Cauchy-Schwarz inequality $|\langle u|v\rangle| \leq \|u\|\|v\|$. The last inequality is 37. Considering the general bounds for fidelity $0 \leq 1 - |\langle\lambda_0|\psi\rangle| \leq 1$ for any two normalized

vectors, the above upper bound $\eta(1+2e^{\frac{1}{2}t^2\lambda_0^2})$ is only useful if $\eta(1+2e^{\frac{1}{2}t^2\lambda_0^2}) < 1$. In this case, a tighter error bound $(\eta^2/2)(1+2e^{\frac{1}{2}t^2\lambda_0^2})^2$ is derived as follows.

$$1 - |\langle\lambda_0|\psi\rangle| \leq \frac{1}{2}(2 - 2\,\mathrm{Re}\,\langle\lambda_0|\psi\rangle) \tag{53}$$

$$= \frac{1}{2}(\langle\lambda_0|\lambda_0\rangle + \langle\psi|\psi\rangle - \langle\lambda_0|\psi\rangle - \langle\psi|\lambda_0\rangle) \tag{54}$$

$$= \frac{1}{2}\||\psi\rangle - |\lambda_0\rangle\|^2 \tag{55}$$

$$\leq \frac{\eta^2}{2}(1+2e^{\frac{1}{2}t^2\lambda_0^2})^2. \tag{56}$$

Finally, the query complexity is $\alpha t z_c/\gamma = \mathcal{O}\Big(\frac{\alpha}{\gamma\Delta_s}\log\frac{1}{\gamma\eta}\Big)$, where the factor of $1/\gamma$ comes from the minimum label finding algorithm (or amplitude amplification) in Ref. 83 to get an estimate for the ground state energy. This is the same complexity as Ge *et al.* [83] and Lin and Tong [85] for ground state preparation (ground energy known within a bound δ). But our bound $\delta = \mathcal{O}\Big(\Delta_s/\sqrt{\log\frac{1}{\gamma\eta}}\Big)$, derived in Appendix D.5, quadratically reduces the precision requirement reported in Ge *et al.* [83] of $\delta = \mathcal{O}\Big(\Delta_s/\log\frac{1}{\gamma\eta}\Big)$.

A short summary of parameters to set in numerical calculations.

- $\gamma = |\,\langle\lambda_0|\psi_0\rangle\,|$
- $\epsilon = 1 - |\,\langle\lambda_0|\psi_t\rangle\,|$; $\eta = \||\psi_t\rangle - |\lambda_0\rangle\| \approx \sqrt{2\epsilon}$
- $t = \mathcal{O}\Big(\frac{1}{\Delta_s}\sqrt{\log\frac{1}{\gamma\eta}}\Big)$
- $z_c = \mathcal{O}\Big(\sqrt{\log\frac{1}{\gamma\eta}}\Big)$
- $\Delta_z = 2\pi/(z_c' + t)$; $N_z = [z_c/\Delta_z]$

D.4 Proof of Theorem 3

First, let us confirm that through the Fourier-Laplace integral transform (FIT) we do in fact recover the resolvent operator.

$$R(\omega + i\Gamma, \hat{H}) = -i \int_0^\infty \mathrm{d}t\, e^{i(\omega+i\Gamma)t} e^{-it\hat{H}} \tag{57}$$

$$= -i \int_0^\infty \mathrm{d}t\, e^{i(\omega-\hat{H}+i\Gamma)t} \quad (\Gamma > 0) \tag{58}$$

$$= -i \left. \frac{e^{i(\omega-\hat{H})t} e^{-\Gamma t}}{i(\omega - \hat{H} + i\Gamma)} \right|_0^\infty \tag{59}$$

$$= -i \frac{e^{i(\omega-\hat{H})\infty} e^{-\Gamma\infty} - e^{i(\omega-\hat{H})0} e^{-\Gamma 0}}{i(\omega - \hat{H} + i\Gamma)} \tag{60}$$

$$= \frac{1}{\omega - \hat{H} + i\Gamma}. \tag{61}$$

$$\tag{62}$$

Next, we discretize the FIT to express it as an LCU.

$$
\begin{aligned}
h(\omega + i\Gamma, \hat{H}) &= -i \sum_{k=0}^{N_c} \Delta_t \, e^{i(\omega - \hat{H} + i\Gamma)k\Delta_t} && (63)\\
&= -i \sum_{k=0}^{N_c} \Delta_t \left[e^{i(\omega - \hat{H} + i\Gamma)\Delta_t} \right]^k && (64)\\
&= -i\Delta_t \frac{1 - e^{i(\omega - \hat{H} + i\Gamma)\Delta_t (N_c+1)}}{1 - e^{i(\omega - \hat{H} + i\Gamma)\Delta_t}} && (65)\\
&\approx \frac{i\Delta_t}{e^{i(\omega - \hat{H} + i\Gamma)\Delta_t} - 1} && (66)\\
&\text{since } \lim_{N_c\Delta_t \to \infty} e^{-\Gamma \Delta_t (N_c+1)} \to 0 && (67)\\
&\approx \frac{i\Delta_t}{i(\omega - \hat{H} + i\Gamma)\Delta_t} && (68)\\
&\text{since } \lim_{x \to 0} e^x - 1 \to x && (69)\\
&= \frac{1}{\omega - \hat{H} + i\Gamma} = R(\omega + i\Gamma, \hat{H}). && (70)\\
& && (71)
\end{aligned}
$$

We then borrow the general method and notation of Ref. 175 and bound the truncation (ϵ_t) and discretization error (ϵ_d) defined as:

$$
\begin{aligned}
&\left\| h(\omega + i\Gamma, \hat{H}) - R(\omega + i\Gamma, \hat{H}) \right\| \\
&\leq \left\| h(\omega + i\Gamma, \hat{H}) - h^{\infty}(\omega + i\Gamma, \hat{H}) \right\| + \left\| h^{\infty}(\omega + i\Gamma, \hat{H}) - R(\omega + i\Gamma, \hat{H}) \right\| \qquad (72)\\
&\equiv \epsilon_t + \epsilon_d.
\end{aligned}
$$

Suppose we want to limit the sum of truncation and discretization errors to $\epsilon_t + \epsilon_d = \epsilon'$. We can choose the balanced case $\epsilon_t = \epsilon_d = \frac{\epsilon'}{2}$. For truncation error,

$$\epsilon_t = \left\| h(\omega + i\Gamma, \hat{H}) - h^{\infty}(\omega + i\Gamma, \hat{H}) \right\| \tag{73}$$

$$= \left\| \sum_{k=N_c+1}^{\infty} \Delta_t e^{i(\omega - \hat{H} + i\Gamma)k\Delta t} \right\| \tag{74}$$

$$\leq \sum_{k=N_c+1}^{\infty} \Delta_t \left\| e^{i(\omega - \hat{H})k\Delta t} \right\| e^{-\Gamma k \Delta t} \tag{75}$$

$$(e^{-\Gamma k \Delta t} < 1 \ \forall \Gamma > 0, \Delta_t > 0, k > 0) \tag{76}$$

$$= \Delta_t \frac{\left\| e^{i(\omega - H)(N_c+1)\Delta_t} \right\| e^{-\Gamma(N_c+1)\Delta_t}}{1 - \left\| e^{i(\omega - H)\Delta_t} \right\| e^{-\Gamma \Delta_t}} \tag{77}$$

$$= \frac{\Delta_t e^{-\Gamma(N_c+1)\Delta_t}}{1 - e^{-\Gamma \Delta_t}} = \frac{\Delta_t e^{-\Gamma N_c \Delta_t}}{e^{\Gamma \Delta_t} - 1} \quad (N_c \Delta_t = t_c) \tag{78}$$

$$= \frac{\Gamma \Delta_t}{e^{\Gamma \Delta_t} - 1} \frac{e^{-\Gamma t_c}}{\Gamma} < \frac{e^{-\Gamma t_c}}{\Gamma}. \tag{79}$$

In the last step, we have used $\frac{x}{e^x - 1} = x/(x + \frac{1}{2!}x^2 + \dots) < 1$, $\forall x = \Gamma \Delta_t > 0$. Solving $\epsilon_t < \frac{e^{-\Gamma t_c}}{\Gamma} = \frac{\epsilon'}{2}$, we find

$$t_c = \frac{1}{\Gamma} \log\left(\frac{2}{\Gamma \epsilon'}\right), \tag{80}$$

$$N_c = \frac{t_c}{\Delta_t} = \frac{1}{\Gamma \Delta_t} \log\left(\frac{2}{\Gamma \epsilon'}\right). \tag{81}$$

Now we inspect the discretization error ϵ_d.

$$\epsilon_d = \left\| h^{\infty}(\omega + i\Gamma, \hat{H}) - R(\omega + i\Gamma, \hat{H}) \right\| \tag{82}$$

$$= \left\| \frac{i\Delta_t}{e^{i(\omega - \hat{H} + i\Gamma)\Delta_t} - 1} - \frac{1}{\omega - \hat{H} + i\Gamma} \right\| \tag{83}$$

$$= \Delta_t \left\| \frac{1}{e^z - 1} - \frac{1}{z} \right\| \quad (z = i(\omega - \hat{H} + i\Gamma)\Delta_t) \tag{84}$$

$$= \Delta_t \left\| -\frac{1}{2} + \frac{z}{12} + \mathcal{O}\big(z^3\big) \right\| \tag{85}$$

$$< \frac{1}{2}\Delta_t + \frac{2W}{12}\Delta_t^2 + \left\| \mathcal{O}\big(\Delta_t^4\big) \right\|. \tag{86}$$

$$W \equiv \left\| \omega - \hat{H} + i\Gamma \right\| /2 \tag{87}$$

$$\lesssim \left| \lambda_{\max}(\hat{H}) - \lambda_{\min}(\hat{H}) \right| /2 \tag{88}$$

$$(\forall \omega \in \Big[\lambda_{\min}(\hat{H}), \lambda_{\max}(\hat{H})\Big], \tag{89}$$

$$\Gamma \ll \max\Big\{ \left|\lambda_{\min}(\hat{H})\right|, \left|\lambda_{\max}(\hat{H})\right| \Big\})$$

$$\leq (\left|\lambda_{\max}(\hat{H})\right| + \left|\lambda_{\min}(\hat{H})\right|)/2$$

$$< (\left\|\hat{H}\right\|_s + \left\|\hat{H}\right\|_s)/2 = \left\|\hat{H}\right\|_s, \tag{90}$$

where the single-particle excitation spectrum norm is defined as (use the original form of $\hat{H} \to \hat{H} - E_0^N$ in $G^>$ resolvent):

$$\left\|\hat{H}\right\|_s \equiv \sup_{\alpha} \left\| \hat{H} \left| \psi_{\alpha}^{N+1} \right\rangle \right\| = \sup_{\alpha} \left| E_{\alpha}^{N+1} - E_0^N \right|. \tag{91}$$

Now we solve for Δ_t as follows.

$$\epsilon_d < \frac{1}{2}\Delta_t + \frac{2W}{12}\Delta_t^2 + \left\| \mathcal{O}\big(\Delta_t^4\big) \right\| = \frac{\epsilon'}{2} \tag{92}$$

$$\Longrightarrow \Delta_t + \frac{W}{3}\Delta_t^2 + \left\| \mathcal{O}\big(\Delta_t^4\big) \right\| = \epsilon'. \tag{93}$$

Let $\Delta_t = \epsilon' + a\epsilon'^2 + b\epsilon'^3 + \mathcal{O}(\epsilon'^4)$,

$$\epsilon' + a\epsilon'^2 + b\epsilon'^3 + \frac{W}{3}\epsilon'^2(1 + 2a\epsilon') + \mathcal{O}\big(\epsilon'^4\big) = \epsilon' \tag{94}$$

$$\epsilon' + (a + \frac{W}{3})\epsilon'^2 + (b + \frac{2aW}{3})\epsilon'^3 + \mathcal{O}\big(\epsilon'^4\big) = \epsilon' \tag{95}$$

$$\Longrightarrow a = -\frac{W}{3},\ b = \frac{2W^2}{9}. \tag{96}$$

$$\Delta_t = \epsilon' - \frac{W}{3}\epsilon'^2 + \frac{2W^2}{9}\epsilon'^3. \tag{97}$$

The bound on Δ_t is not useful in practice since the parameter $W \equiv \|\omega - \hat{H} + i\Gamma\|$ is not easy to compute and it depends on ω. However, since $W \leq \|H\|$, we verify that the choice $\Delta_t = \min\{\epsilon'/2, 3/\|H\|\}$ suffices to ensure $\epsilon_d < \epsilon'/2$ if $\|\mathcal{O}(\Delta_t^4)\|$ can be neglected. Note that $\Delta_t \leq \epsilon'/2$ and $\Delta_t \leq 3/\|H\|$; the latter gives $W\Delta_t \leq 3$.

$$\epsilon_d < \frac{1}{2}\Delta_t + \frac{2W}{12}\Delta_t^2 + \|\mathcal{O}\big(\Delta_t^4\big)\| \tag{98}$$

$$\approx \frac{\Delta_t}{2}\left(1 + \frac{W\Delta_t}{3}\right) \leq \frac{\epsilon'/2}{2}\left(1 + \frac{3}{3}\right) = \frac{\epsilon'}{2}. \tag{99}$$

For spectrum-normalized $\hat{H}$, $\|\hat{H}\| = \mathcal{O}(1)$ and thus $\Delta_t = \mathcal{O}(\epsilon')$.

A summary of the bounds derived above.

- $t_c = \dfrac{1}{\Gamma}\log\left(\dfrac{2}{\Gamma\epsilon'}\right)$
- $\Delta_t = \epsilon' - \dfrac{W}{3}\epsilon'^2 + \dfrac{2W^2}{9}\epsilon'^3$
- $N_c = \dfrac{t_c}{\Delta_t} \approx \dfrac{1}{\Gamma\epsilon'}\log\left(\dfrac{2}{\Gamma\epsilon'}\right)$

Now we calculate the $\|\vec{\alpha}\|_1$ in the LCU sum $h(\omega + i\Gamma, \hat{H})$.

$$h(\omega + i\Gamma, \hat{H}) = \sum_{k=0}^{N_c} \Delta_t e^{-\Gamma k \Delta_t} e^{-i[(\hat{H}-\omega)k\Delta_t + \frac{\pi}{2}]} \tag{100}$$

$$= \sum_{k=0}^{N_c} \alpha_k \hat{U}_k,$$

$$\|\vec{\alpha}\|_1 = \sum_{k=0}^{N_c} \alpha_k = \sum_{k=0}^{N_c} \Delta_t e^{-\Gamma k \Delta_t} \tag{101}$$

$$= \Delta_t \frac{1 - e^{-\Gamma(N_c+1)\Delta_t}}{1 - e^{-\Gamma \Delta_t}} \tag{102}$$

$$< \Delta_t \frac{1}{1 - e^{-\Gamma \Delta_t}} = \frac{\Gamma \Delta_t}{1 - e^{-\Gamma \Delta_t}} \frac{1}{\Gamma} \tag{103}$$

$$< \frac{\Gamma \epsilon'}{1 - e^{-\Gamma \epsilon'}} \frac{1}{\Gamma} \quad \begin{bmatrix} \frac{x}{1-e^{-x}} \\ \text{monotonically} \\ \text{increases with } x \\ \text{and} \\ x = \Gamma \Delta_t < \Gamma \epsilon' \end{bmatrix} \tag{104}$$

$$= \left[1 + \frac{\Gamma \epsilon'}{2} + \mathcal{O}\big(\Gamma^2 \epsilon'^2\big)\right] \frac{1}{\Gamma} \tag{105}$$

$$= \frac{1}{\Gamma} + \frac{\epsilon'}{2} + \mathcal{O}\big(\Gamma \epsilon'^2\big) \approx \frac{1}{\Gamma}. \tag{106}$$

$$\therefore \|\vec{\alpha}\|_1 \approx \frac{1}{\Gamma}. \tag{107}$$

Therefore, the query complexity is $\|\vec{\alpha}\|_1 t_c = \frac{1}{\Gamma^2} \log\left(\frac{2}{\Gamma \epsilon'}\right)$, which only depends on the required precision ϵ' as $\log(1/\epsilon')$ and in this aspect is similar to the cost of ground state preparation. However, the cost of numerical demonstration on classical computer is proportional to N_c that depends on the required precision ϵ' as $(1/\epsilon')\log(1/\epsilon')$. For ground state preparation, the total number of LCU terms N_z of the discretized Gaussian integration depends on the required precision ϵ' as $\log(1/\epsilon')$, so the numerical calculation of the ground state preparation is less expensive than the resolvent calculation on classical computer for the same precision.

D.5 Derivation of tightened bounds from Ge *et al.*

For parameter M in Lemma 1 from Ref. 83, we first show that the lower bound of M can be tightened from $M = \Omega\Big(\frac{1}{\Delta(\tau+\delta_E)}\log\frac{1}{\gamma\eta}\Big)$ to $M = \Omega\Big(\frac{1}{\Delta(\tau+\delta_E)+(\Delta^2/2)}\log\frac{1}{\gamma\eta}\Big)$. Then, we show that by applying the Lemma 1 with this new bound, the required precision of the ground energy in Theorem 1 from Ref. 83 can be lowered from $\mathcal{O}\Big(\Delta/\log\frac{1}{\gamma\eta}\Big)$ to $\mathcal{O}\Big(\Delta/\log^{1/2}\frac{1}{\gamma\eta}\Big)$ and the query complexity determined from the parameter m_0 can be reduced from $\mathcal{O}\Big(\frac{1}{\Delta}\log^{3/2}\Big(\frac{1}{\gamma\eta}\Big)\Big)$ to $\mathcal{O}\Big(\frac{1}{\Delta}\log\frac{1}{\gamma\eta}\Big)$.

Following the definition of Lemma 1 from Ref. 83, a new Hamiltonian H is defined from the original $\tilde{H}$ as $H = \tilde{H}-(E-\tau) = \tilde{H}-\lambda_0+(\tau+\delta_E)$, where $E \in [0,\lambda_0]$, $\delta_E = \lambda_0 - E \in [0,\lambda_0]$, and $\tau \in [0,1/2]$. Here $\{\lambda_0, |\lambda_0\rangle\}$ are the ground energy and ground state of the original $\tilde{H}$ that has a spectrum $\sigma(\tilde{H}) \in [\lambda_0, 1] \subseteq [0,1]$ with $\lambda_0 \geq 0$. We denote the first excited energy of $\tilde{H}$ as $\lambda_1 = \lambda_0 + \Delta_s \leq 1$. Here, E, τ, δ_E, λ_0 are not required to be small. Our derivation below also does not require the spectral gap Δ_s to be small.

Since $\tau + \delta_E \in [0, 3/2]$, we have $\cos^M(\tau+\delta_E) > 0$. For $l > 0$, $\lambda_l - \lambda_0 + \tau + \delta_E \geq \lambda_1 - \lambda_0 + \tau + \delta_E = \Delta_s + \tau + \delta_E > 0$ and $\lambda_l - \lambda_0 + \tau + \delta_E \leq 1 - \lambda_0 + 1/2 + \lambda_0 = 3/2$, so $0 < \cos(\lambda_l - \lambda_0 + \tau + \delta_E) \leq \cos(\Delta_s + \tau + \delta_E)$ for $l > 0$. Denote $\tau' = \tau + \delta_E$ for convenience. Note that $\Delta_s + \tau' = \Delta_s + \tau + \delta_E \leq \Delta_s + \tau + \lambda_0 = \lambda_1 + \tau \leq 1 + 1/2 = 3/2$. The new lower

bound for M is derived as follows.

$$\left\| \frac{\cos^M(H)\,|\lambda_0^\perp\rangle}{\cos^M(\tau')} \right\| = \frac{\left\| \sum_{l>0} \cos^M(\lambda_l - \lambda_0 + \tau')(c_l\,|\lambda_l\rangle) \right\|}{\cos^M(\tau')} \tag{108}$$

$$= \frac{\left(\sum_{l>0} \cos^{2M}(\lambda_l - \lambda_0 + \tau')|c_l|^2 \right)^{1/2}}{\cos^M(\tau')} \tag{109}$$

$$\leq \frac{\left(\cos^{2M}(\Delta_s + \tau') \sum_{l>0} |c_l|^2 \right)^{1/2}}{\cos^M(\tau')} \tag{110}$$

$$= \frac{\sqrt{1-\gamma^2}\cos^M(\Delta_s + \tau')}{\cos^M(\tau')} \tag{111}$$

$$< \frac{\cos^M(\Delta_s + \tau')}{\cos^M(\tau')} \tag{112}$$

$$= \left(\frac{\cos\Delta_s \cos\tau' - \sin\Delta_s \sin\tau'}{\cos\tau'} \right)^M \tag{113}$$

$$= (\cos\Delta_s)^M (1 - \tan\Delta_s \tan\tau')^M \tag{114}$$

$$< (\cos\Delta_s)^M (1 - \tau'\Delta_s)^M \tag{115}$$

$$< e^{-M(\frac{1}{2}\Delta_s^2 + \tau'\Delta_s)}. \tag{116}$$

In the second to the last step, we used $\tan x > x$ for $x \in (0, \pi/2]$ and $1 - \tan\Delta_s \tan\tau' = \cos(\Delta_s + \tau')/(\cos\Delta_s \cos\tau') > 0$. In the final step, we used $\cos x < e^{-x^2/2}$ for $x \in (0, \pi/2]$, $1 - x \leq e^{-x}$ for $x \in \mathbb{R}$, and $(1-x)^M \leq e^{-Mx}$ for $x \leq 1$ [1]. The last one has a restricted domain due to sign difference between $1 - x$ and $(1-x)^M$ for even integer M and $x > 1$. $\tau'\Delta_s < 1$ follows directly from $\tau'\Delta_s < \tan\Delta_s \tan\tau' < 1$. To make

$$\left\| \frac{\cos^M(H)\,|\lambda_0^\perp\rangle}{\cos^M(\tau')} \right\| < \gamma\eta, \tag{117}$$

[1]Both $\tan x > x$ for $x \in (0, \pi/2]$ and $e^{-x} \geq 1 - x$ for $x \in \mathbb{R}$ are easy to verify by noticing that the functions $\tan x$ and e^{-x} are concave upward in the respective domains, and x and $1 - x$ are the tangent lines for the respective functions in their domains. $\cos x < e^{-x^2/2}$ for $x \in (0, \pi/2]$ can be shown as follows. Integrating both sides of $\tan x > x$ in a domain $[0, \theta]$, where $\theta \in (0, \pi/2)$, we find $-\log\cos\theta > \theta^2/2$. This gives $1/\cos\theta > e^{\theta^2/2}$ and thus $\cos\theta < e^{-\theta^2/2}$ for $\theta \in (0, \pi/2)$. Last, for $\theta = \pi/2$, the inequality can be directly verified.

it is sufficient to set $e^{-M(\frac{1}{2}\Delta_s^2+\tau'\Delta_s)} \leq e^{-M(\frac{1}{2}\Delta^2+\tau'\Delta)} < \gamma\eta$, and then we find the lower bound for M is

$$M = \Omega\left(\frac{1}{\tau'\Delta + (\Delta^2/2)} \log \frac{1}{\gamma\eta}\right). \tag{118}$$

In proving their Theorem 1 (in which Δ_s and τ' are now assumed to be small and $\log \frac{1}{\gamma\eta}$ large), to ensure $\left\|\cos^M(H)\,|\psi_0\rangle\right\| = \Omega(\gamma)$, Ge *et al.* [83] found the following condition must be satisfied: $\tau'^2 M/2 = \mathcal{O}(1)$. For our bound of M, this can be achieved by choosing $\tau' = \mathcal{O}\left(\Delta/\log^{1/2}\frac{1}{\gamma\eta}\right)$ and $M = \mathcal{O}\left(\frac{2}{\Delta^2}\log\frac{1}{\gamma\eta}\right)$. Since $\tau' = \tau + \delta_E$ and δ_E represents the precision of the ground energy, the required precision of the ground energy is also $\mathcal{O}\left(\Delta/\log^{1/2}\frac{1}{\gamma\eta}\right)$. The parameter m_0 related to the number of LCU terms and the query complexity can be found by setting the truncation error (by the bound to lower and upper tails of the binomial distribution) $2e^{-m_0^2/m} = 2e^{-2m_0^2/M} = \gamma\eta$, which leads to $m_0 = \mathcal{O}\left(\sqrt{(M/2)\log\frac{2}{\gamma\eta}}\right) = \mathcal{O}\left(\frac{1}{\Delta}\log\frac{\sqrt{2}}{\gamma\eta}\right)$. The constant factor $\sqrt{2}$ is kept in the formula in order to more accurately compare with our algorithm in the numerical demonstration [2].

[2]The constant factor $\sqrt{2}$ is derived as follows. $(\log\frac{1}{\gamma\eta}\log\frac{2}{\gamma\eta})^{1/2} = [\log\frac{1}{\gamma\eta}(\log\frac{1}{\gamma\eta}+\log 2)]^{1/2} = \log\frac{1}{\gamma\eta}[1+(\log 2)\log^{-1}\frac{1}{\gamma\eta}]^{1/2} \approx \log\frac{1}{\gamma\eta}[1+(\frac{1}{2}\log 2)\log^{-1}\frac{1}{\gamma\eta}] = \log\frac{1}{\gamma\eta} + \log\sqrt{2} = \log\frac{\sqrt{2}}{\gamma\eta}$

Vita

Trevor Keen graduated from South Central High School in Farina, Illinois before attending Southern Illinois University, Carbondale in Carbondale, Illinois. He graduated in May 2017 with a Bachelor of Science in Computational Physics as well as a Bachelor of Science in Mathematics, cum laude. He then chose to pursue doctoral studies at the University of Tennessee, Knoxville in the department of Physics and Astronomy through research conducted at Oak Ridge National Laboratory and coursework at the University of Tennessee.